Dissertation

Lipid Hydrolysis in Liver Disease

submitted by

BSc. MSc.

Maximilian SCHINAGL

for the Academic Degree of

Philosophy (PhD)

at the

Medical University of Graz

Diagnostic and Research Institute of Pathology

Medical University of Graz

Stiftingtalstraße 24/1

8010 Graz, Austria

under the Supervision of

Univ. Prof. Dipl.-Ing. Dr. techn. **Ruth Birner-Grünberger**

2023

Page intentionally left blank

Statutory Declaration

I hereby declare that this thesis is my own original work and that I have fully acknowledged by name all of those individuals and organisations that have contributed to the research for this thesis. Due acknowledgement has been made in the text to all other material used. Throughout this thesis and in all related publications I followed the “Guidelines of the Medical University of Graz on Good Scientific Practice.”

Date: Tuesday, 18 July 2023

_____

Maximilian Schinagl

Disclosures

This thesis opens with a general introduction into the topic of human liver disease and first highlights our findings regarding lipid metabolism in liver cells (hepatocytes) in chapter one. Subsequently, chapter two presents our scientific discoveries in liver fibrosis and hepatic stellate cells. Some of the results of chapter two have been published in the International Journal of Molecular Sciences (IJMS, Multidisciplinary Digital Publishing Institute MDPI) doi:10.3390/ijms222312782 by Maximilian Schinagl, Tamara Tomin, Juergen Gindlhuber, Sophie Honeder, Raphael Pfleger, Matthias Schittmayer, Michael Trauner and Ruth Birner-Gruenberger under the title “Proteomic Changes of Activated Hepatic Stellate Cells” (1).

Additionally, my contribution to several publications can be viewed in the following co-authorships: (2–4)

All co-authors were contacted and granted the use of their data in this thesis.

All figures adapted from other publications are licenced under creative common licence CC BY 4.0, allowing for the use of the material for any purpose in accordance with the publisher. Respective figures are indicated by a statement at the end of the figure legend showing adequate attribution.

Funding

This research was funded by Austrian Science Fund FWF, grant numbers F73 (SFB “Lipid hydrolysis”) and W1226 (Doctoral School “DK-Metabolic and Cardiovascular Disease”).

Acknowledgements

Despite conducting the majority of this thesis amidst the challenges posed by the first global pandemic, I can assert with confidence that the experience surpassed my expectations and brought me an immense amount of joy. The impact of being a scientist on my life has been unparalleled, surpassing any other influence.

Above all, I am immensely grateful for our dear captain Ruth. She consistently remained accessible, even while juggling more tasks than any of us could handle individually, all the while making it appear effortless. Transferring an entire laboratory from Graz to Vienna and effectively managing both facilities is an accomplishment only she could achieve. Despite her overwhelming workload, she led us with the wisdom of a seasoned captain. Although I may not have followed every piece of advice she offered, she consistently proved to be correct in the end.

I would also like to extend my gratitude to Richard Lehner, whose invaluable assistance has helped me gain a fresh perspective in my research, and to the entire team at the University of Alberta for graciously hosting me. Special thanks are due to Russell Watts, who proved to be an exceptional lab manager and friend, going above and beyond expectations. Randal Nelson, a true embodiment of a living scientific encyclopaedia, deserves recognition for his vast knowledge and expertise. Jihong Lian, a remarkable individual who encompasses the skills and qualities of an entire team. And last but certainly not least, I express my appreciation to Chinmayee Das, the heart and soul of the lab and an esteemed microscopy expert. Although our time together may have been limited, I consider each of you as dear friends.

Furthermore, I express my gratitude to my comrades in piracy, as none of this would have been feasible without you. Thank you, Jürgen, for introducing my to the group and teaching me the in-and outs of microscopy. Laura and Babsi, you form the very foundation of our lab, and without your presence, none of my endeavours would have been imaginable. Tam, you are an unparalleled source of guidance, both in scientific and non-scientific matters within our lab. You are the cohesive force that binds this crew together, selflessly aiding students in countless ways, perhaps even unbeknownst to yourself. I wish to extend my thanks to Matthias for ensuring the seamless operation of all our procedures, to the extent that an analysis

can be initiated with little more than the press of a button. Sophie, I am grateful for your role as my peer, friend, teacher and at times, my second brain when navigating bureaucratic tasks. Raphael, you are an exceptional student and undoubtedly the life of every party. Thank you for all your help. Isa, you are the one person who always makes me laugh when life isn't fun. Thank you for that. Dominik, thank you for being an excellent fitness instructor, perpetually overflowing with enthusiasm and knowledge. Vici, your leadership in managing the laboratory and your guidance through the jungle of TU Wien deserve my sincere appreciation. Additionally, I extend my thanks to those with whom I had the pleasure of spending a brief period: Julia, Petra, Terka, and Jonas.

I am grateful for my thesis committee consisting of Prof. Hämmerle and Prof. Trauner for guiding me through my thesis. Furthermore, I want to express my deepest gratitude for Karin, our beloved manager for the doctoral studies program.

Lastly, I would like to express my heartfelt appreciation to my family and friends for the unwavering support they have provided me over the past years. Mum, Dad, Walter and Anneliese, Sebastian and all my other brothers and sister, my grandparents, Simon, Lorenz, Oliver, Hansi, Roman and other cherished friends and family: your consistent encouragement has made it feasible for me to traverse this path. I am sincerely grateful for all that you have done.

Table of Contents

Chapter Two: The role of lipid metabolism in hepatic stellate cell induced liver fibrosis

Abbreviations and Definitions

Cell lines

HepG2.....hepatocellular carcinoma cell line
Hep3B .....hepatocellular carcinoma cell line
HSC .....hepatic stellate cell
LX-2 ... Lieming Xu 2 hepatic stellate cell line

Proteins

ABHD5 ..A/B hydrolase containing protein 5
ATGL.....adipocyte triglyceride lipase
CGI-58 .. comparative gene identification-58
COL1A1 ..... collagen type 1 α 1
PNPLA3 ..... patatin-like p.-lipase c. protein 3
α-SMA.....α-smooth muscle actin

Medical terminology

AFL..... alcoholic fatty liver
ALD ..... alcoholic fatty liver disease
HCC .....hepatocellular carcinoma
NAFL .....non-alcoholic fatty liver
NAFLD ..... non-alcoholic fatty liver disease
NASH..... non-alcoholic steatohepatitis

Molecular biology terminology

DG..... diglyceride
ECM .....extracellular matrix
FA..... fatty acid
FFA .....free fatty acid
KD .....knock-down
KO ..... knock-out
LD .....lipid droplet
OE .....over-expression
TG ..... triglyceride

Others

RT..... room temperature

Zusammenfassung

Leberkrebs ist eine der wenigen Krebsarten mit steigender Inzidenz. Dies kann teilweise auf eine erhöhte Fettleibigkeit der Bevölkerung und der daraus resultierenden Zunahme von nicht-alkoholischer Fettlebererkrankung, die die Entwicklung von Leberfibrose und Krebs fördert, zurückgeführt werden. In dieser Arbeit untersuchen wir veränderten Fett-(Lipid)-stoffwechsel in Leberzellen und seine Auswirkungen auf Zellproliferation, Glukosestoffwechsel und fibrotisches Potential von speziellen Leberzellen (hepatische Sternzellen). Dazu betrachten wir drei wichtige Proteine im Lipidstoffwechsel der Leber genauer und untersuchen deren Auswirkungen in Leberzellen Mithilfe von Phänotyp- und Proteomanalysen.

Erstens zeigen wir, dass eine (enzymatische) Abnahme des wichtigsten Triglycerid-Katabolismus-Proteins Adipose Triglyceride Lipase (ATGL) nur das Lipidtropfenvolumen der Leberzellen erhöht, jedoch das Zellwachstum nicht beeinflusst, obwohl ATGL in Leberkrebszellen, im Vergleich zu gesundem Gewebe, eine verminderte Genexpression aufweist. Das übergeordnete Regulations-Protein von ATGL, CGI-58 (ABHD5), zeigte eine ähnlich niedrige Genexpression in Leberkrebsgewebe, im Vergleich zum gesunden Gewebe. Eine verminderte Expression von CGI-58 erhöhte ebenfalls das Lipidtropfenvolumen in Leberzellen, wirkte sich jedoch auch positiv das Zellwachstum in Hepatozyten aus. Die Proteom- und Phänotyp-Analyse von Hepatozyten mit verminderter CGI-58 Expression zeigte eine Verschiebung des Stoffwechsels auf einen Glucose-zentrierten Metabolismus mit erhöhter Glykolyse, was auf eine Änderung hin zu einem krebsartigeren Phänotyp in diesen Zellen hinweist. Interessanterweise verursachte eine erhöhte Expression von CGI-58 keine der oben genannten Veränderungen im Hepatozyten-Phänotyp. Als nächstes wurde PNPLA3 untersucht, ein Enzym, das mit einer Zunahme von Lebererkrankungen in seiner mutierten Form assoziiert ist und analoge Auswirkungen auf den Lipid- und Glukosestoffwechsel, ähnlich einer verminderten Expression von CGI-58, zeigte.

Zweitens untersuchten wir das Proteom und den Phänotyp von spezialisierten Leberzellen, den sogenannten "hepatischen Sternzellen". Diese Zellen sind dafür verantwortlich, Fibrose in der geschädigten Leber auszulösen, und durchlaufen massive Veränderungen während ihrer Transformation von einem ruhenden Zustand in einen "aktiven" fibrotischen

Zustand. Wir berichten, dass diese Aktivierung mit einer Zunahme der zellulären Migration, einer erhöhten Proliferation, dem Verlust von Lipidtropfen-Volumen, einer Erhöhung der Proteinsynthese und einer Umstellung auf einen Glucose-zentrierten Stoffwechsel verbunden ist. Eine erhöhte Expression des I148M mutierten PNPLA3-Gens (eine im Menschen weitverbreitete Mutation) in diesen Zellen resultierte in einer vermehrten Expression von Proteinen, die die Aggressivität von Krebszellen fördern.

Zusammenfassend zeigen wir die Bedeutung des gesunden Lipidstoffwechsels in Leberzellen auf und demonstrieren, wie der Lipidstoffwechsel mit anderen Stoffwechselwegen der zellulären Energiegewinnung verbunden ist.

Abstract

Liver cancer is one of the few types of cancer with rising levels of occurrence. This is mostly due to growing levels of obesity and the subsequent increase in non-alcoholic fatty liver disease initiating development of liver fibrosis and cancer. In this thesis we explore abnormal lipid metabolism in liver cells and its consequences on cell proliferation, glucose metabolism, and fibrotic potential of specialized liver cells (hepatic stellate cells). For this, we take a closer look at three important proteins in liver lipid metabolism using phenotypic and proteomic analyses.

First, we show that a decrease of the major triglyceride catabolizing protein activity Adipose-triglyceride-lipase (ATGL) merely increases cytosolic lipid droplet volume, but does not influence cell growth, despite ATGL showing decreased expression in liver cancer cells, compared to healthy tissue. The upstream regulator of ATGL, CGI-58 (ABHD5), displays similar downregulation in liver cancer tissue as ATGL, compared to healthy tissue. CGI-58 silencing likewise increased cytosolic lipid droplet volume, but also positively affected cell growth in hepatocytes. Proteomic and phenotype analysis of CGI-58 depleted hepatocytes indicated a switch to increased glycolysis, resembling a shift towards a more cancerous phenotype in these cells. Interestingly, an overabundance of CGI-58 did not cause any of the above-mentioned metabolic changes in the hepatocyte phenotype. Next, we found that PNPLA3, an enzyme associated with an increase in liver disease in its mutated form, showed similar effects to CGI-58 downregulation on alterations of lipid and glucose metabolism.

Second, we investigated the proteome and phenotype of specialized liver cells, so called hepatic stellate cells (HSC). These cells are responsible for initiating fibrosis in the injured liver and undergo massive changes during their transformation from a resting “quiescent” state, into an “active” fibrotic state. We demonstrate that this activation is associated with an increase in migratory behaviour, increased proliferation, lipid droplet volume loss, an increase in protein production, and a switch towards a glucose-focused metabolism. Moreover, increased I148M PNPLA3 mutant expression (a common mutation in humans) in these cells was accompanied by an upregulation of proteins strongly associated with cancer aggressiveness.

Collectively, we demonstrate the importance of functional lipid metabolism in liver cells and show how lipid metabolism is connected to other energy metabolism pathways.

1 General introduction

Cancer rates worldwide are increasing, especially in countries with long life expectancy. There were approximately 19.3 $*10^6$ new cancer cases in 2020 and $10.0*10^6$ people died from cancer in 2020 (5). Due to an increasingly older population, cancer rates are predicted to rise to 29.5 $* 10^6$ cases per year[1] by the year 2040, with a projected overall mortality of ~ 55 %[2], according to the International Agency for Research on Cancer at the World Health Organisation (6). Although the general public perceives cancer as a single disease, different types of cancer and underlying causes for cancer are varying wildly. It is therefore crucial to obtain a better understanding of the biochemical processes leading to cancer in order to develop effective prevention measures and treatments.

Liver cancer is one of the few cancer types steadily increasing in occurrence[3] (Figure 1 A) while having a strikingly low 5-year survival rate of 20 % (Data for United States only) (7). The causes for liver cancer range from alcohol consumption to toxin ingestion (aflatoxin b[4]) and fatty liver disease. Especially fatty liver disease or the umbrella term "non-alcoholic fatty liver disease" (NAFLD), excluding alcohol abuse, is a serious concern especially due to globally rising obesity rates. The world population showed overweight in 28.8 % of people and obesity rates of 19.8 % in 2016 (Figure 1 B) with steadily increasing rates of both overweight and obesity (10). NAFLD is therefore becoming an increasingly serious public health concern.

[1] https://gco.iarc.fr/tomorrow/en/dataviz/bubbles?sexes=0&mode=population (accessed on 04.01.2023)
[2] https://gco.iarc.fr/tomorrow/en/dataviz/trends?sexes=1_2&mode=population&types=1 (accessed on 04.01.2023)
[3] Primary liver cancer cases have increased by ~ 328 % in the last 40 years (data averaged from 1975-1979 vs. 2015-2019) while stabilizing slowly since 2010 (7), see also Figure 1. (Data for United States only).
[4] Aflatoxin B1 is a common food contaminant produced by the fungus *Aspergillus flavus* and has been affecting grain storage mainly in Asia until the 1990s, leading to rising cases of liver disease which have been falling recently (8). Data for liver cancer occurrence and mortality in this thesis is therefore sourced primarily from the United States.

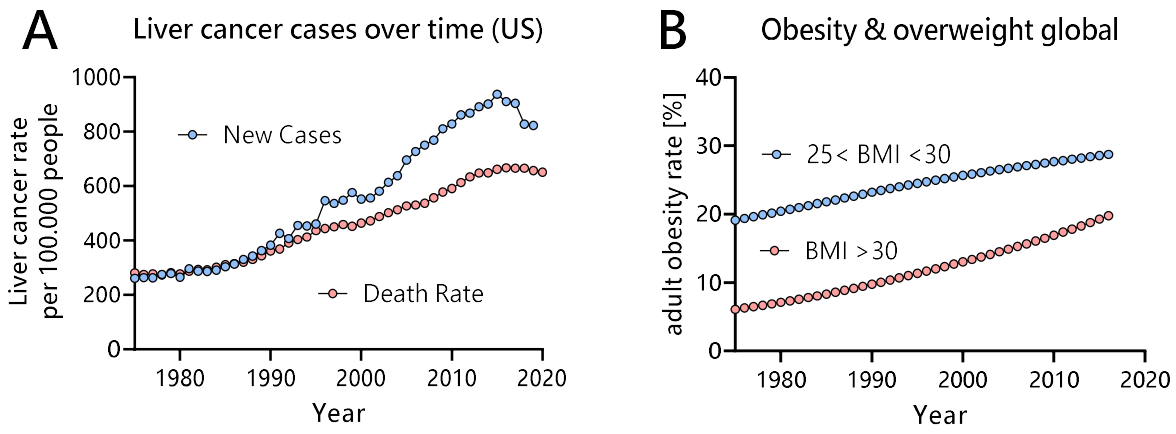

Figure 1: Liver cancer cases in the US and global obesity and overweight rates over time. (A) Liver cancer cases in the United States over time. Data from National Cancer Institute (National Institute of Health NIH) available at https://seer.cancer.gov/statfacts/html/livibd.html (accessed 04.01.2023). Cases include liver and intrahepatic bile duct cancer. **(B)** Global obesity and overweight rate for people with a body mass index (BMI) > 25 while <30 (overweight) or obese BMI > 30. Data from World Health Organization WHO https://www.who.int/data/gho/data/indicators/indicator-details/GHO/prevalence-of-obesity-among-adults-bmi-=-30-(crude-estimate)-(-) (accessed 04.01.2023).

1.1 Liver disease

The human liver is the only organ[5] in the human body which is capable of regenerating large amounts of lost or damaged tissue (11). This ability is reliant on a complex synergistic network of cells, which first leads to the isolation of the damaged sections of the liver and then re-structuring of the environment for new liver cells to populate the area (12,13). Although this process is useful to withstand a plethora of injuries, the liver is susceptible to long-term inflammation and damage. This is apparent from the pathophysiology of both alcoholic liver disease (ALD) and NAFLD. Both of these liver diseases feature similar modes of slow

[5] Excluding bone marrow and skin.

progression and show underlying disease mechanisms (14). While ALD is caused by long term consumption of ethanol (15), NAFLD is progressing due to excessive storage of liver fat (16). Both ALD- and NAFLD related mortality have been on the rise in recent years (17,18). Both ALD and NAFLD contribute to an increased risk of hepatocellular carcinoma (HCC) (19,20). The increase in HCC cases correlates with the global obesity epidemic (21,22) (Figure 1 A, B). Although ALD and NAFLD are an enormous burden on public health (23), no effective treatment, other than decreased alcohol consumption (ALD) and weight loss (NAFLD) is currently available (24).

1.1.1 Alcoholic fatty liver disease (ALD)

Although this dissertation is focused on the role of lipids in liver diseases, a short introduction is given for ALD, as this disease shares wide public recognition and features a disease progression similar to NAFLD. ALD is caused by the consumption of alcohol over a long period of time in which high risk individuals (heavy drinkers) are classified by drinking over 40 g of ethanol per day over many years (25). Heavy drinkers accumulate fat in hepatocytes, often leading to an alcoholic fatty liver (AFL), also known as alcoholic steatosis (15). The reasons for AFL development are multifactorial, including increased acetyl-CoA[6] production from ethanol via acetaldehyde and acetic acid (26), decreased mitochondrial β-oxidation via deregulated NADH/NAD^+ ratios (27–29) and peroxisome proliferator-activated receptor α (PPARα) inactivation (30), as well as upregulated lipogenesis via SREBP1c (31). AFL is a strong risk factor for the development of liver inflammation (steatohepatitis) (32). AFL featuring steatohepatitis can progress further to liver fibrosis and cirrhosis (32), which in turn increases the risk for the development of liver cancer dramatically (33).

1.1.2 Non-alcoholic fatty liver disease (NAFLD)

Since 1975 obesity rates among adults in the United States have increased from 6.1 % to 19.8 % in 2016 (Figure 1 B) (10). This societal change has come with a plethora of negative

[6] Precursor for fatty acid (FA) synthesis via acetyl-CoA carboxylase (ACC) to malonyl-CoA.

health effects, among which NALFD has been one of the worst contenders, together with heart disease (34). NAFLD is used as an umbrella term, encompassing many different aspects of a progressive liver disease such as non-alcoholic steatosis, liver fibrosis, and cirrhosis (35) (Figure 2).

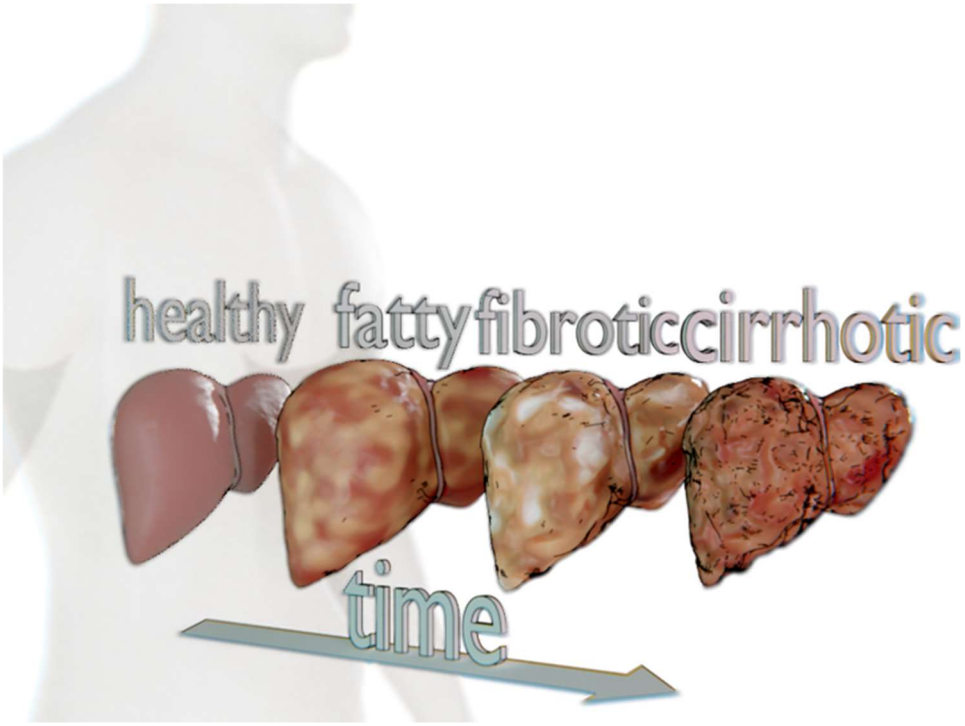

Figure 2: Potential progression of non-alcoholic fatty liver disease (NAFLD) in humans over time. Increased levels of hepatic fat accumulation can lead to a progression of liver disease from a fatty liver to a fibrotic and later cirrhotic liver.

Steatosis is defined as > 5 % of hepatocytes displaying lipid droplet[7] (LD) deposition (Figure 3) in the absence of alcohol consumption (36) and is often followed by liver inflammation, also called non-alcoholic steatohepatitis (NASH). This progression can be attributed to

[7] Lipid droplets (LD) are intracellular organelles responsible for lipid storage. They typically range from 20 nm to 100 nm in size in hepatocytes. LD are made up of triglycerides (TG), cholesterol esters and other less common lipid species surrounded by a phospholipid monolayer membrane (Figure 3).

lipotoxicity[8] and subsequent inflammation of the liver (38). Recruitment of immune cells due to inflammation is often followed by the activation of neighbouring hepatic stellate cells (HSC) (38) which create a fibrotic (scar-tissue like) environment (see chapter 1.1.3). If inflammation persists for a long-time, accumulation of fibrotic proteins in larger sections of the liver restrict liver function (39). This stage is termed cirrhosis and generally deemed irreversible[9] (42). The only viable option to improve liver function at this stage is liver transplantation (42). Even though the cause for hepatocellular carcinoma (HCC, see chapter 1.1.4 below) is not always clear, 80 – 90 % of HCC cases feature cirrhosis (43), suggesting a strong correlation between these diseases.

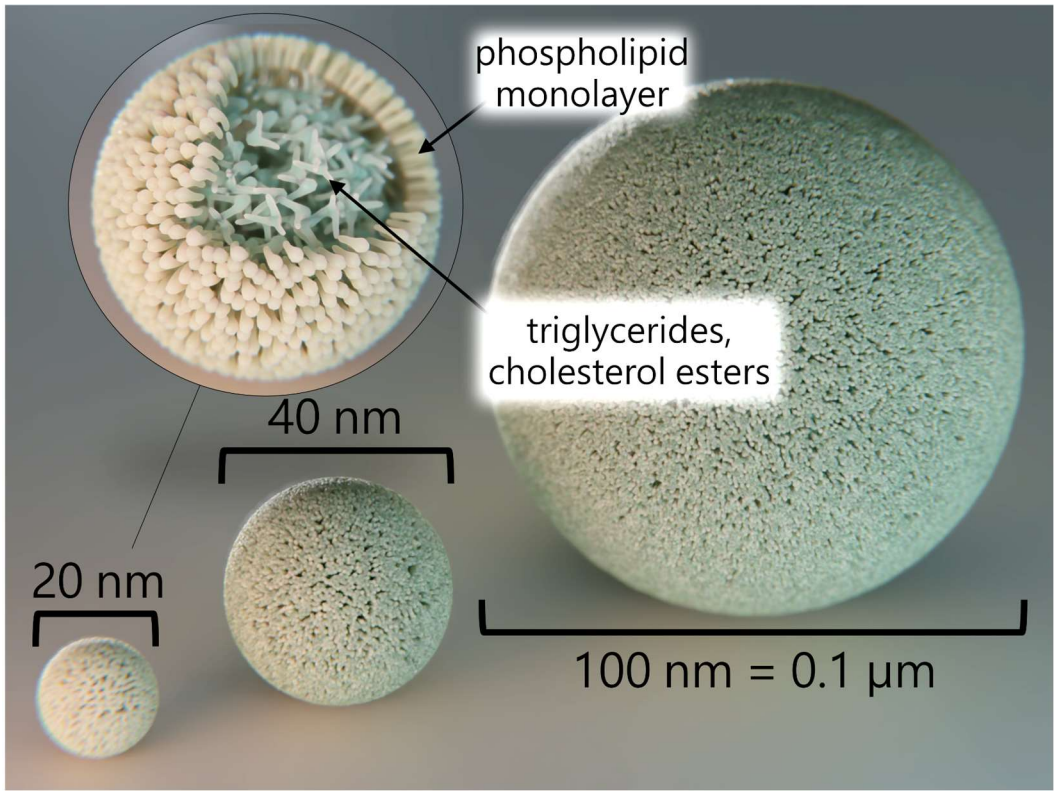

[8] Lipotoxicity is defined as a broad category of cellular damages caused by various lipid species. An overabundance or insufficient clearance of free fatty acids (FFA) can cause lipotoxicity in the liver (37).
[9] New findings suggest cirrhosis might be at least partially reversible if treated early on (40,41).

Figure 3: Lipid droplet (LD) sizes in healthy hepatocytes. Comparison of common LD sizes and composition in healthy hepatocytes. nm = nanometre, µm = micrometre.

1.1.3 Liver fibrosis

Liver fibrosis is characterized by the accumulation of fibrotic extracellular matrix (ECM) proteins usually as a consequence of chronic liver disease or liver damage. ECM production is unambiguously linked to activated (fibrotic) hepatic stellate cells (HSC) (44,45). Fibrotic tissue severely restricts liver function and blood flow to the liver (portal hypertension) (46), leading to liver enlargement and then shrinkage (in the early and late stages of the disease, respectively) and severe weight loss reaching the point of cachexia[10] in some cirrhosis cases (47). To date, there is no available medically approved treatment for liver fibrosis.

1.1.4 Hepatocellular carcinoma (HCC)

Among liver cancer cases, primary HCC (emerging in hepatocytes) is the most common type of cancer, accounting for ~ 90 % of cases (48), followed by bile duct cancer. The 5-year survival rate for HCC is as low as ~ 20 % (7), being the third deadliest cancer type globally. HCC is strongly associated with cirrhosis and liver fibrosis. Hepatitis B (48) and C (49) are strong factors implicated in HCC development, together with aflatoxin B_1 (8). Common causes for HCC are slowly developing liver diseases triggered by alcohol (ALD) and obesity (NAFLD), as these can end up contributing significantly to the risk of developing cirrhosis and subsequently HCC (19).

1.2 Liver cells

The human liver features multiple cell types, whereas the only parenchymal[11] cell type in the liver are hepatocytes. These cells are responsible for a myriad of tasks, ranging from modification and detoxification of substances in the bloodstream to the synthesis and

[10] Disease instigated muscle and weight loss with increased mortality. Not treatable by nutritional supplementation.

[11] Non-structural or functional parts of an organ in contrast to stromal, or supportive tissue.

distribution of lipids including cholesterol. Non-parenchymal cells include HSC, endothelial liver sinusoidal cells (Figure 4) and liver macrophages (Kupffer cells).

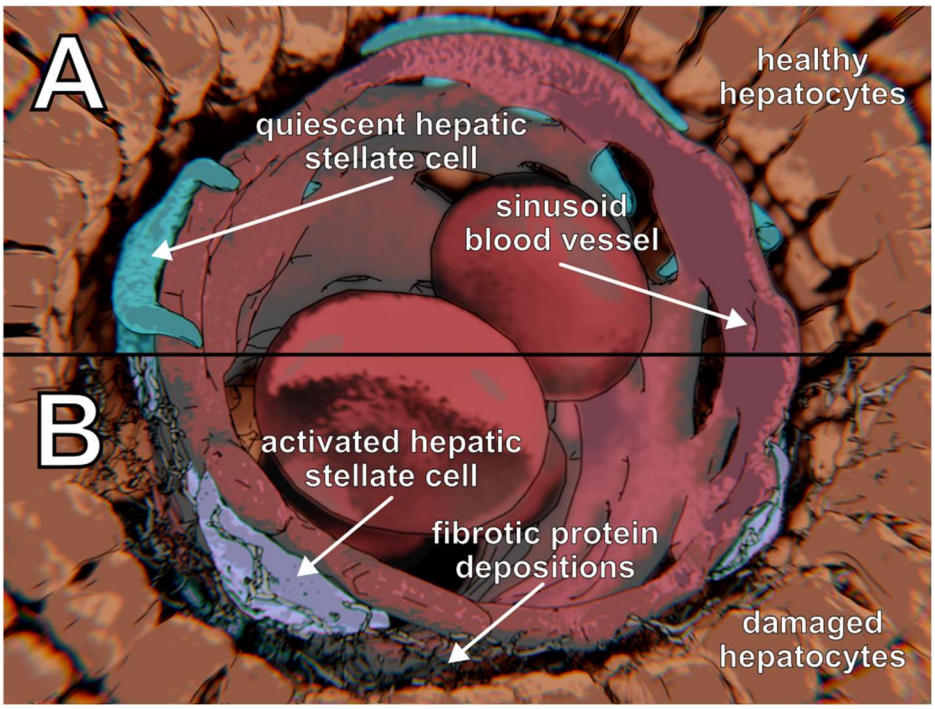

Figure 4: Graphical representation of a liver sinusoid (blood vessel) close-up. (A) Representation of a healthy liver featuring hepatocytes and quiescent hepatic stellate cells (HSC) in the Space of Dissee (perisinusoidal space) between hepatocytes and a blood capillary. **(B)** Graphical demonstration of an injured liver highlighting damaged hepatocytes and fibrotic protein deposition by activated HSC.

1.2.1 Hepatocytes

Hepatocytes make up 80 – 90 % of all liver cells by weight and cell number. They measure ~20 – 30 µm in diameter, making them one of the larger cells in the human body. Hepatocytes feature a large smooth endoplasmic reticulum, necessary for the synthesis and excretion of lipids and detoxification of both endogenous and exogenous substances (50). Hepatocytes also produce bile acid for lipid absorption in the intestine and excrete lipids via lipoproteins to be distributed via the blood stream. Their ability to produce lipids via *de novo* lipogenesis in large quantities makes them unique in the human body. Hepatocytes aim to balance lipid

levels in the blood by absorbing excess lipids or by increasing lipid production and export (51). Elevated blood lipid levels can arise from increased mobilization of FA from adipose tissue due to obesity and diabetes or increased intestinal absorption of dietary FA. Overwhelming blood lipid levels can therefore increase hepatic lipid content and lead to NAFLD in the long term.

1.2.2 Hepatic stellate cells (HSC)

Being the main driver of liver fibrosis in humans, HSC have gained increased interest in the last decades. Also known as lipocytes or Ito-cells[12], HSC in their quiescent (resting) state are mainly involved in vitamin A (retinol) storage being located in the area between liver sinusoidal cells and hepatocytes, better known as "Space of Disse" (Figure 4). These cells release vitamin A during times of vitamin A shortage in the body. Apart from vitamin A (retinol) (40 %), HSC also store TG and cholesterol esters at 32 % and 15 % of their total LD composition, respectively (52).

When HSC transform into their activated state during liver damage, they resemble fibrotic myofibroblast cells (53). This transformation marks a major shift in protein expression, lipid metabolism and overall phenotype, including increased proliferation and migration (53). Activated HSC deposit large amounts of fibrotic proteins[13] (Figure 4 B) and attract immune cells, which in turn influence HSC activation (54). Inflammatory environments perpetuate HSC activation, leading to large scale fibrosis of the liver over a long period of time if the source of inflammation remains unresolved.

Activated HSC were believed to undergo apoptosis after the source of liver damage or inflammation has been removed. Recent studies however indicate that HSC can undergo reversal of their activated state, which might aid re-structuring damaged parts of the liver after injury (55). Reversed HSC (rHSC) provide an important therapeutic potential, as they might halt, or even reverse advanced fibrosis.

[12] Named after their discoverer Toshio Ito in 1951.

[13] Mostly collagen and fibronectin.

1.3 Lipid metabolism in the liver

Liver cells are responsible for lipid homeostasis in the human body by clearing excess lipids from the bloodstream and distributing lipids via excretion of lipoproteins. Due to their dual role in systemic lipid metabolism, liver cells are disproportionally affected by lipid overload. Several aspects of lipid uptake, clearance, and distribution in the liver can be negatively affected leading to liver damage, cell death and inflammation.

1.3.1 Role of the liver in systemic lipid supply

Lipid uptake in the human body is occurring through intestinal lipid absorption. Pancreatic lipases hydrolizes TG[14] in the intestine, aided by bile produced and excreted from the liver. Due to the hydrophobic character of most lipids, bile helps emulsifying lipids aiding uptake in micelles after being broken down into FA, monoacylglycerol and glycerol. Lipids are taken up by enterocytes via cluster of differentiation 36 (CD36 or fatty acid translocase) lipid transport proteins or passive diffusion, are re-esterified to TG and distributed into the bloodstream as lipoproteins, allowing transport of TG and cholesterol in polar environments. Lipoproteins are taken up and hydrolized by lipoprotein lipase (LPL) into FA and monoacylglycerol by hepatocytes, skeletal muscle, and adipocytes, where they are subsequently either stored as re-esterified TG or used in β-oxidation. FA originating from peripheral adipose tissue can be taken up by hepatocytes and subsequently stored in cytosolic LD. Similar to enterocytes, hepatocytes are able to re-distribute lipids into the bloodstream via lipoproteins.

1.3.2 Cellular lipid metabolism in the liver

The liver is the only major source of newly synthesised lipids in the human body and able to redistribute them via lipoproteins secreted into the bloodstream. Various proteins are involved in the synthesis and breakdown of lipids in the liver, which are discussed in the next section. Cytosolic LD TG hydrolysis takes place in a process called “neutral lipolysis”, which refers to the fact that the breakdown of TG happens in a non-acid environment, in contrast to

[14] Nutritional lipid composition is mainly consisting of TG (~95 %) in addition to sterols, phospholipids and fat-soluble vitamins (56).

the acidic environment in the lysosome where TG is hydrolized by lysosomal acid lipase (LAL) (Figure 5). The lipolytic cascade, breakdown of TG by removing FA from the glycerol backbone, starts with adipose triglyceride lipase (ATGL) (57) on cytosolic LDs, continues with hormone-sensitive lipase[15] (HSL) (59) and MGL removing the second and last FA from diacyl- and monoacylglycerol (60). HSL can additionally hydrolyse TG, although to a lower extent compared to ATGL (59).

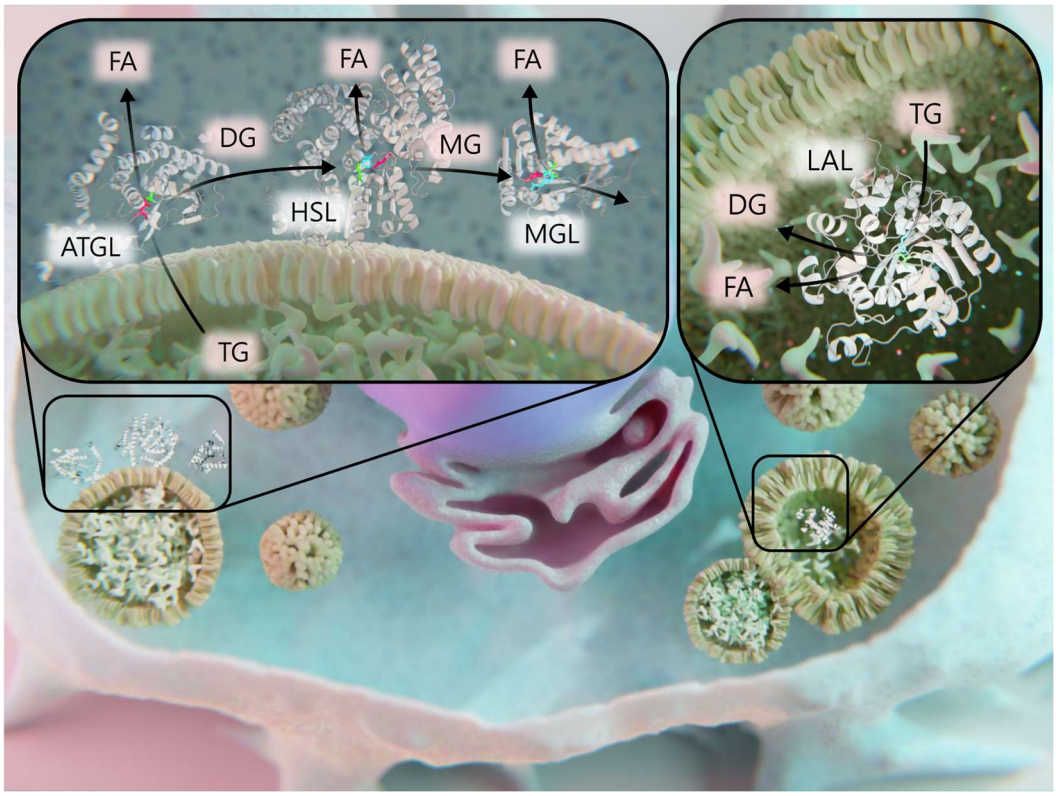

Figure 5: Graphical representation of central intracellular lipases. ATGL, HSL and MGL carrying out neutral lipolysis on and in close proximity to an intracellular LD by hydrolysing TG, DG, and MG (left). LAL performing acidic lipolysis in a lysosome via hydrolysis of TG to DG

[15] In the human liver (especially in hepatocytes), HSL expression levels are low, compared to other tissues (58). Data from human protein atlas: https://www.proteinatlas.org/ENSG00000079435-LIPE/tissue/Liver#rnaseq (accessed 05.01.2023)

and FA (right). Adapted from Honeder *et al* 2023 (61) with approval from the publisher under CC BY 4.0 license.

Adipose triglyceride lipase (ATGL)

ATGL or patatin-like phospholipase domain-containing protein 2 (*PNPLA2*) is the first and rate-limiting enzyme in the lipolytic cascade (57). The main substrate for ATGL are TG in LD. ATGL achieves its maximum efficiency when co-activated by alpha/beta hydrolase domain containing protein 5 (*ABHD5*, comparative gene identification 58 "CGI-58") (62). The release of fatty acids by ATGL from TG by co-activation of CGI-58 is crucial to protect the liver from an overabundance of lipids. Even though lipids stored as neutral TG are not lipotoxic, unmediated accumulation of large and numerous LD can lead to lipotoxicity and subsequently apoptosis of hepatocytes through ballooning[16] and successive inflammation (63). Insufficient re-esterification of FA from extracellular sources, increased *de novo* lipogenesis and decreased export of FA can further increase the risk for hepatocyte apoptosis and subsequent immune responses.

ATGL deletion or mutations in mice can cause steatosis which are specific for loss of CGI-58 accumulation of fat in various tissues, as well as obesity (64), but no skin barrier defects[17] (66). Paradoxically, neither systemic loss (67) nor specific loss of ATGL in hepatocytes (68) leads to impaired liver function, although in both cases increased TG levels are found in the liver. Interestingly, systemic pharmacologic ATGL inhibition leads to improvements in liver health (69). Briefly, decreased systemic ATGL expression lowers FA mobilized from adipose tissue, followed by decreased liver FA uptake, while reducing *de novo* lipogenesis (70).

Although there are no known cases of genetic loss of ATGL in humans, rare frame-shift mutations in the PNPLA2 gene can lead to a premature stop codon (71). ATGL mutations in

[16] Ballooning describes a degenerative form of apoptosis in hepatocytes which is characterized by swelling of the cell body.
[17] Mice with CGI-58 loss die perinatally and have severe skin barrier defects due to the loss of certain long-chain fatty acids making up that skin barrier (65).

humans lead to cardiac and skeletal myopathy, but surprisingly neither steatosis nor obesity (72). Hepatomegaly has, however, been reported in some cases (71).

The involvement of ATGL in cancer is not yet clear and might be highly dependent on the tissue of the primary tumor. In lung and colorectal cancer increased ATGL expression shows pro-neoplastic features (73,74), although recent data in our group hints at a more aggressive phenotype of human lung cancer cell lines with ATGL loss (3,75). Liver cancer occurrence and aggressiveness might be attenuated by higher ATGL expression (76). In immune cells, higher ATGL levels increase the inflammatory response trough peroxisome proliferator-activated receptor (PPAR) signalling, whereas it reduces inflammatory signalling in many non-immune cells like hepatocytes and adipocytes (77).

Alpha/beta hydrolase domain containing protein 5, comparative gene identification 58 (*ABHD5*/CGI-58)

CGI-58 is a major player in the lipolytic cascade by co-activating ATGL. The enzymatic activity of ATGL in liver is decreased by ~73 % in CGI-58$^{-/-}$, compared to CGI-58 wild-type (wt) mice (65). Liver specific CGI-58 KO mice show exacerbated NAFLD, including NASH and liver fibrosis on western-type diet (78).

Loss of CGI-58 functionality in humans has more pronounced consequences than loss of ATGL. Humans with a mutation in the ABHD5 (CGI-58) gene (Chanarin-Dorfman syndrome) experience steatosis, ichthyosis, and skeletal myopathy (62). This highlights that even though CGI-58 and ATGL are functionally connected in lipid catabolism, genetic loss, or loss of function, of either ATGL or CGI-58 does not result in the same outcome. This suggests CGI-58 that might have additional functions outside ATGL activation (79).

Although CGI-58 features a serine-hydrolase catalytic triad in its AB hydrolase fold (76), similar to the catalytic dyad of ATGL, the enzymatic function of CGI-58 remains obscure. CGI-58 might have an ATGL independent lysophosphatidic acid acyltransferase function (77), or no enzymatic function at all.

Lipid droplet accumulation by CGI-58 loss might help to clear cytosolic lipotoxic lipid species (80)[18] and induce a shift towards an aerobic glycolytic phenotype (Warburg effect[19]) (82). Low levels of CGI-58 were found to promote aggressiveness of colorectal tumours (82,83), prostate cancer (84), and shows oncogenic potential in endometrial cancer (85). Despite these findings, there have been no reports of HCC cases in patients with Chanarin Dorfman syndrome (86). However, it is important to note that there are only ~120 reported cases of Chanarin Dorfman syndrome in total.

Patatin-like phospholipase domain-containing protein 3 (*PNPLA3*)

PNPLA3 is related to ATGL (*PNPLA2*), sharing ~39 % protein sequence homology[20], although the enzymatic function of PNPLA3 remains largely unclear to this day. Even though PNPLA3 is categorized as a lipase (like ATGL), loss of PNPLA3 does not alter lipid metabolism in mice (87).

A common pathological mutation of PNPLA3 is the exchange of isoleucine at position 148 to methionine (I148M) (88). This mutation increases PNPLA3 affinity for CGI-58, thereby reducing ATGL-CGI-58 interaction, subsequently reducing lipolysis (89), and has far reaching implications in the development of NAFLD and HCC (90). PNPLA3 I148M increases the frequency of steatosis to 33 % with a homozygous I148M mutation and 26 % with a heterozygous PNPLA3 mutation, compared to 15 % in PNPLA3 I148I control groups (in patients with a high prevalence of existing NAFLD) (91). The risk for HCC development is 2.2-fold increased in patients with homozygous I148M mutation in the PNPLA3 gene, compared to PNPLA3 wt (92). The frequency with which the PNPLA3 I148M in humans is present depends on geographic location. For example, people of Hispanic heritage have the highest rate of PNPLA3 I148M

[18] In this article, LD accumulation was induced by ATGL depletion.

[19] The Warburg effect, named after the German biochemist Otto Warburg, is a metabolic phenomenon observed in many different types of cancer. It is characterized by an increased rate of cytosolic glycolysis, despite the presence of oxygen (aerobic glycolysis). The decrease in efficiency (ATP production per glucose molecule) in this altered pathway is compensated by the increased usefulness of glycolysis products for cellular proliferation. Consequently, mitochondrial structure is negatively affected by the Warburg effect (81).

[20] Data from National Centre for Biotechnology Information (NCBI) Needleman-Wunsch global align protein sequences of NP_065109.1 (PNPLA2) and NP_079501.2 (PNPLA3).

occurrence of 49 %, while European Americans and African Americans show only 23 % and 17 % occurrence, respectively (88).

CHAPTER ONE: THE ROLE OF

LIPID METABOLISM IN HEPATOCYTES

2 Introduction to lipid metabolism in hepatocytes

Both ATGL and CGI-58 play an important role in liver lipid metabolism. Loss of either protein in hepatocytes leads to an accumulation of cytosolic LD. Although there are other enzymes with TG lipolysis function, loss of ATGL might not be fully replaceable, while loss of CGI-58 is generally more severe.

ATGL protein expression is classified as medium[21] in liver, lung, and adipose tissue, and low in skeletal and heart muscle. ATGL liver RNA expression is 58.4 nTPM[22] (normalized transcripts per million). The highest ATGL mRNA expression is found in adipose tissue (508.1 nTPM). Lung and skeletal muscle show medium- to high ATGL mRNA expression (57.3 nTPM in lung, 194.6 nTPM in skeletal muscle). Both HepG2 (59.1 nTPM) and Hep3B (66.0 nTPM) cells show similar ATGL mRNA expression levels.

CGI-58 protein expression is very low (not detected) in liver cells, compared to other tissues (high in brain, kidney, and pancreas, medium in lung, and adipose tissue, low in skeletal muscle). ABHD5 (CGI-58) RNA expression in the liver is 21.7 nTPM, compared to 38.8 nTPM in adipose tissue and 16.4 nTPM in lung. ABHD5 mRNA expression is lower in Hep3B cells (2.5 nTPM) compared to HepG2 cells (5.4 nTPM).

PNPLA3 protein is only detected in liver (medium expression) and kidney (high expression). PNPLA3 mRNA expression is highest in the liver (31.0 nTPM), compared to adipose tissue (2.6 nTPM), lung (0.8 nTPM) and kidney (4.5 nTPM). Both HepG2 and Hep3B cells show similar PNPLA3 expression (Hep3B 12.0 nTPM, HepG2 14.3 nTPM). It is important to note that Hep3B cells express non-pathologic PNPLA3 wt, whereas HepG2 cells homozygously express the pathological PNPLA3 I148M variant.

ATGL (chapter 0), CGI-58 (chapter 0), and PNPLA3 (chapter 0) play a role in liver disease and possibly in liver cancer. ATGL (72) and PNPLA3 (87) loss in humans show little

[21] Data from human protein atlas www.proteinatlas.org (93) on tissue protein expression. Expression is classified into 4 categories: not-detected, low, medium, high.
[22] Data from human consensus expression dataset consisting of protein atlas (www.proteinatlas.org) (93) and Genotype-Tissue Expression (GTEx) transcriptomics datasets.

consequences in liver health, although higher ATGL expression could have a protective effect on liver cancer (76). Changes in the expression of non-pathologic PNPLA3 wt is not associated with liver disease in mice (87). However, the expression of the pathologic PNPLA3 I148M variant shows a strong correlation with a decrease in liver health and increased liver cancer risk (94). Lastly, low CGI-58 expression shows a detrimental effect on liver health and might be a risk-factor for the development of liver cancer (62).

Taken together, liver health is affected by the expression of ATGL, CGI-58, and PNPLA3, although there are major differences how these proteins affect liver health. It is therefore necessary to take a closer look at each of these proteins individually to determine their role in liver disease.

3 Material and Methods

Parts of this section have been adapted from Schinagl *et al* 2021 (1).

3.1 Cell Culture

HepG2 cells from the CellBank Graz at the Medical University of Graz, Austria, and Hep3B cells generously provided by Prof. Michael Trauner's lab at the Medical University of Vienna, Austria, were cultured in RPMI-1640 or high-glucose Dulbecco's Modified Eagle Medium (DMEM D6546) from Sigma-Aldrich, USA. The culture media were supplemented with 2 mM L-glutamine from Gibco, Thermo Fisher, USA (25030081), and 10% FBS from Gibco (F7524). Plastic dishes (surface treated 734-2323 VWR, Radnor, Pennsylvania, USA) were used for cell culturing. The cells were maintained at 37 °C with 5 % CO_2 and 20 % O_2. Sub-culturing of HepG2 and Hep3B cells was performed every 72 h at a 1:5 ratio, and experiments were conducted after at least two passages of subculturing. Cell lines were used for a maximum of 15 passages after seeding. The CASY (OMNI live science, Germany) and EVE cell counting systems (NanoEntek, USA) were employed to ensure equal numbers of cells were seeded. For western blot and proteomic analysis, HepG2 and Hep3B cells were harvested 24 h after seeding.

3.2 Protein overexpression and knock-down

HepG2 ATGL and ATGL S47A overexpression (OE), Hep3B CGI-58 OE, GFP OE, CGI-58 KD and control, in addition to Hep3B PNPLA3 I148M and PNPLA3 wt OE was achieved using custom designed lentiviral vectors by Vector Builder (Chicago, USA) (For vectors see Figure 6 A-H) and cells were selected using either G418 (Thermo Fisher, USA, 10131035) (ATGL OE, ATGL S47A OE, PNPLA3 I148M and I148I) or Hygromycin B (Thermo Fisher, USA, 10687010) (CGI-58 OE, GFP OE, CGI-58 KD, CGI-58 control). Protein expression was confirmed via western blotting after at least 14 days of selection.

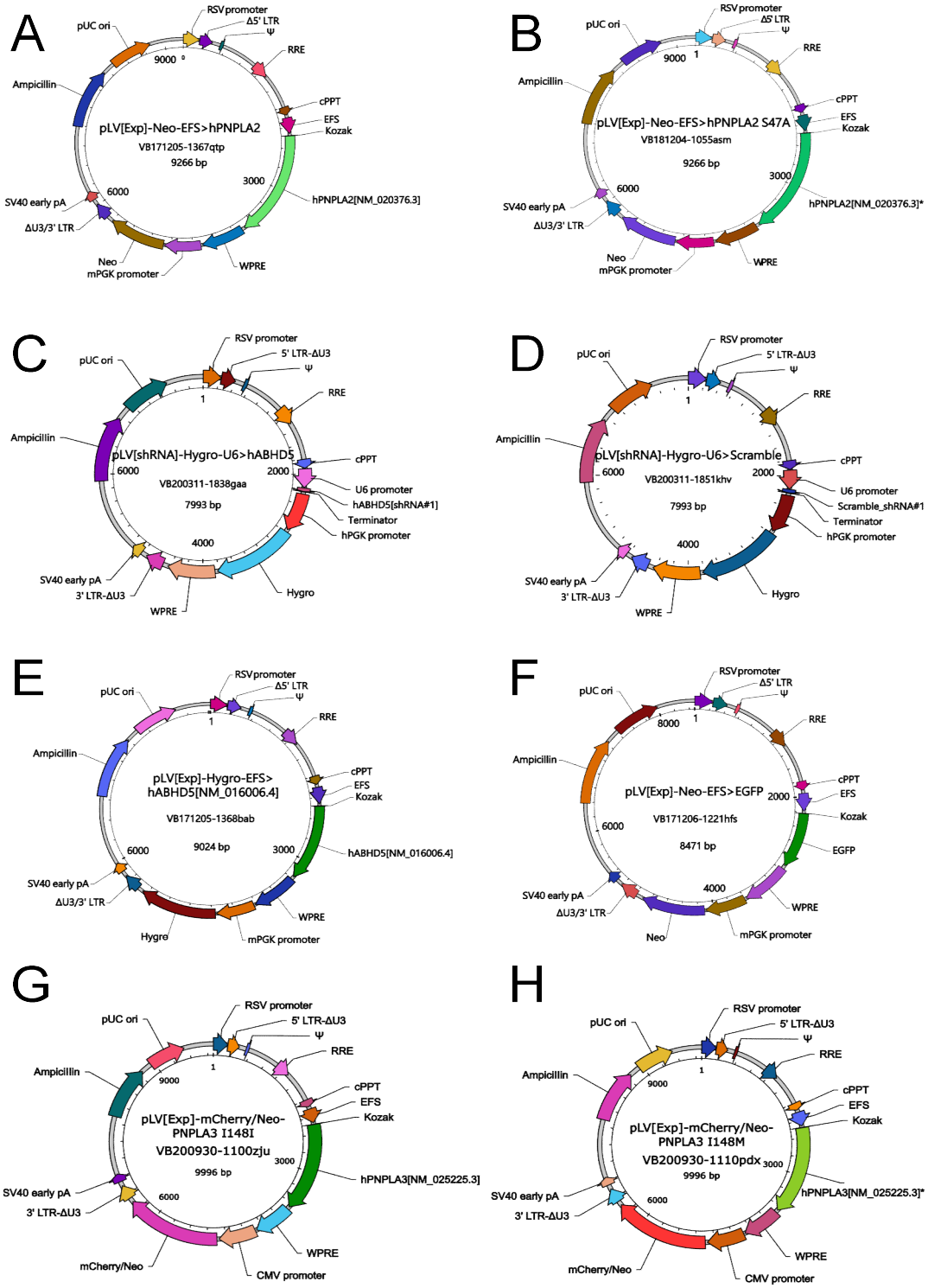

Figure 6: Lentiviral vectors for modifying ATGL (PNPLA2), CGI-58 (ABHD5) and PNPLA3 expression. (A) ATGL OE. **(B)** ATGL S47A OE. **(C)** CGI-58 small hairpin RNA (shRNA) KD. **(D)**

CGI-58 KD control (scramble shRNA). **(E)** CGI-58 OE. **(F)** GFP OE. **(G)** PNPLA3 wt OE **(H)** PNPLA3 I148M OE. pLV: lentivirus vector, Exp: expression, Neo: neomycin resistance (G418), EFS: elongation factor 1alpha binding sequence, h: human, EGFP: enhanced green fluorescent protein (GFP).

3.3 Proliferation Assay

Hep3B cells were distributed into individual wells of 96-well plates, with each well containing 10,000 cells in 100 µL of DMEM with 10 % FBS. After 24 hours, the medium in each well was replaced with 100 µL of fresh DMEM with 10 % FBS. The proliferation of cells was evaluated every 24 hours using the cell counting kit 8 assay (CCK 8, 96992) from Sigma-Aldrich, St. Louis, MO, USA, following the provided protocol.

3.4 Western Blotting Analysis

HepG2 and Hep3B cells were harvested after 24 hours of incubation in 10% FBS when they reached approximately 85% confluency. For ATGL, CGI 58, or PNPLA3 expression analysis, HepG2 and Hep3B cells were harvested after 48 hours of incubation in 10% FBS DMEM. The cells were lysed in CST lysis buffer (9803) from Cell Signaling Technologies, Danvers, MA, USA, supplemented with a protease inhibitor cocktail (P8340) from Sigma Aldrich. SDS-PAGE 4 to 12% Bis-Tris gels (WG1401A) with a thickness of 1.0 mm from NuPage, Thermo Fisher, Waltham, MA, USA, were used to separate equal amounts of protein using 1x MES-SDS running buffer (AB349824) from abcr, Karlsruhe, Germany. The gel electrophoresis was conducted at a constant voltage of 200 V for 45 minutes on ice. Semi-dry blotting onto nitrocellulose membranes (IB23001) from Invitrogen, Thermo Fisher, was performed using the iBlot 2 system (Thermo Fisher) at 7 V for 30 minutes. The membranes were blocked with protein-free (PBS) blocking buffer (37572) from Thermo Fisher for 1 hour at room temperature. Primary antibodies (vinculin from Invitrogen, clone 7F9; CGI-58 from Abnova, catalog number H00051099-M01; PNPLA3 from Thermo Fisher, catalog number 16809965) were incubated overnight at 4°C, and secondary antibodies (horse anti-mouse 7076 and goat anti-rabbit 7074S) from Cell Signaling Technologies were incubated at room temperature for 1 hour. Chemiluminescent detection agent Super-Signal West Pico PLUS (34577) from Thermo Fisher was used as the

substrate, and the detection was performed using a ChemiDoc MP or XRS+ system (BioRad, Hercules, CA, USA). Image analysis was conducted with Image Lab software (BioRad).

3.5 Proteomic Analysis

Hep3B cells were collected using cell scrapers after 24 hours of incubation in 10 % FBS DMEM when they reached approximately 90 % confluency. For CGI-58 (KD or OE) expression analysis or PNPLA3 over-expression analysis, Hep3B cells were cultured for 24 h in 10 % FBS DMEM. The cells were washed with PBS and lysed using an in-house reducing and alkylating buffer consisting of 100 mM TRIS HCl (pH = 8.5), 1% sodium dodecyl sulphate, 10 mM tris(2-carboxyethyl) phosphine, and 40 mM 2-chloroacetamide. After sonication (1 kJ), the samples were heated to 95 °C for 10 min. A total of 100 µg of protein per sample (determined using the bicinchoninic acid assay protein estimation, BCA, from Thermo Fisher Scientific, compatible with reducing agents) were subjected to acetone precipitation by adding NaCl to a final concentration of 10 mM. Then, 4x volumes of acetone were added and incubated for 10 min. The supernatant was removed after centrifugation (10 min at 14,000 g). The dried samples were dissolved in 25 % trifluoroethanol (TFE) in 100 mM Tris HCl (pH = 8.5) and sonicated until completely dissolved. For protein digestion, the samples were diluted to 10 % TFE using 100 mM ammonium bicarbonate (ABC). Sequencing Grade Modified Trypsin (V5111) from Promega, Walldorf, Germany, was added at a 1:100 enzyme-to-protein ratio, and digestion was carried out overnight at 37 °C. The samples were desalted the next day using in-house prepared polystyrene-divinylbenzene, reversed-phase sulfonate stage tips (66886) from Supelco, Thermo Fisher, and resuspended in 0.1% formic acid. Chromatography was performed using an Ultimate 3000 RCS Nano Dionex system from Thermo Fisher, equipped with an Aurora Series UHPLC C18 column (250 mm × 75 µm, 1.6 µm) (AUR2-25075C18A) from Ionoptics, Fitzroy, Australia. Separation was achieved with a linear gradient of H_2O (solvent A) and acetonitrile, both with 0.1 % formic acid added (solvent B) (0 - 5.5 min 2 % B; 65.5 min 17 % B; 95.5 min 25 % B; 105 min 37 % B; 115.5 - 125.5 min 95 % B; 126 - 136.5 min 2 % B) at a flow rate of 0.4 µL/min. The column temperature was maintained at 40 °C. Mass spectrometric analysis was conducted using a timsTOF Pro instrument from Bruker Daltonics, Billerica, Massachusetts, USA, operating in positive data-dependent Parallel Accumulation-Serial

Fragmentation (PASEF) (95) mode with enabled trapped Ion Mobility Spectrometry (TIMS) at a 100% duty cycle (100 ms cycle time). The source capillary voltage was set to 1500 V, and the dry gas flow was 3 L/min at 180 °C.

3.6 Proteomic Data Analysis

Data analysis, database search and protein quantification were performed with MaxQuant version 2.01.0 (96); and statistical data analysis with Perseus version 1.6.14.0 (97). Search criteria for MaxQuant: false discovery rate (FDR) for peptide, peptide-to-spectrum as well as protein matches was set to 1 %. Peptide tolerance was set to ± 20 and ± 4.5 for the first and main peptide search, respectively. Product mass tolerance was set to ± 0.5 Da. Cysteine carbamidomethylation was set as static whereas methionine oxidation and N-terminal acetylation were set as dynamic modifications. Minimum required peptide length was six amino acids and maximum number of allowed tryptic mis-cleavages was two. For protein search, the SwissProt human FASTA file (downloaded on 30 November 2020 from https://www.uniprot.org, 20,434 entries) containing most common protein contaminants was used as a database. Label-free protein quantitation (LFQ) was performed with a minimum of two peptides per protein (unique and razor) as quantitation requirement. Match between runs was enabled in the retention time window of 1 min and alignment window of 20 min respectively. LFQ values were log2 transformed (resulting in invalid values [NaN] for any missing value), and contaminants were removed. Further data analysis and graphical interpretation of protein networks was performed using Cytoscape (98) v3.8.2. STRING (99) v11.5 was used to generate protein networks using the following parameters: Homo Sapiens, full STRING network, medium confidence (0.4), medium FDR stringency (0.05). Imputation histograms can be found in the appendix (Figure 29). The proteomics data for Hep3B CGI-58 KD, OE and PNPLA3 I148M experiments were deposited to the ProteomeXchange consortium via the PRIDE (100) partner repository with the dataset identifier PXD042879.

3.7 Lipid Droplet Analysis

125.000 HepG2 or Hep3B cells were seeded onto glass cover slips (ROTH, 18 × 18 mm, thickness 0.13 – 0.16 mm) in 6-wells in 10 % FBS DMEM. The next day, the medium was

replaced by fresh 10 % FBS DMEM. After 24 h of additional incubation, LD were stained with BODIPY (4,4-difluoro-4-bora-3a,4a-diaza-s-indacene) 493/503 (D3922, Invitrogen, Thermo Fisher) for 10 min at 37 °C and then washed twice with pre-warmed PBS. After that, cells were fixed with 3.7 % formaldehyde for 10 min at 37 °C and nuclei received DAPI (4',6-diamidino-2-phenylindole) staining (H-1200-10, Vector Labs, Newark, California, USA). Cover slips were placed onto glass slides (ROTH) and imaged on a Nikon A1 confocal microscope. LD volume was calculated using an in-house FIJI (101) script by Juergen Gindlhuber.

4 Results

4.1 ATGL expression affects hepatocyte lipid droplet metabolism

To better understand the impact of ATGL expression in liver cancer, we investigated the expression levels of ATGL in liver tumour tissue and healthy tissue using the UCSC Xena-Browser[23]. The National Cancer Institute "Genomic Data Commons" (GDC) "The Cancer Genome Atlas" (TGCA) liver cancer (LIHC) dataset was used to assess ATGL expression in liver cancer, whereas the GDC all cancer dataset was used to assess ATGL expression in all types of cancer. Statistical analysis of available data (null-value gene expression data removed) for calculating survival was performed using Kaplan-Meier; Welch's test (two-sided) comparing gene expression in solid tissue (primary tumour vs. solid tissue normal). GDC TGCA Liver Cancer dataset: 421 samples total, 371 primary tumour, 50 solid tissue normal; GDC all cancer PANCAN dataset: 10828 samples total, 10087 primary tumour, 741 solid tissue normal.

Even though lower ATGL expression is not associated with a change in survival rate (Figure 7 A), decreased levels of ATGL expression are found in primary liver cancer, compared to normal tissue (Figure 7 B). All cancer mortality is slightly increased with lower ATGL expression, compared higher ATGL expression (Figure 7 C) and overall ATGL expression in cancer is likewise decreased (Figure 7 D).

[23] https://xenabrowser.net/ (102)

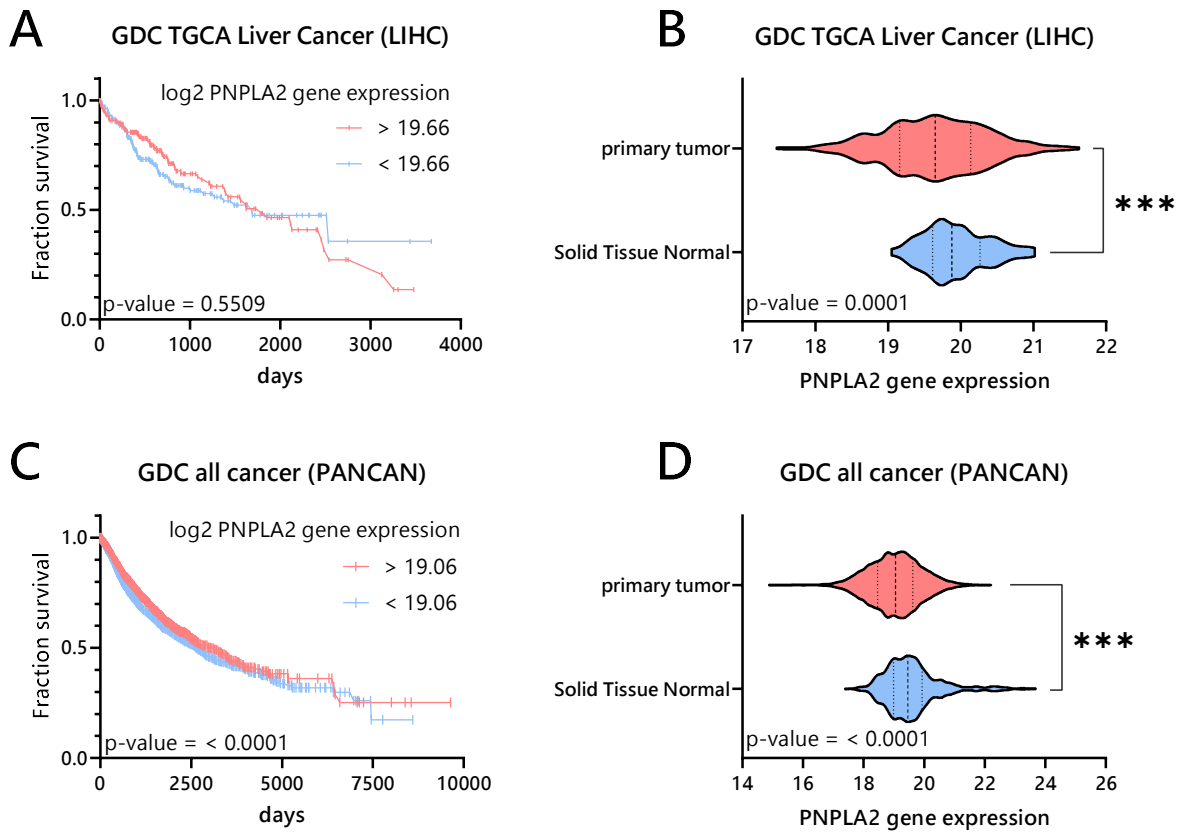

Figure 7: ATGL expression in relation to liver cancer survival and occurrence. (**A**) ATGL expression in relation to liver cancer survival, over time. (**B**) ATGL expression in liver cancer, compared to healthy tissue (Solid tissue normal). (**C**) ATGL expression in relation to survival in all cancer types (tissue types), over time. (**D**) ATGL expression in all cancer types (tissue types), compared to healthy tissue (Solid tissue normal). Data from UCSC XENA browser. Statistical significance calculation in **A**, **C** Kaplan-Meier; **B**, **D** Welch's test. GDC TGCA Liver Cancer dataset: 421 samples, GDC all cancer PANCAN dataset: 10828 samples. (*** $p < 0.001$)

Although the role of ATGL in cancer is still controversial and might depend on the type of tissue of the primary tumour (see chapter 0), the role of ATGL as a TG hydrolase is well established. Since TG hydrolysis plays an important role in NAFLD, we therefore assessed the enzymatic function of ATGL in hepatocytes with either enzymatically non-functional ATGL S47A or ATGL OE. HepG2 ATGL OE and ATGL S47A OE were created using lentiviral transfection of HepG2 cells (Figure 6**Error! Reference source not found.** A, B). After selection with

geneticin[24] (G418), western blotting revealed 7-fold and 6-fold increase expression of ATGL and ATGL S47A over ancestral HepG2 ATGL expression, respectively (see Figure 8 B).

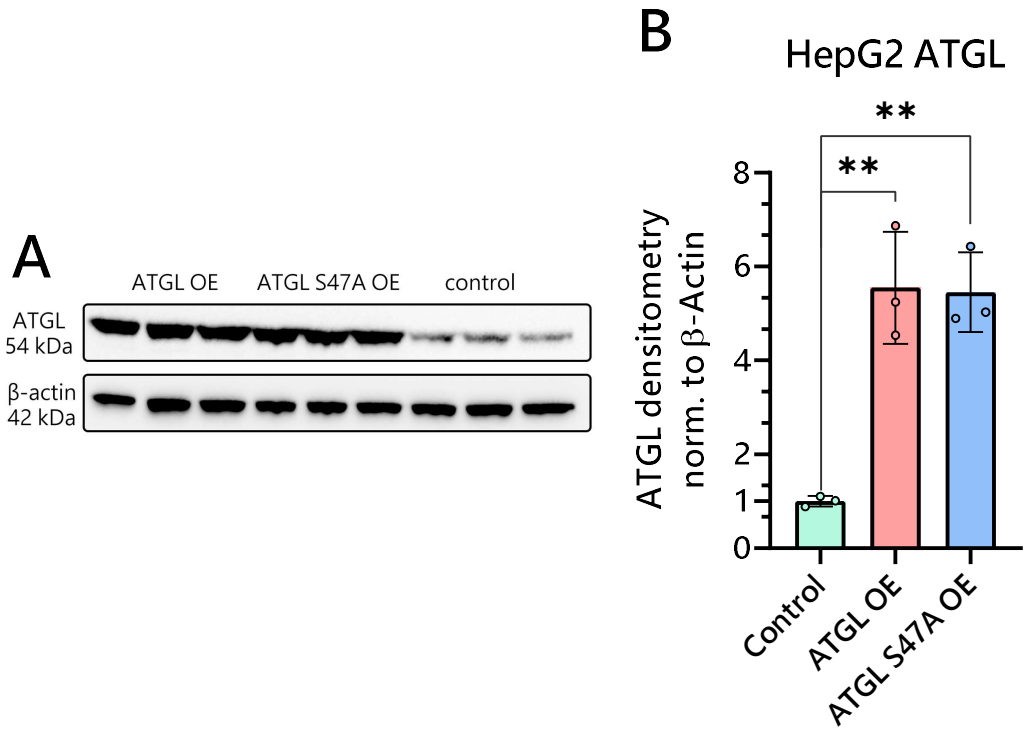

Figure 8: Western blot for ATGL over-expression (OE) and ATGL S47A OE in HepG2 cells, compared to controls. (A) Demonstration of western blot ATGL protein expression. 3 samples per group. **(B)** One-way ANOVA statistical analysis of HepG2 ATGL expression with multiple comparisons, densitometry normalized to β-actin (** p-value < 0.01).

Next, we assessed the role of ATGL as a TG hydrolase in HepG2 cells. For this, we stained LD in HepG2 ATGL OE, ATGL S47A OE and ancestral[25] "control" HepG2 cells using BODIPY, after seeding equal numbers of cells in biological triplicates. Lipid loading via oleic acid is not necessary in hepatocytes as they actively producing TG via *de novo* lipogenesis and 10 % FBS DMEM contains sufficient amounts of lipids. HepG2 cells were imaged on a Nikon confocal

[24] Suitable for neomycin selection of cells by blocking the translational step in peptide synthesis (elongation step) at the ribosome.
[25] Ancestral cell lines describe genetically unaltered "pure" cell lines.

microscope with 10-15 images of 2-4 cells in z-direction. Afterwards, z-stacks were imported into ImageJ and LD volume analysis was performed via an in-house script. LD volume was normalized per cell (identified via DAPI stained nuclei). Although ATGL OE only slightly reduced LD volume, compared to HepG2 controls (two-sided t-test, p = 0.045), the enzymatically inactive variant ATGL S47A significantly (two-sided t-test, p = 0.0085) increased the accumulation of LD, compared to HepG2 controls (see Figure 5). It is important to note that HepG2 cells are homozygous for the PNPLA3 I148M variant, therefore possibly reducing the basal activity of ATGL in these cells (see chapter 0).

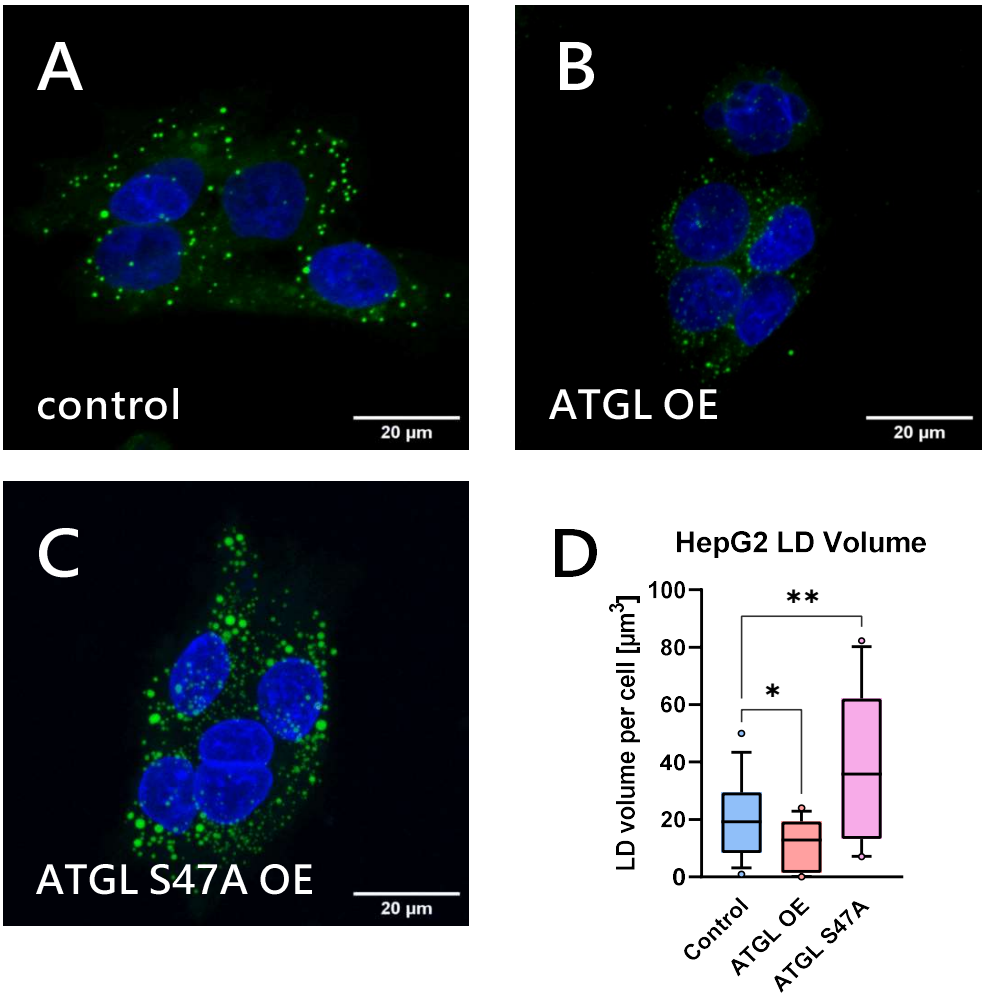

Figure 9: ATGL OE in HepG2 cells results in the reduction of LD volume, whereas expression of the enzymatically dead ATGL S47A increases LD volume. LD in HepG2 cells labelled with BODIPY (green), nuclei stained with DAPI (blue). **(A)** Compared to control, **(B)** ATGL OE cells

slightly lower HepG2 LD volume. **(C)** ATGL S47A OE increases LD accumulation in HepG2 cells, compared to controls. **(D)** Two-sample t-test (two-sided) statistical analysis of LD volume. n = 15 measurements for control and ATGL S47A OE, n = 16 measurements for ATGL OE (* p-value < 0.05, ** p-value < 0.01).

Although ATGL OE and ATGL S47A OE, compared to control, resulted in significant ($p < 0.05$) differences in LD volume, growth analysis did not detect differences between these groups (Figure 10). This suggests ATGL expression and enzymatic function might not be involved in critical proliferative processes in HepG2 cells. We therefore opted to investigate a higher regulatory level of lipid metabolism by varying expression of CGI-58 in Hep3B cells, which express non-pathologic PNPLA3 wt, therefore not interfering with the co-activating of ATGL by CGI-58.

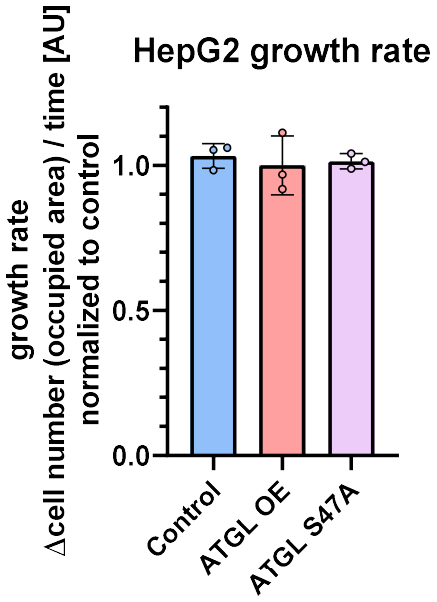

Figure 10: HepG2 growth rate (slope) is not affected by ATGL activity. Compared to HepG2 control, HepG2 ATGL OE and HepG2 ATGL S47A cells did not show increased growth. Growth was assessed as a function of HepG2 occupied area during a linear growth rate from 13 h to 35 h after seeding.

4.2 CGI-58 is involved in lipid and glucose metabolism in Hep3B cells

HepG2 cells express a PNPLA3 variant which is suspected to supress ATGL enzymatic function by sequestering CGI-58 (89), we therefore continued our experiments using Hep3B cells which carry the non-pathological I148I (wt) PNPLA3 variant. In these cells, we knocked-down (KD) or over-expressed CGI-58, which we expected to show a stronger effect in LD catabolism, compared to ATGL.

Similar to ATGL, lower CGI-58 (ABHD5) expression is not related to a decrease in survival in liver cancer patients (Figure 11 A). However, data from the GDC TGCA liver cancer dataset (see chapter 4.1 above) suggests CGI-58 expression is decreased in primary liver tumours, compared to healthy liver tissue (Figure 11 B). Although CGI-58 expression is not associated with liver cancer survival, higher CGI-58 expression levels indicate decreased survival for overall cancer, compared to lower CGI-58 expression levels (Figure 11 C). Akin to liver cancer CGI-58 expression, all-cancer expression of CGI-58 is lower, compared to healthy tissue (Figure 11 D).

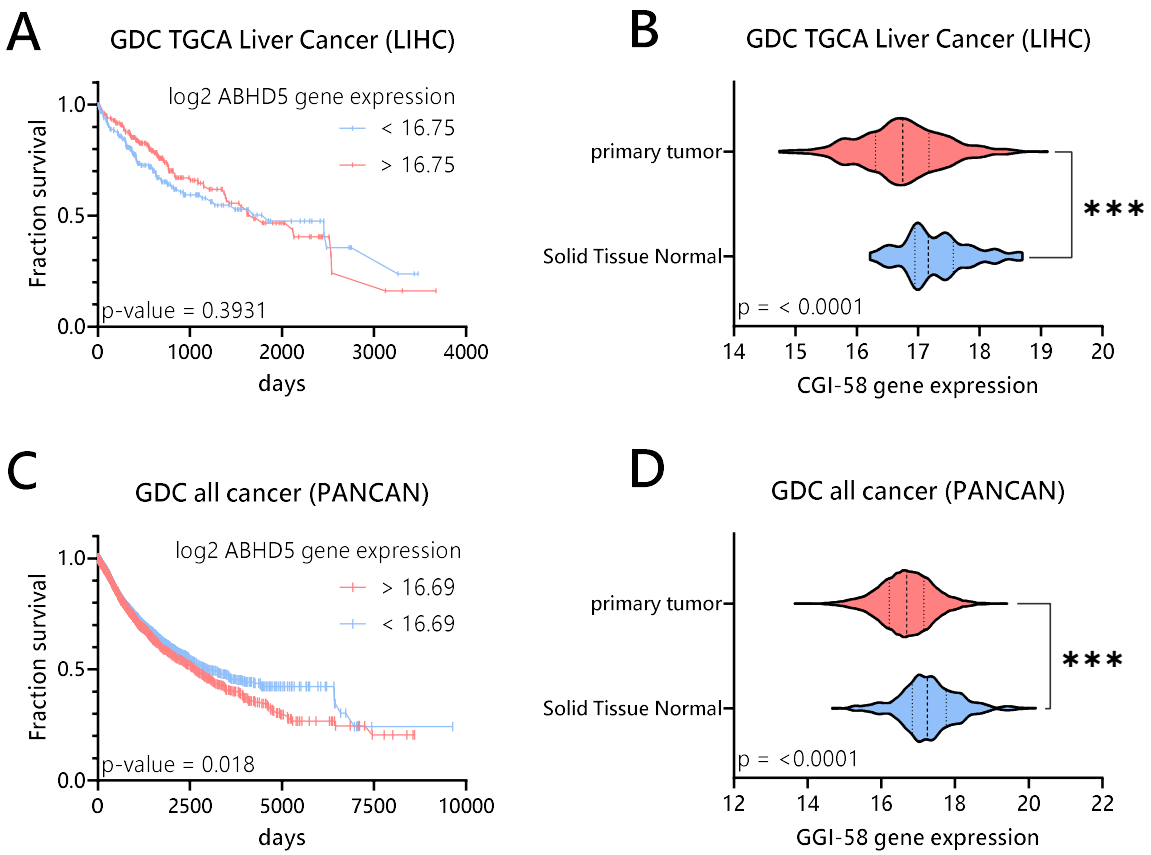

Figure 11: CGI-58 expression in relation to liver cancer survival and occurrence. (A) CGI-58 expression in relation to liver cancer survival over time. **(B)** CGI-58 expression in liver cancer, compared to healthy tissue (Solid tissue normal). **(C)** CGI-58 expression in relation to survival in all cancer types (tissue types) over time. **(D)** CGI-58 expression in all cancer types (tissue types), compared to healthy tissue (Solid tissue normal). Data from UCSC XENA browser. Statistical significance calculation in **A, C** Kaplan-Meier; **B, D** Welch's test. GDC TGCA Liver Cancer dataset: 421 samples, GDC all cancer PANCAN dataset: 10828 samples. (*** $p < 0.001$).

Hep3B CGI-58 KD and control cells we prepared using lentiviral transfection of Hep3B cells (Figure 6**Error! Reference source not found.** C, D). Hep3B control cells were created using a scramble shRNA sequence CCTAAGGTTAAGTCGCCCTCG (103), which does not interfere with any known human mRNA, while CGI-58 KD cells were created using the following shRNA target

sequence: GCAGCGTTTAAGGCCTGATTT. After selection with hygromycin B[26], western blotting of Hep3B CGI-58 KD cell lysate showed ~ 50 % reduction of CGI-58 expression, compared to control.

Hep3B CGI-58 OE and GFP control cells were created likewise using lentiviral transfection of Hep3B cells (Figure 6**Error! Reference source not found.** E, F), whereas Hep3B CGI-58 OE cells display a 60-fold increase in CGI-58 expression (Figure 12 A, B), compared to GFP controls.

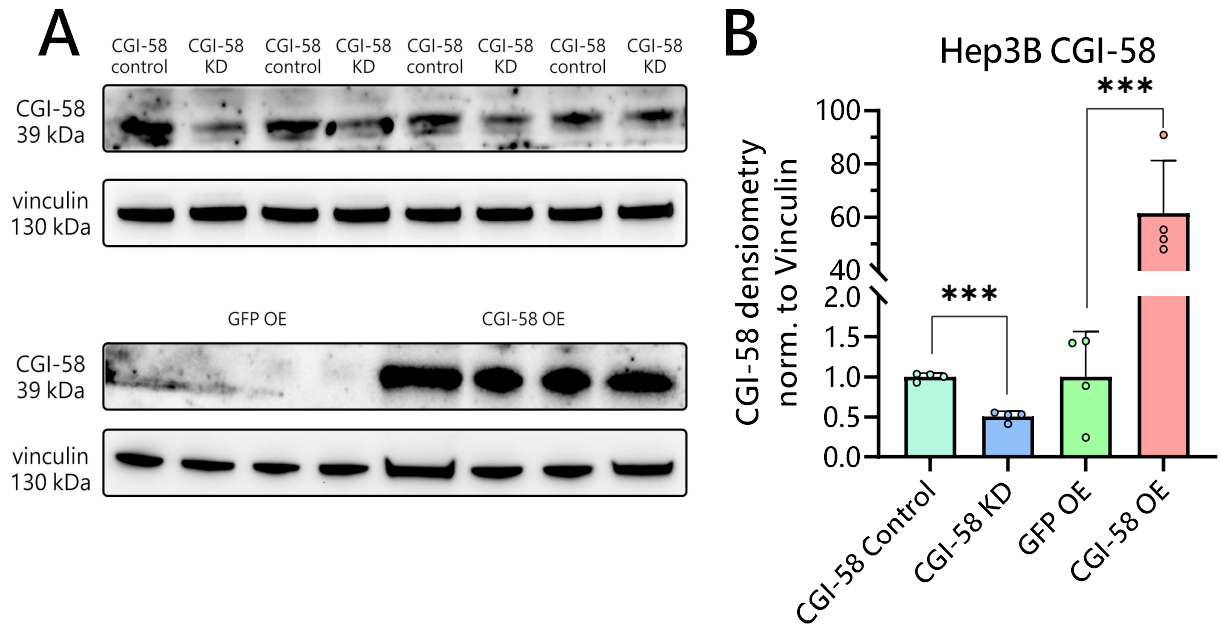

Figure 12: Western blot for CGI-58 knock-down and CGI-58 OE in Hep3B cells, compared to controls. (A) Demonstration of western blot CGI-58 protein expression. 4 samples per group. GFP OE and CGI-58 OE were imaged under different conditions, compared to CGI-58 KD and controls, showing little CGI-58 expression in GFP OE cells due to short exposure time. **(B)** One-way ANOVA statistical analysis of Hep3B CGI-58 expression with multiple comparisons, densitometry normalized to Vinculin (** p-value < 0.01). Compared to control, a ~50% decrease of

[26] Hygromycin B is an aminoglycoside antibiotic which inhibits the translational step in peptide synthesis (elongation) at the ribosome (104).

CGI-58 expression was shown in Hep3B CGI-58 KD cells. Hep3B CGI-58 OE cells showed a 60-fold increase in CGI-58 expression.

After WB analysis confirmed sufficient KD and OE of CGI-58 in Hep3B cells, we investigated the effects of CGI-58 increase and reduction in the context of TG hydrolysis via LD volume analysis in Hep3B cells. This was accomplished by staining LD in Hep3B cells with BODPIY, after seeding equal amounts of Hep3B CGI-58 KD, control, OE and GFP control cells, similar to LD staining of HepG2 cells (see chapter 4.1 above).

LD volume analysis (One-way ANOVA, multiple comparisons with Sidak multi-testing correction) of Hep3B cells revealed significantly increased volume in CGI-58 KD cells (Figure 13 B), compared to controls (Figure 13 A). Hep3B CGI-58 OE cells showed a major reduction in LD volume (Figure 13 D), compared to GFP controls (Figure 13 C). Although Hep3B GFP OE cells express GFP which shows similar excitation-emission spectra to BODIPY, due to the low abundance of GFP proteins, compared to BODIPY, and the high quantum yield of BODIPY[27] it is possible to distinguish LD from cytosolic GFP fluorescence.

These results suggest CGI-58 plays a major role in lipid metabolism in hepatocytes. As expected, higher CGI-58 expression correlates with lower LD volume. This effect was only observed in a much-reduced form in ATGL OE (Figure 9), suggesting CGI-58 co-activation is more influential on TG hydrolysis, compared to plain ATGL protein overabundance. To further study differences caused by different levels of CGI-58 expression in hepatocytes, we performed label-free quantitative shot-gun proteomic analysis of our Hep3B CGI-58 constructs.

[27] The quantum yield describes the chance of a photon getting absorbed by a molecule and re-emitted as a lower-wavelength photon. Higher quantum yield translates to more desirable properties for microscopy, in this case of BODIPY.

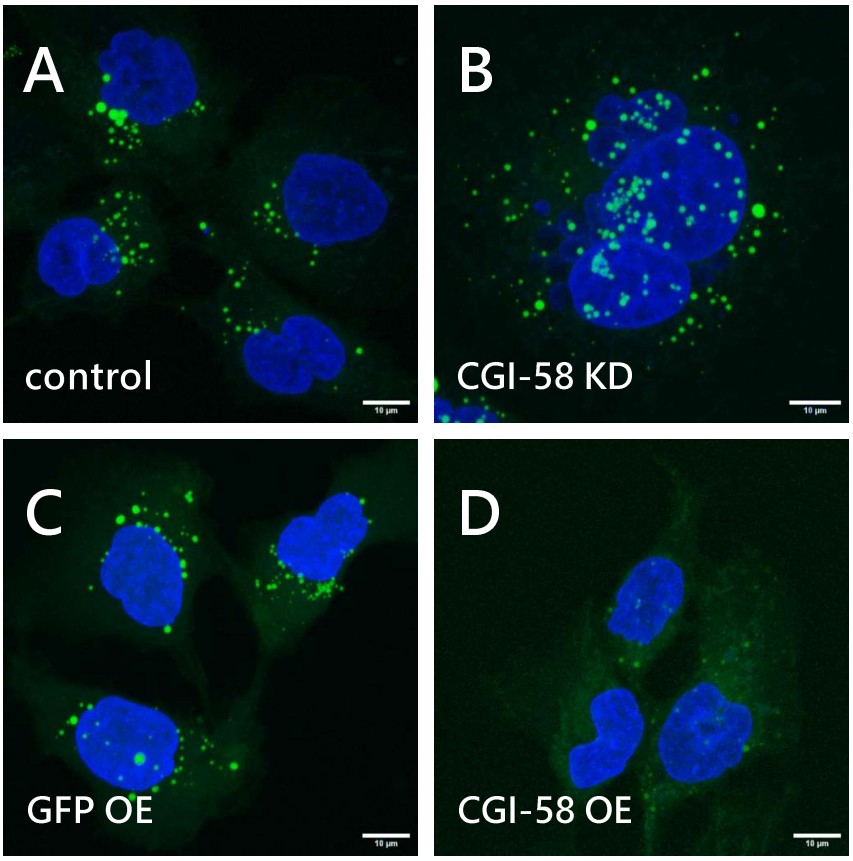

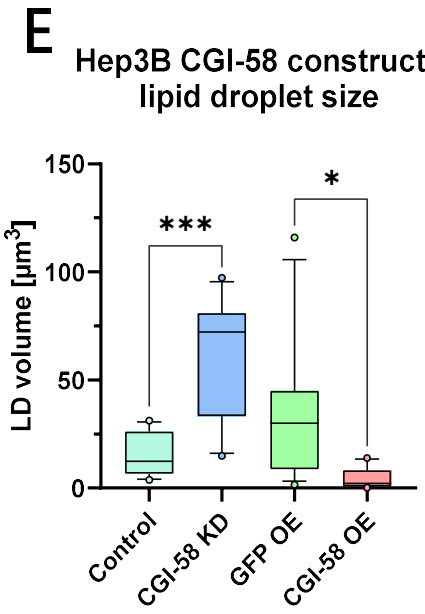

Figure 13: CGI-58 KD results in LD accumulation in Hep3B cells, whereas CGI-58 OE reduces LD volume in Hep3B cells. LD in Hep3B cells labelled with BODIPY (green), nuclei stained with

DAPI (blue). **(A)** Compared to control, **(B)** CGI-58 KD increases LD volume in Hep3B cells. **(C)** Compared to GFP OE control, **(D)** CGI-58 OE drastically reduces LD volume in Hep3B cells. **(E)** One-way ANOVA statistical analysis of LD volume with multiple comparisons. n = 11 measurements for control and CGI-58 KD, n = 10 measurements for GFP OE, n = 12 measurements for CGI-58 OE (* p-value < 0.05, *** p-value < 0.001).

4.2.1 CGI-58 knock-down in Hep3B cells influences proteins related to lipid- and glucose metabolism

Apparent changes in the LD volume upon knock-down of CGI-58 in Hep3B cells (Figure 13 A, B, E) indicates a shift in lipid metabolism. We therefore decided to investigate differences in protein expression between Hep3B CGI-58 KD and control by label-free quantitative proteomics. After pre-processing our data (see Methods), we filtered for at least 7 valid values in total (CGI-58 KD or control, 4 samples per group), reducing our dataset from 4725 to 2456 quantified proteins. Stringent filtering in these large datasets is necessary to ensure the reliability and accuracy of identified proteins and to reduce false positives arising from excessive imputation. Missing values were imputed separately for each column with a width of 0.3 and a down-shift of 1.8.

A two-sample student's T-test (both sides) with $S_0 = 0.1$ and a permutation-based false-discovery rate of 0.05 with 250 randomizations resulted in 10 significantly (q-value < 0.05) differentially expressed proteins between Hep3B CGI-58 KD vs control (see Table 1). A volcano plot of this analysis is shown in Figure 14 A. The function of these 10 significantly (q < 0.05) differentially expressed proteins (Hep3B CGI-58 KD vs. control) is briefly summarized here. GANAB, CALR (105), HSPA1B, and SEC24A (106) are all involved in the processing of proteins in the endoplasmic reticulum. These four proteins are all downregulated in Hep3B CGI-58 KD compared to controls, suggesting impaired protein processing likely caused by shRNA treatment. PEG10 is a protein involved in apoptosis, cell growth and hepatoma formation (107), and also downregulated in Hep3B CGI-58 KD cells compared to controls. CCDC132 is downregulated and involved in the recycling of the transferrin receptor, which is responsible for the import of iron into the cell (108). Lastly, PGM1 is involved in both the breakdown and synthesis of glucose in the liver via the transition of glucose 1 phosphate to glucose 6 phosphate (109).

PGM1 is downregulated in Hep3B CGI-58 KD, compared to controls, suggesting a decreased gluconeogenesis pathway, which might increase the flux of glucose into the cell. EXOSC4 is an exonuclease, which is involved in the degradation of RNA from RNA interference events like shRNA or siRNA (104). EPHB4 plays a role in cell-cell adhesion (109) and is upregulated in Hep3B CGI-58 KD cells compared to controls. EXOSC4 is upregulated in Hep3B CGI-58 KD, compared to controls and has been shown to be amplified in multiple cancer types (105).

Principal component analysis revealed a clear separation between Hep3B CGI-58 KD and control cells (Figure 14 B).

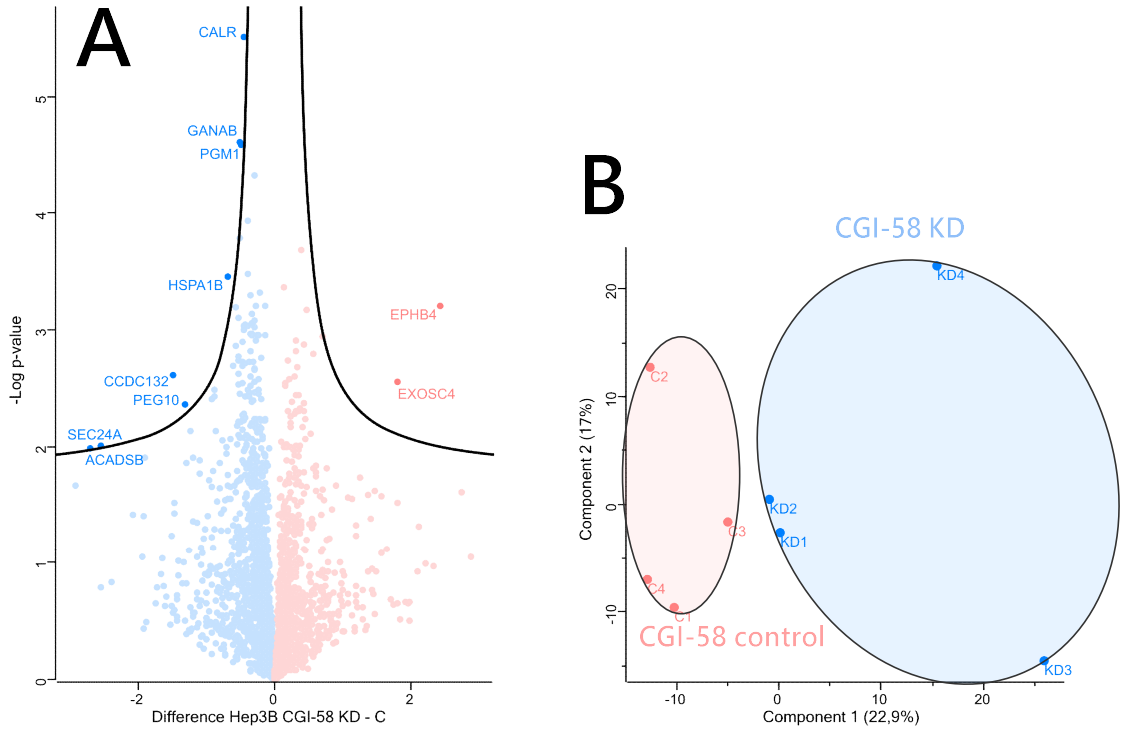

Figure 14: LFQ proteomics data suggests several statistically significant (q-value < 0.05) differentially regulated proteins between Hep3B CGI-58 KD vs. control. n = 4 samples per group. **(A)** Volcano blot of Hep3B CGI-58 KD cells vs. control, LFQ data. Statistical analysis: t-test (two-sided) with multi-testing (permutation-based) corrected FDR = 0.05, $S_0 = 0.1$ plotted as $-Log_{10}$ p-value. Difference in protein expression plotted as log_2 mean on x-axis. Red dots represent proteins with a mean log2 difference of Hep3B CGI-58 KD vs. control > 0, whereas blue dots show mean protein expression log2 difference < 0. **(B)** Principal component analysis of Hep3B

CGI-58 KD vs. control without category enrichment shows a clear separation between the two groups.

Table 1: List of proteins with statistically significant (two-sample t-test, two sided, FDR = 0.05, S_0 = 0.01, q < 0.05) changes in expression Hep3B CGI-58 KD vs. control.

GENE NAMES	PROTEIN NAMES	DIFFERENCE KD - C	P-VALUE KD - C	Q-VALUE KD - C
ACADSB	Short/branched chain specific acyl-CoA dehydrogenase, mitochondrial	-2,71	0,038	1,03E-02
SEC24A	Protein transport protein Sec24A	-2,55	0,035	9,73E-03
CCDC132	Coiled-coil domain-containing protein 132	-1,49	0,063	2,41E-03
PEG10	Retrotransposon-derived protein PEG10	-1,32	0,035	4,40E-03
HSPA1B; HSPA1A	Heat shock 70 kDa protein 1B; Heat shock 70 kDa protein 1A	-0,69	0,031	3,52E-04
GANAB	Neutral alpha-glucosidase AB	-0,52	0,047	2,48E-05
PGM1	Phosphoglucomutase-1	-0,49	0,033	2,56E-05
CALR	Calreticulin	-0,45	0,038	3,10E-06
EXOSC4	Exosome complex component RRP41	1,80	0,094	2,82E-03
EPHB4; EPHB3	Ephrin type-B receptor 4; Ephrin type-B receptor 3	2,43	0,052	6,26E-04

To further analyse proteins which are differentially expressed between Hep3B CGI-58 KD vs control, we expanded our search to proteins excluded in the FDR cut-off of q < 0.05 and analysed the resulting 432 proteins (304 downregulated, 128 upregulated) with a p-value of < 0.05 (Hep3B CGI-58 KD vs. controls). A full list of proteins used for this analysis can be found in Table 4 in the appendix. Using the STRING database (99) protein search ("Proteins with Values/Ranks") with medium (5 %) FDR stringency, our analysis revealed changes in fatty acid metabolism (Figure 15 A) and a downregulation (Hep3B CGI-58 KD vs. control) of mitochondrial matrix proteins (Figure 15 B), among other entries which are displayed in Table 6, Table 7 and Table 8 in the appendix. The corresponding isolated datasets are depicted in volcano plots (Figure 15, Table 2) with a q-value (FDR) cut-off of < 0.05, S_0 = 0.1 with 250 randomizations. Taken together, these two downregulated pathways in Hep3B CGI-58 KD vs. control suggest a shift away from fatty acid metabolism and glucose metabolism in mitochondria towards a more glycolytic phenotype. One of the features of a metabolic shift towards a more glycolytic phenotype is the increased production of lactate in the cytosol and the discharge of lactate into the extracellular space. Often, this shift occurs in cancerous cells and is accompanied by an increased growth rate (81).

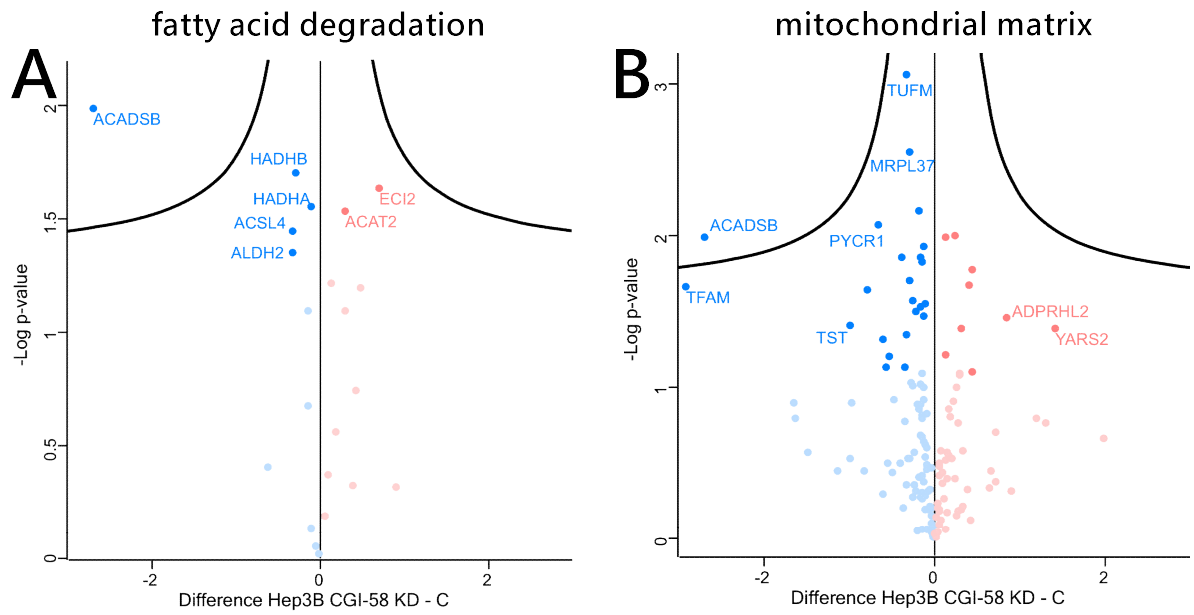

Figure 15: Volcano plots of enriched GO terms in Hep3B CGI-58 KD vs control LFQ data. n = 4 samples per group. Statistical analysis for volcano plots: t-test (two-sided) with multi-testing (permutation-based) corrected FDR = 0.05, S_0 = 0.1 plotted as -Log_{10} p-value with 250 randomizations. Difference in protein expression plotted as log_2 mean on x-axis. Pale dots (red/blue) represent proteins with a p-value > 0.05. Bright dots indicate proteins with a p-value < 0.05. Differences in expression levels are depicted as red (upregulation) or blue (downregulation) in Hep3B CGI-58 KD vs. control. **(A)** KEGG pathway "fatty acid degradation". **(B)** GO cellular component "mitochondrial matrix".

Table 2: List of selected enriched GO terms Hep3B CGI-58 KD vs control using only proteins with a p-value of < 0.05 (two-sided t-test without FDR correction, S_0 = 0.1) for analysis. Both "fatty acid metabolism" and "mitochondrial matrix" terms were identified using the STRING database analysis on differentially expressed proteins between Hep3B CGI-58 KD vs. control with a p-value < 0.05 (t-test (two-sided) without multi-testing correction).

DESCRIPTION	CATEGORY	TERM NAME	FDR	GENES MAPPED / PATHWAY SIZE
FATTY ACID DEGRADATION	KEGG Pathways	hsa00071	0.01	7/42
MITOCHONDRIAL MATRIX	GO Cellular Component	GO:0005759	2.98e-05	32/479

To investigate this possible shift towards a glycolytic phenotype, we evaluated growth and extracellular lactate accumulation in Hep3B CGI-58 KD vs. control cells using a colorimetric growth and extracellular lactate assay, respectively. Interestingly, we identified a ~15 % increase in growth rate of CGI-58 KD cells after 24 h, compared to controls (Figure 16 A) (two-sided t-test, $p < 0.05$). Furthermore, ~20 % increased extracellular lactate levels were measured in Hep3B CGI-58 KD vs. control after 24 h (Figure 16 B) (two-sided t-test, $p < 0.05$). These results suggest a shift towards a slightly increased glycolytic phenotype in Hep3B CGI-58 KD vs. control.

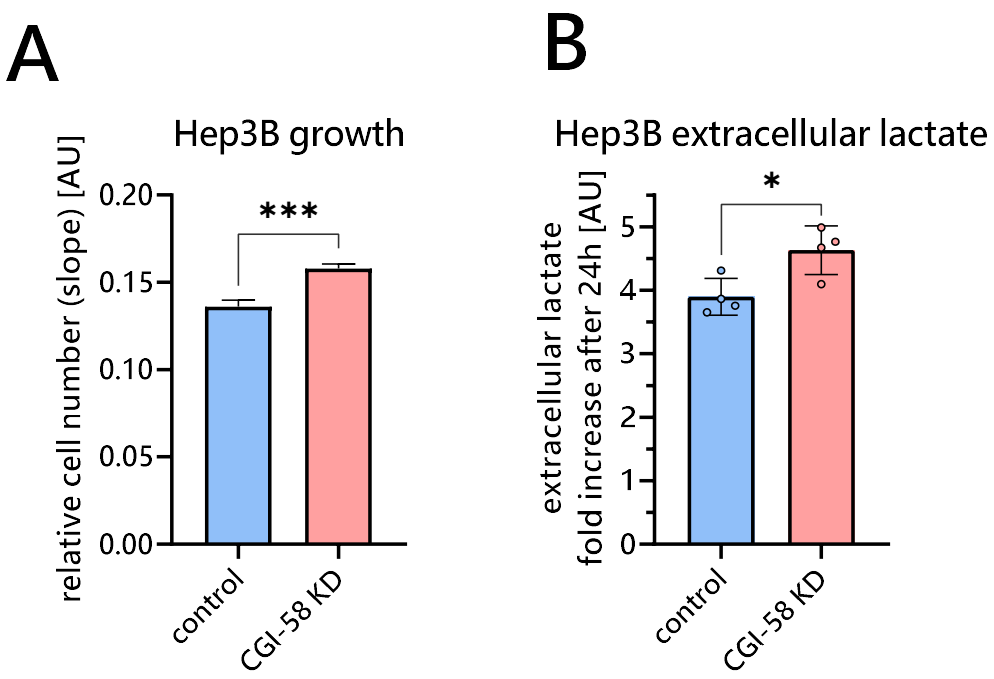

Figure 16: Differences in growth and lactate secretion in Hep3B CGI-58 vs. control cells. (A) Growth analysis (CCK-8) of Hep3B cells (24 h) shows increased growth of CGI-58 KD cells compared to controls. **(B)** Glo-lactate assay suggests slightly increased extracellular lactate in in Hep3B CGI-58 KD compared to controls. (* p-value < 0.05, *** p-value < 0.001).

4.2.2 CGI-58 over-expression in Hep3B cells does not influence the metabolic phenotype

Corresponding to the increase in LD volume in Hep3B CGI-58 KD cells vs. control, we detected a decrease in LD volume in Hep3B CGI-58 OE cells vs. GFP control (Figure 13). We therefore decided to additionally perform label-free quantitative proteomic analysis of Hep3B CGI-58 OE vs. GFP control. Data analysis was performed by pre-processing of our data (see Methods section 3.5) and filtering for 100 % (stringent filtering due to the high variance of the dataset) of valid values (4 samples per group, 8 samples total), reducing our dataset from 5834 to 2944 identified proteins. A two-sample student's t-test (two sided) with S_0 = 0.1 and permutation-based FDR of 0.05 with 250 randomizations did not result in any significantly (q-value < 0.05) differentially expressed proteins between Hep3B CGI-58 OE vs GFP OE. A volcano plot of this analysis is shown in Figure 17 A. Without FDR correction, 163 proteins were significantly (p-value < 0.05) differentially expressed between CGI-58 OE and GFP control. Principal component analysis revealed no separation between Hep3B CGI-58 OE and GFP OE cells (Figure 17 B). STRING analysis with all available proteins, annotated with $\log_2$-fold change, in "proteins with values/ranks" could not detect any enriched pathways regarding metabolism, growth or pathological signalling. These results suggest OE of CGI-58 increases the turnover of TG in LD but might not be involved in other cellular functions at an expression level higher than its base level, contrary to more pronounced effects by its depletion (CGI-58 KD).

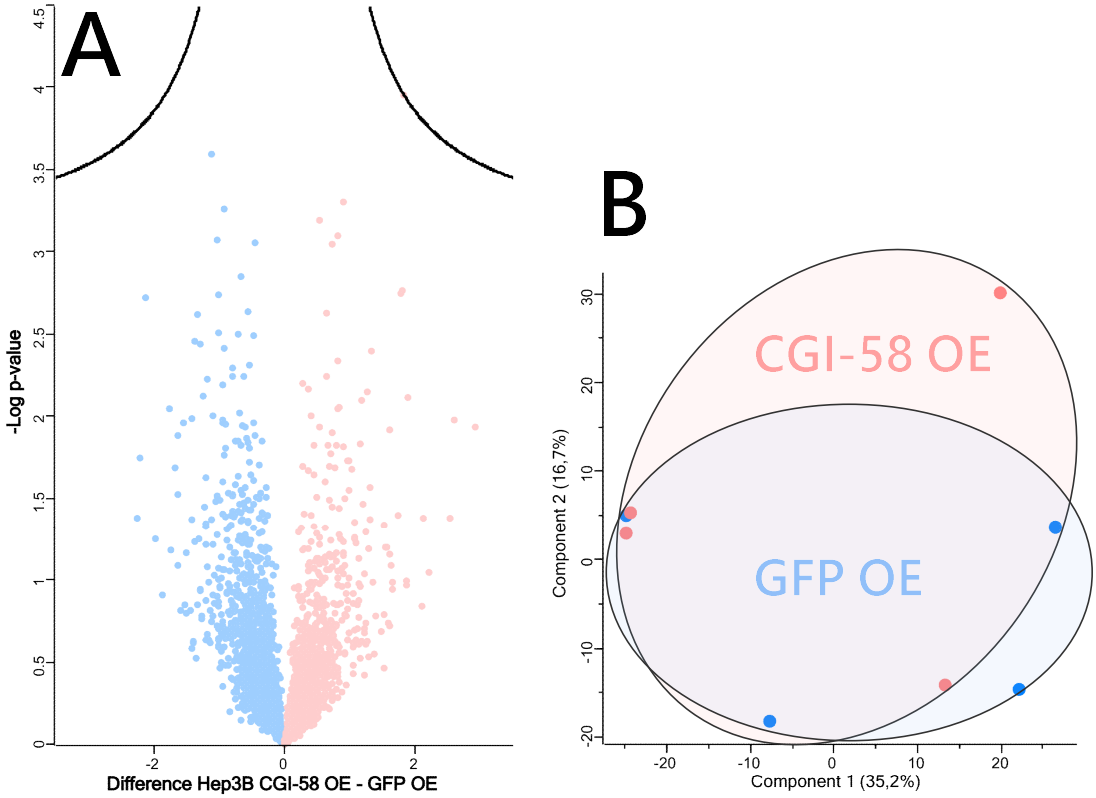

Figure 17: LFQ proteomics data shows no statistically significant (q-value < 0.05) differentially regulated proteins between Hep3B CGI-58 OE vs. GFP OE control. n = 4 samples per group. (A) Volcano blot of Hep3B CGI-58 OE cells vs. GFP OE control, LFQ data. Statistical analysis: t-test (two-sided) with multi-testing (permutation-based) corrected FDR = 0.05, S0 = 0.1 plotted as -Log10 p-value. Difference in protein expression plotted as log2 mean on x-axis. Red dots represent proteins with a difference of Hep3B CGI-58 OE vs. GFP OE control > 0, whereas blue dots show protein expression < 0. (B) Principal component analysis of Hep3B CGI-58 OE vs. GFP OE control without category enrichment shows no separation between the two groups.

4.3 PNPLA3 I148M expression changes hepatocyte metabolism

PNPLA3 I148M is a common mutation in humans, drastically increasing the likelihood of liver disease and liver cancer (90). PNPLA3 is a close homolog of ATGL (PNPLA2) suspected

to sequester CGI-58 from ATGL, thereby decreasing TG hydrolysis and leading to accumulation of fat in the liver (89). We therefore investigated the effects of PNPLA3 I148M on potential protein expression changes in Hep3B cells. Hep3B cells innately carry the non-pathologic I148I (wt) variant of the PNPLA3 protein (110). To investigate the effect of the PNPLA3 I148M mutation in Hep3B cells, we over-expressed both the PNPLA3 I148M mutant and wt of PNPLA3 in Hep3B cells using lentiviral transfection (Figure 6**Error! Reference source not found.** G, H). After geneticin[28] (G418) selection we performed western blotting analysis which revealed comparable ~10-fold OE of PNPLA3 I148M and wt relative to ancestral Hep3B cells (Figure 18 A, B).

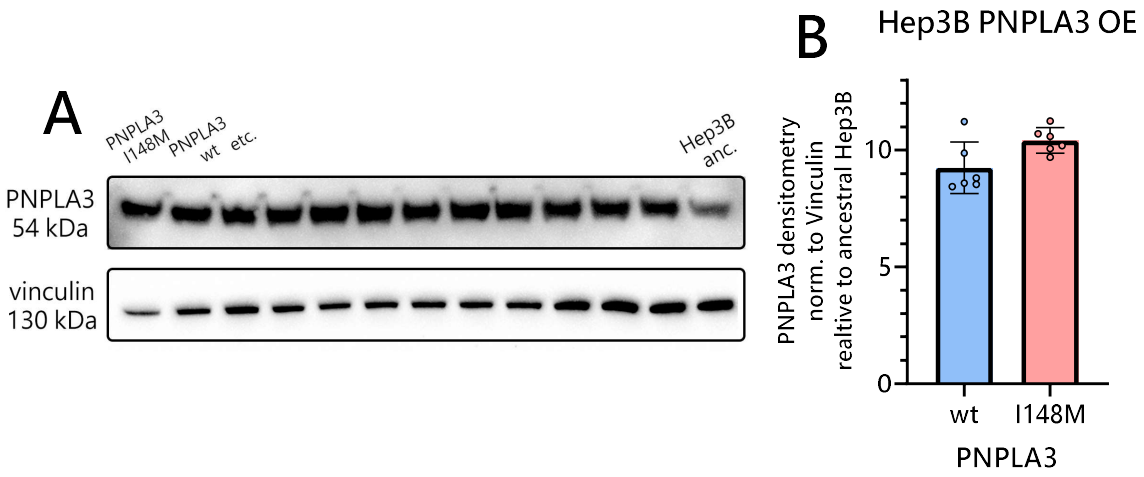

Figure 18: Western blot for PNPLA3 I148M or wt OE in Hep3B cells, compared to ancestral controls. 6 samples per group, 1 sample for ancestral cells. (A) Demonstration of western blot for PNPLA3 protein expression. (B) Graphical representation of Hep3B PNPLA3 expression (densitometry), normalized to Vinculin (loading control). Hep3B PNPLA3 wt and I148M cells show similar expression of PNPLA3 with a ~ 10-fold increase over ancestral Hep3B cells.

[28] Geneticin is, similar to hygromycin b, an antibiotic aminoglycoside which works by blocking the synthesis of polypeptides in eukaryotes (and procaryotes) during the elongation step (111).

Next, we performed label-free proteomic analysis of Hep3B PNPLA3 I148M vs. wt. After pre-processing our data (see Methods 3.5), we filtered for at least 10 valid values (PNPLA3 I148M vs. wt, 6 samples per group, 12 samples total), reducing our dataset from 5601 to 4378 quantified proteins. Missing values were imputed separately for each column with a width of 0.3 and a down-shift of 1.8. Next, a two-sample student's t-test (both sides) with $S_0 = 0.1$ and permutation-based false-discovery rate of 0.05 with 250 randomizations revealed no significant (q-value < 0.05) differentially expressed proteins between Hep3B PNPLA3 I148M vs. wt. A volcano plot of this analysis is shown in Figure 19 A. Without FDR correction, 193 proteins were significantly (p-value < 0.05) differentially expressed between Hep3B PNPLA3 I148M vs. wt. Principal component analysis revealed a clear overlap between Hep3B PNPLA3 I148M vs. wt cells (Figure 19 B).

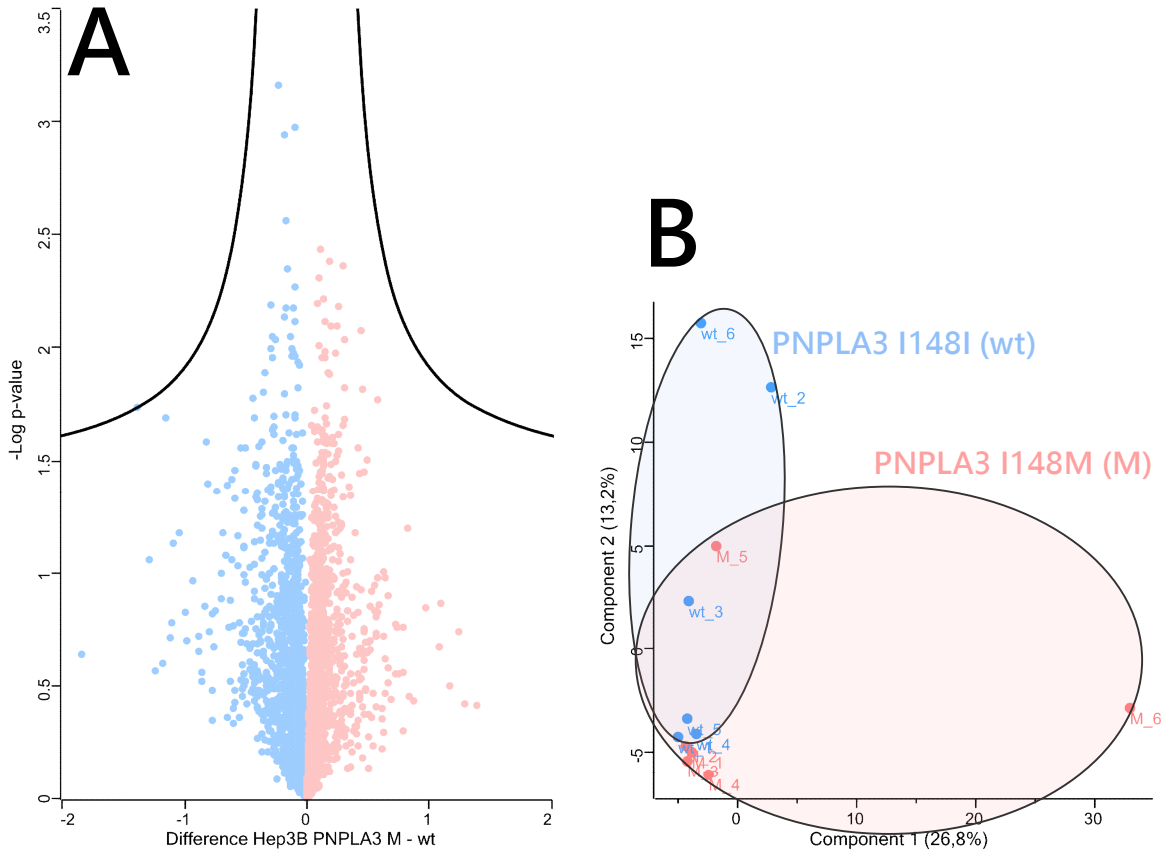

Figure 19: LFQ proteomics data shows no statistically significant (q-value < 0.05) differentially regulated proteins between Hep3B PNPLA3 I148M (M) vs. PNPLA3 wt control. n = 6

samples per group. **(A)** Volcano blot of Hep3B PNPLA3 I148M vs. wt control, LFQ data. Statistical analysis: t-test (two-sided) with multi-testing (permutation-based) corrected FDR = 0.05, S_0 = 0.1 plotted as -Log_{10} p-value. Difference in protein expression plotted as log_2 mean on x-axis. Red dots represent proteins with a difference of Hep3B PNPLA3 I148M vs. wt control > 0, where-as blue dots show protein expression < 0. **(B)** Principal component analysis of Hep3B PNPLA3 I148M vs. wt control without category enrichment shows a clear overlap between the two groups.

A closer investigation of the differentially expressed proteins in Hep3B PNPLA3 I148M vs. wt, using all available proteins, was achieved using the values/ranks section in STRING[29] database (99) with a high FDR < 0.01 and an initial sort order by enrichment on with the organism "homo sapiens". Interestingly, the peroxisome proliferator-activated receptor alpha (PPAR) pathway, a signalling pathway involved in the metabolism of fatty acids, was downregulated in Hep3B PNPLA3 I148M vs. wt control. Furthermore, Perseus 1D annotation enrichment analysis of identified proteins (sorted by differential expression, no cut-offs) with a lenient 0.25 Benjamini-Hochberg FDR cut-off revealed both a downregulation in the KEGG terms "fatty acid metabolism" and "TCA cycle and respiratory electron transport" in Hep3B PNPLA3 I148M vs. wt. This suggests a decreased catabolic process of fatty acids while upregulating glucose outside of mitochondria possibly via aerobic glycolysis. Although all of the above-mentioned pathways were downregulated, Spearman rank correlation calculation of the average of all 6 samples by group in Hep3B PNPLA3 I148M vs. wt was equal to 0.9965, suggesting no differences in normal distribution between groups (indicating a non-skewed dataset).

[29] The "proteins with values/ranks" section in STRING recommends the input of full datasets without cut-offs.

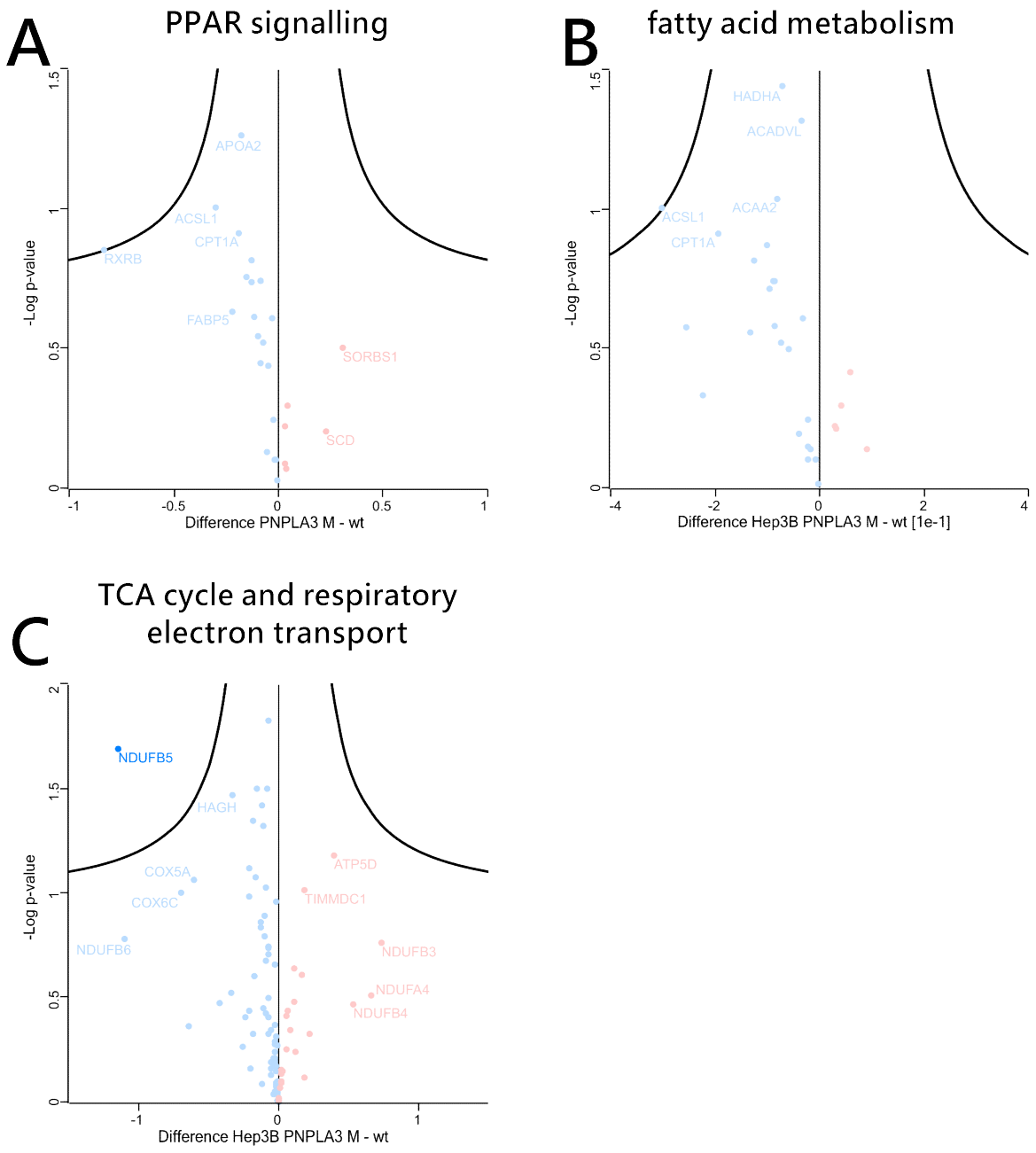

Figure 20: Volcano plots of enriched GO terms in Hep3B PNPLA3 I148M (M) OE vs PNPLA3 I148I (wt) OE LFQ data. n = 6 samples per group. Statistical analysis: t-test (two-sided) with multi-testing (permutation-based) corrected FDR = 0.05, S_0 = 0.1 plotted as -Log_{10} p-value with 250 randomizations. Difference in protein expression plotted as log_2 mean on x-axis. **(A)** Reactome "PPAR signalling pathway". 20 out of 26 (77 %) identified proteins were downregulated in Hep3B PNPLA3 I148M vs. wt. **(B)** GO process "fatty acid metabolism". 24 out of 29

(83 %) identified proteins were downregulated in Hep3B PNPLA3 I148M vs. wt. **(C)** Reactome "TCA cycle and respiratory electron transport". 74 out of 99 (74 %) identified proteins were downregulated in Hep3B PNPLA3 I148M vs. wt.

Table 4: List of enriched GO terms Hep3B PNPLA3 I148M vs PNPLA3 wt using all quantified proteins for analysis. Both KEGG pathways "PPAR signalling pathway" and "fatty acid metabolism" were identified using the 1D annotation enrichment in Perseus with a lenient Benjamini-Hochberg FDR cut-off of 0.25. The GO term "TCA cycle and respiratory electron transport" was identified using the STRING database (99) multiple proteins (values/ranks) input with a high FDR cut-off of 0.01.

TERM DESCRIPTION	CATEGORY	TERM ID	GENES MAPPED/ PATHWAY SIZE	FALSE DISCOVERY RATE
PPAR SIGNALING PATHWAY	KEGG	hsa03320	26/75	0.245
FATTY ACID METABOLISM	KEGG	ko01212	29/84	0.215
TCA CYCLE AND RESPIRATORY ELECTRON TRANSPORT	Reactome	HSA-1428517	99/176	0.007

5 Discussion

Primary liver cancer is usually caused by hepatocytes, being the most common liver cell by cell number and cell mass. Hepatocytes play a major role in metabolism in humans, being mainly responsible for lipid metabolism via the synthesis of new lipids and the uptake and distribution of circulating lipids. In NAFLD, deregulation of liver lipid metabolism is apparent in increased lipid synthesis, uptake of lipids, and/or reduced catabolism of stored lipids. The accumulation of neutral lipids is not toxic for hepatocytes *per se*, although drastically increased build-up of neutral lipids can lead to ballooning and apoptosis of hepatocytes (63). This can cause inflammation and recruitment of immune cells in the liver, as well as damage to nearby hepatocytes leading to liver damage (38). Additionally, de-toxification of FFA in neutral lipids can be reduced in NAFLD, often due to overwhelming influx of lipids, leading to additional inflammation in hepatocytes.

TG catabolism via ATGL and subsequent oxidation of FA in mitochondria can help reducing the amount of lipids present in hepatocytes. This is apparent in Figure 9 (B) where over-

expression of ATGL led to a reduction in LD volume in HepG2 cells, whereas OE of the enzymatically dead S47A mutant of ATGL led to an increase in LD volume (Figure 9 C) compared to controls (Figure 9 A). These findings are in line with ATGL KD and KO in mouse livers leading to accumulation of LD (64). An even stronger effect of ATGL mediated lipolysis can be seen in Figure 13 (B, E), where the decrease in CGI-58 expression (the activator of ATGL), drastically increased LD volume compared to control, whereas the OE of CGI-58 severely reduced LD volume, compared to GFP controls. Judged on the effect on LD volume, CGI-58 expression occupies a more important role in liver lipid metabolism than ATGL. This is further underlined by experiments on mice with CGI-58 loss and Chanarin-Dorfman syndrome (CGI-58 mutations) in humans showing drastic changes in liver health upon CGI-58 (function)-loss, but little effect by ATGL loss (see chapters 0 & 0).

5.1 Downregulation of CGI-58 leads to a more cancerous phenotype in Hep3B cells

Due to persistent inflammation, cell-, and DNA damage, NAFLD increases the risk of HCC in humans (19). Interestingly, in liver cancer, ATGL and CGI-58 are often downregulated, compared to healthy tissue (Figure 7 A2, Figure 11 A2). This might be due to the increase in *de novo* lipogenesis in many HCC cases (112), fuelling the enhanced demand for membrane lipids in rapidly dividing cells, which would be counteracted by over-active lipolysis. Furthermore, many cancer cells switch their metabolism towards a glycolytic pathway, which takes advantage of the ability to quickly generate energy from glucose. This could lead to a downregulation of lipolysis and subsequently β-oxidation through decreased expression of mitochondrial proteins, which are in less demand in a heavily glycolytic phenotype. Furthermore, lipids might be preferentially used generating new membrane lipids, rather than degradation or β-oxidation (112).

Some of this behaviour can be seen in Figure 15 (A, B) where both fatty acid degradation and proteins of the mitochondrial matrix are downregulated in Hep3B CGI-58 KD cells, compared to control. Additionally, PGM1 is downregulated in Hep3B CGI-58 KD cells vs. control, suggesting increased influx of glucose into the cell, since a decrease in hepatic PGM1 is associated with a downregulation in gluconeogenesis (113) and an induced upregulation of

glucose import[30] (109), as well as increased cancer malignancy (114). Furthermore, we could detect an increase in extracellular lactate in Hep3B CGI-58 KD cells, compared to control (Figure 16 B). Lactate is produced in greater extent and shuttled into the extracellular space in cells utilizing glycolysis, suggesting that, compared to controls, Hep3B CGI-58 KD cells preferentially metabolize glucose in the cytosol rather than shuttling pyruvate into mitochondria, fuelling the citric acid cycle and electron transport chain. In mitochondria, compared to controls. Strikingly, Hep3B CGI-58 KD cells show an increase in growth rate compared to control cells, further solidifying the hypothesis that a reduction of CGI-58 might lead to both a shift in metabolism and cancer aggressiveness.

Although we could identify features (glycolysis, growth) suggesting an increase in aggressiveness of Hep3B CGI-58 KD cells, compared to control, the protein PEG10 was found to be downregulated in Hep3B CGI-58 KD cells, which is used as a biomarker for HCC progression[31] (107), suggesting a more complicated picture of the effect of liver CGI-58 decrease.

5.2 Upregulation of CGI-58 is not associated with a metabolic shift in Hep3B cells

Although we could observe major changes in CGI-58 KD vs. control Hep3B cells in regard to lipid and glucose metabolism (and related proteins), as well as growth differences, over-expression of CGI-58 in Hep3B cells did not result in any significant changes to the proteome (Figure 17 A, B), compared to GFP OE control cells. This might appear counter-intuitive at first, expecting CGI-58 OE and KD would act in opposite ways. Instead, we hypothesize a sudden increase in CGI-58 expression first reduces LD volume drastically but might not have any longer-lasting effects other than keeping Hep3B LD volume small.

[30] It is important to note that Hep3B cells are grown in high-glucose media easing the transition to an aerobic glycolytic phenotype by providing a continuous supply of extracellular glucose.
[31] PEG10 plays a role in cell proliferation and apoptosis.

5.3 The PNPLA3 I148M mutation is associated with a shift towards a glucose-focused metabolism in Hep3B cells

The I148M mutation in PNPLA3 is often associated with a decrease in lipolytic activity, due to the sequestration of CGI-58 by PNPLA3 I148M (89). Therefore, we expected to see similar results in protein expression between Hep3B CGI-58 KD and Hep3B PNPLA3 I148M OE. Although PCA analysis of proteomics data shows significant overlap between Hep3B PNPLA3 I148M vs. wt (Figure 19 B) and no identified proteins were found to be significantly ($q < 0.05$) differentially regulated between these groups (Figure 19 A), we could identify enriched pathways related to lipid and glucose metabolism, however, with low statistical significance. First, PPAR signalling pathways are downregulated in Hep3B PNPLA3 I148M vs. wt (Figure 20 A), which indicates a shift in various lipid metabolism related pathways. PPAR-γ is regulating lipid biosynthesis (115), whereas PPAR-α regulates lipid breakdown (116). We could identify more proteins related to PPAR-α in our dataset, compared to PPAR-γ, suggesting downregulation of lipolysis in Hep3B PNPLA3 I148M vs. wt. Furthermore, fatty acid metabolism related proteins were mostly downregulated in Hep3B PNPLA3 I148M vs. wt (Figure 20 B). Additionally, we found a downregulation of the pathway "TCA cycle and respiratory electron transport" (Figure 20 C). This suggests a link between PNPLA3 I148M mutations and glucose metabolism/glycolysis (117). Although we did not yet perform LD volume analysis in Hep3B PNPLA3 I148M cells, other studies show increased LD volume upon PNPLA3 I148M expression, compared to PNPLA3 wt controls (118).

5.4 Conclusion

Taken together, these results suggest that both Hep3B CGI-58 KD and Hep3B PNPLA3 I148M OE share similarities regarding glucose and lipid metabolism. Both, the downregulation of CGI-58 and OE of PNPLA3 I148M seem to entail a re-wiring of Hep3B metabolism via the downregulation of lipolysis and catabolism of lipids in mitochondria, while an upregulation of glycolysis is occurring in Hep3B CGI-58 KD cells (Figure 16 B) and downregulation of the classical TCA cycle is seen in Hep3B PNPLA3 I148M OE cells (Figure 20 C). This change of central metabolic pathways may be linked to an increase in proliferation in Hep3B CGI-58 KD cells (Figure 16 A) compared to controls, suggesting increased cancer aggressiveness. Taken

together with the decrease of CGI-58 expression in tumours (Figure 11 A, B), these results might hint at a mild cancer-protective effect of CGI-58.

CHAPTER TWO: THE ROLE OF LIPID METABOLISM IN HEPATIC STELLATE CELL INDUCED LIVER FIBROSIS

6 Introduction to activation and lipid metabolism in hepatic stellate cells

Hepatic stellate cells (HSC) are mesenchymal cells surrounding sinusoidal blood vessels in the liver. These cells are also called Ito-cells or lipocytes (fat-storing cells) because they store ~80 % of the total systemic retinol (vitamin A) supply as retinol esters in lipid droplets in their quiescent (or resting) state (119). They are responsible for uptake and re-distribution of retinol in the body. Apart from retinol storage, their lipid droplets are made up of ~32 % triglycerides (52). Additional functions of quiescent hepatic stellate cells are yet elusive.

Upon liver damage or inflammation, their unique ability to quickly transform into a proliferative, fibrotic phenotype has sparked interest in their role in causing liver fibrosis. HSC are sensitive to external stimulation, for example by immune cells (38) or damaged hepatocytes (120).

Activated HSC alter their phenotype in order to enhance production of fibrotic proteins to isolate damaged areas of the liver (120). These fibrotic proteins like collagen or fibronectin also close off parts of the fenestrated blood vessels and reduce access to the blood flow, further isolating the site of damage from the rest of the liver (121).

Hepatic stellate cells can also reverse their activation and proceed to a reverted state, which removes some of the fibrotic tissue and supports resettlement of new hepatocytes (55).

Long lasting inflammation in the liver results in perpetual activation of HSC, depositing large amounts of fibrotic tissue leading to decreased liver function and fibrosis (122). It is therefore crucial to better understand the implications of HSC activation and the role these cells play in liver health. In the next sections, we explored and investigated an often-used method of HSC *in vitro* activation, which helped us better understand the transformations these cells undergo during their transition. To this end, we decided to take a closer look at proteomic and phenotypic changes in HSC during activation.

7 Material and Methods

Parts of this section have been published in Schinagl et al 2021 (1).

7.1 Cell Culture

LX-2 cells (EP-CL-0560, Szabo Scandic, Vienna, Austria), as well as Hep3B cells (a kind gift provided by the lab of Prof. Michael Trauner at the Medical University of Vienna, Austria) were cultured in high-glucose Dulbecco's Modified Eagle Medium (DMEM D6546, Sigma-Aldrich, St. Louis, Missouri, USA) supplemented with 2 mM L-glutamine (25030081, Gibco, Thermo Fisher, Waltham, USA) and either 1 or 10 % FBS (F7524, Gibco) in plastic dishes (all plastic dishes are surface treated 734-2323 VWR, Radnor, Pennsylvania, USA). For all LX-2 activation related assays we used 1% FBS DMEM, unless stated otherwise. Hep3B cells were always kept at 10 % FBS, unless stated otherwise. Cells were maintained at 37 °C at 5 % CO_2 and 20 % O_2. LX-2 and Hep3B cells were sub-cultured every 72 h at a ratio of 1:5 and used for experiments after at least two passages of subculturing. Cell lines were used to a maximum passage number of 10 after seeding. Seeding equal numbers of cells was assured using the CASY and EVE cell counting systems. LX-2 and Hep3B cells for western blot and proteomic analysis were harvested after 24 and 48 h, respectively.

7.2 Protein overexpression and knock-down

LX-2 PNPLA3 overexpression (OE), as well as Hep3B CGI-58 KD and control was achieved using custom designed lentiviral vectors by Vector Builder (Chicago, USA) (Figure 6) and cells were selected using either G418 or Hygromycin (both Thermo Fisher). Protein expression was confirmed via western blotting after at least 14 days of selection.

7.3 Proliferation Assay

LX-2 cells were seeded in 96-well plates at 10,000 cells per well in 1 % FBS containing DMEM growth medium. After 24 h, media was replaced by 100 µL of either 1 % or 10 % FBS containing DMEM. Cell proliferation was assessed every 24 h using the cell counting kit 8 assay (CCK 8, 96992, Sigma-Aldrich, St. Louis, MO, USA) according to protocol.

7.4 Western Blotting Analysis

LX-2 cells were harvested after 24 h incubation time at either 1 or 10 % FBS at ~85 % confluency using trypsin-EDTA (25200056, Thermo Fisher). LX-2 cells for PNPLA3 expression analysis were harvested after 48 h of incubation in 1 % FBS. Cells were lysed in CST lysis buffer (9803, Cell Signalling Technologies, Danvers, MA, USA) supplemented with protease inhibitor cocktail (P8340, Sigma Aldrich). SDS-page 4 to 12 %, Bis-Tris, 1.0 mm (WG1401A, NuPage, Thermo Fisher, Waltham, MA, USA) was used to resolve equal amounts of protein using 1X MES-SDS running buffer (AB349824, abcr, Karlsruhe, Germany) at 200 V constant for 45 min on ice. Semi-dry blotting was performed onto nitrocellulose membranes (IB23001, Invitrogen, Thermo Fisher) using the iBlot 2 (Thermo Fisher) at 7 V for 30 min. Blocking of membranes was achieved by protein-free (PBS) blocking buffer (37572, Thermo Fisher) for 1 h at RT. Primary antibody (α-SMA, Invitrogen 1A4; vinculin, Invitrogen 7F9; COL1A1 Invitrogen PA5-29569; PNPLA3, Thermo Fisher 16809965) incubation was performed over night at 4 °C and secondary HRP antibody (horse anti-mouse 7076, Cell Signalling Technologies, goat anti-rabbit 7074S Cell Signalling Technologies) incubation was performed at RT for 1 h. Chemiluminescent detection agent SuperSignal West Pico PLUS (34577, Thermo Fisher) was used as substrate and detection was done at a ChemiDoc MP or XRS+ (BioRad, Hercules, CA, USA). Image analysis was carried out with Image Lab (BioRad).

7.5 Proteomic Analysis

LX-2 cells were harvested using cell scrapers after 48 h incubation at either 1 % or 10 % FBS at ~85 % confluency. LX-2 cells for PNPLA3 OE analysis were cultured for 48 h in 1 % FBS. Cells were washed with PBS and lysed with an in-house reducing and alkylating buffer (100 mM TRIS HCl; pH = 8.5, 1 % sodium dodecyl sulphate, 10 mM tris(2-carboxyethyl) phosphine, 40 mM 2-chloroacetamide). After sonication (1 kJ), samples were heated to 95 °C for 10 min. 100 µg of protein per sample (after bicinchoninic acid assay protein estimation (BCA), Thermo Fisher Scientific, reducing agent compatible) were subjected to acetone precipitation by adding NaCl to a final concentration of 10 mM. After that, 4 x volumes of acetone were added and incubated for 10 min. After centrifugation (10 min at 14,000 g) the supernatant was removed. Dried samples were dissolved in 25 % TFE in 100 mM Tris-HCl (pH = 8.5) and

subjected to sonication until completely dissolved. For protein digest, samples were diluted to 10 % TFE using 100 mM ABC. Sequencing Grade Modified Trypsin (V5111, Promega, Walldorf, Germany) was added in a 1:100 enzyme to protein ratio and digest was done overnight at 37 °C. Samples were desalted the following day using in-house prepared polystyrene-divinylbenzene, reversed-phase sulfonate stage tips (66886, Supelco, Thermo Fisher) and re-suspended in 0.1 % formic acid. Chromatography was carried out on an Ultimate 3000 RCS Nano Dionex system (Thermo Fisher) equipped with an Aurora Series UHPLC C18 column (250 mm × 75 µm, 1.6 µm) (AUR2-25075C18A, Ionopticks, Fitzroy, Australia). Separation was achieved via a linear gradient of H_2O (solvent A) and acetonitrile, both with 0.1 % formic acid added (solvent B) (0 – 5.5 min 2 % B; 65.5 min 17 % B; 95.5 min 25 % B; 105 min 37 % B; 115.5 – 125.5 min 95 % B; 126 – 136.5 min 2 % B) with a flow rate of 0.4 µL/min. Column temperature was kept at 40 °C. Mass spectrometric analysis was performed on a timsTOF Pro (Bruker Daltonics, Billerica, Massachusetts, USA) in positive data dependent Parallel Accumulation-Serial Fragmentation (PASEF) (95) mode with enabled trapped Ion Mobility Spectrometry (TIMS) at 100 % duty cycle (100 ms cycle time). Source capillary voltage was set to 1500 V and dry gas flow to 3 L/min at 180 °C. The proteomics data for LX-2 activation via FBS and PNPLA3 I148M experiments were deposited to the ProteomeXchange consortium via the PRIDE (100) partner repository with the dataset identifier PXD029121 and PXD042879, respectively.

7.6 Proteomic Data Analysis

Data analysis, database search and protein quantification were performed with MaxQuant version 2.01.0 (96); and statistical data analysis with Perseus version 1.6.14.0 (97). Search criteria: false discovery rate (FDR) for peptide, peptide-to-spectrum as well as protein matches was set to 1 %. Peptide tolerance was set to ± 20 and ± 4.5 for the first and main peptide search, respectively. Product mass tolerance was set to ± 0.5 Da. Cysteine carbamidomethylation was set as static whereas methionine oxidation and N-terminal acetylation were set as dynamic modifications. Minimum required peptide length was six amino acids and maximum number of allowed tryptic mis-cleavages was two. For protein search, the SwissProt human FASTA file (downloaded on 30 November 2020 from https://www.uniprot.org, 20,434 entries) containing most common protein contaminants was used as a database. Label-free

protein quantitation (LFQ) was performed with a minimum of two peptides per protein (unique and razor) as quantitation requirement. Match between runs was enabled in the retention time window of 1 min and alignment window of 20 min respectively. This resulted in a list of 4598 proteins with their corresponding LFQ values. LFQ values were log2 transformed (resulting in invalid values [NaN] for any missing value), and contaminants were removed. Further data analysis and graphical interpretation of protein networks was performed using Cytoscape (98) v3.8.2. STRING (99) v11.5 was used to generate protein networks using the following parameters: Homo Sapiens, full STRING network, medium confidence (0.4), medium FDR stringency (0.05). Imputation histograms can be found in the appendix (Figure 30).

7.7 Migration Gap Closure Assay

LX-2 cells were seeded in silicone 2-well inserts (80209, ibidi, Gräfelfing, Germany) in 12-wells at 50.000 cells per silicone well in 100 µL 1 % FBS containing DMEM. 2 mL of 1 % or 10 % FBS containing DMEM were placed outside the silicone insert. After 24 h, silicone inserts were carefully removed, and cells were imaged in 4 positions on a cell observer (Zeiss, Jena, Germany) at 37 °C in 20 % O_2 and 5 % CO_2 for 24 h. Gap closure was assessed by an in-house script by Juergen Gindlhuber in NIS-Elements v5.20.02 (Nikon, Tokyo, Japan).

7.8 Migration Transwell Assay

LX-2 cells were seeded in 12-well transwell inserts (polycarbonate, 8 µm pore size, 140656, Thermo Fisher) and put into 12-wells containing either 1 % or 10 % FBS for 24 h. For microscopic analysis, inserts were removed from the 12-well plate, washed twice with PBS and formaldehyde fixed for 2 min at room temperature (RT). After that, cells were washed twice with PBS, permeabilized with methanol for 20 min at RT, stained with crystal violet for 15 min at RT and again washed twice with PBS. Finally, cells from the top layer of the transwell were carefully removed using a cotton swab. Before recording on an inverse microscope, transwells were placed onto a glass slide with the transwell membrane facing down.

7.9 Lipid Droplet Analysis

125.000 LX-2 cells were seeded onto glass cover slips (ROTH, 18 × 18 mm, thickness 0.13 – 0.16 mm) in 6-wells in 1 % FBS media and after they were allowed to settle for 2 h treated with 200 µM oleic acid bovine serum albumin (BSA) conjugate to initiate LD formation. After 24 h, the medium was replaced by either 1 % or 10 % FBS containing medium. After 48 h of additional incubation, LD were stained with BODIPY 493/503 (D3922, Invitrogen, Thermo Fisher) for 10 min at 37 °C and then washed twice with pre-warmed PBS. After that, cells were fixed with 3.7 % formaldehyde for 10 min at 37 °C and nuclei received DAPI staining (H-1200-10, Vector Labs, Newark, California, USA). Cover slips were placed onto glass slides (ROTH) and imaged on a Nikon A1 confocal microscope. LD volume was calculated using an in-house FIJI (101) script by Juergen Gindlhuber.

8 Results

8.1 Activation of hepatic stellate cells

HSC activation is a complex process involving different aspects of metabolism and changes in gene expression. The degree of HSC activation is frequently measured in the expression of proteins which resemble the active phenotype. Alpha smooth muscle actin (α-SMA) and collagen 1 A 1 (COL1A1) are two examples of proteins which are highly expressed in activated, compared to quiescent[32] HSC (123–126). To investigate this shift in protein expression, we induced artificial activation by treating LX-2 cells with either 10 % FBS or 1 % FBS for 24 h, as FBS treatment is a commonly used technique for HSC activation in both human and animal cell models (127–129). Western blotting analysis revealed a significant (two-sided t-test, $p < 0.05$) increase in both α-SMA (Figure 21 A) and COL1A1 (Figure 21 C) expression after 24 h in LX-2 10 % FBS vs. 1 % FBS.

To investigate the ability of HSC to revert back into a quiescent state, we decreased the concentration of LX-2 cells grown for 24 h in 10 % FBS to 1 % FBS for an additional 24 h. Strikingly, α-SMA expression was reduced ~6-fold in these LX-2 cells, compared to cells which were kept in 10 % FBS for 48 h total (Figure 21 B).

[32] Although this thesis is describing quiescent LX-2 cells at 1 % FBS, in vitro HSC are never fully quiescent. Even freshly isolated HSC begin activation when in contact with plastic dishes. Therefore, when quiescent HSC are mentioned in the following section, partially quiescent cells are described.

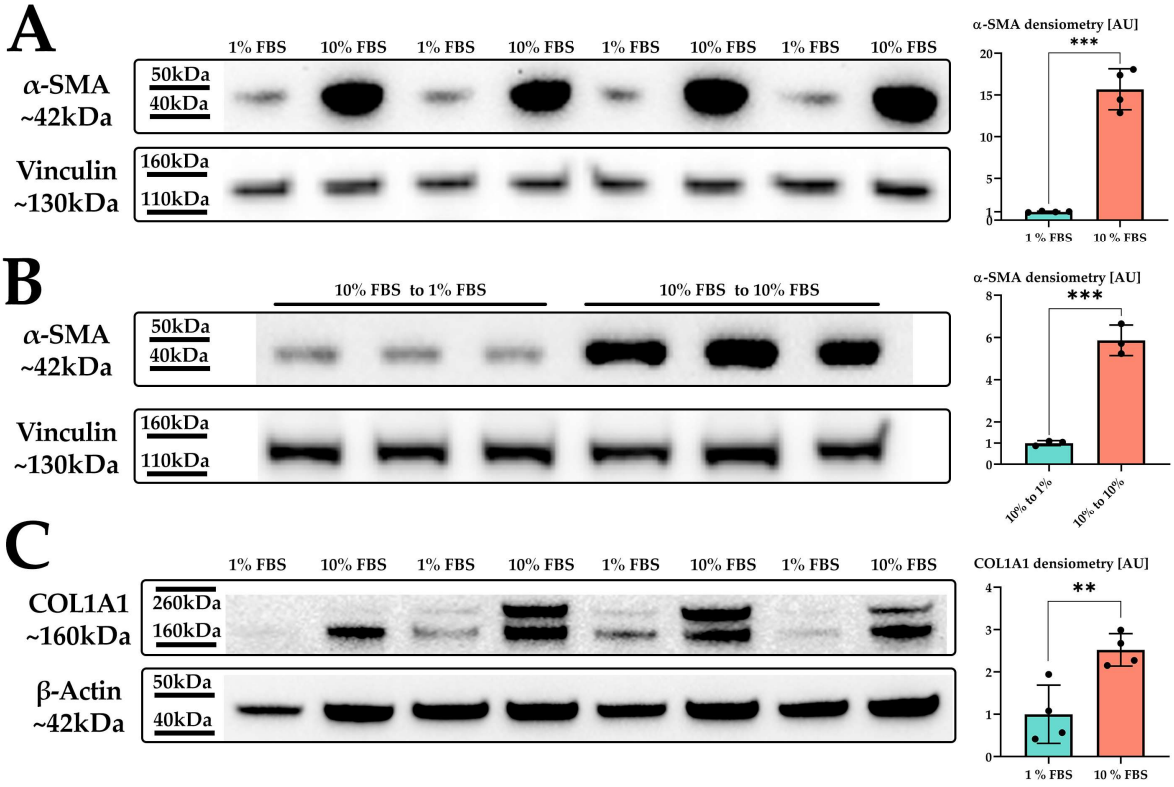

Figure 21: Western blot for α-SMA and COL1A1 in LX-2 cells treated with 10 % or 1 % FBS. **(A)** Higher concentrations of FBS resulted in an increase in α-SMA expression, 10 % FBS compared to 1 % for 24 h. 6 samples per group. **(B)** Reversion of LX-2 cells by a decrease in FBS concentration (from 10 % FBS to 1 % FBS, 24 h) resulted in the decrease of α-SMA expression. 3 samples per group. **(C)** Higher concentrations of FBS resulted in an increase in COL1A1 expression, 10 % FBS compared to 1 % for 24 h. 4 samples per group. Two-sample (two-sided) t-test, $p < 0.05$. Adapted from Schinagl *et al* 2021 (1) under CC BY 4.0 license.

Next, we explored additional changes to the proteome of HSC which undergo activation with label-free quantification proteomic analysis of LX-2 treated with either 1 % or 10 % FBS for 48 h. After pre-processing of our data (see Methods 7.6), filtering for 100 % of valid values in at least one group (6 samples per group, 12 samples total), we reduced our dataset from 4428 to 3163 identified proteins. Missing values were imputed separately for each column using a width of 0.3 and a downshift of 1.8. Two sample student's T-test (both sides) with $S_0 = 0.1$ and permutation-based false-discovery rate of 0.05 with 250 randomizations resulted

in 465 significantly (q-value < 0.05) differentially expressed proteins between LX-2 1 % vs. 10 % FBS. A volcano plot of this analysis with equivalent parameters is shown in Figure 22 A. Without FDR correction, 1033 proteins were significantly (t-test (both sides), p-value < 0.05, S_0 = 0.1) differentially expressed between LX-2 1 % and 10 % FBS. Principal component analysis revealed a clear separation between LX-2 1 % and 10 % FBS cells (Figure 22 B).

Due to the large number of highly significant (q < 0.05) differentially expressed proteins between LX-2 1 % and 10 % FBS, we performed gene ontology enrichment analysis on these 465 highly significant proteins. For this we used the Fisher exact test in Perseus with Benjamini-Hochberg FDR correction with a threshold value of 0.02. First, we identified upregulation of the KEGG term “Ribosome” and downregulation of the KEGG term “Lipid metabolism” in LX-2 10 % FBS vs. 1 % FBS (Table 3). Additionally, we performed gene ontology analysis using STRING database (99) with all available proteins (3163 proteins) in “Proteins with Values/Ranks”.

Strikingly, both ribosomal proteins and proteins related to lipid metabolism were highly up- and downregulated, respectively (LX-2 10 % FBS vs. 1 % FBS). In Figure 22 A, red dots indicate proteins which are included in the terms of “ribosomes” and “ribosome biogenesis in eukaryotes” (both KEGG) and the GOBP terms “ribosome assembly” and “ribosome biogenesis”. Blue dots in Figure 22 A indicate proteins related to the GOBP terms “fatty acid beta-oxidation”, “fatty acid metabolic process” and “lipid metabolic process”. Out of the highly significant proteins in this graph (q < 0.05), “lipid metabolism” showed 35 out of 43 proteins were downregulated, whereas “ribosome” showed 29 out of 30 proteins were upregulated. This suggests a downregulation of processes involved in lipid metabolism in activated LX-2 cells, whereas protein production via ribosomes is upregulated.

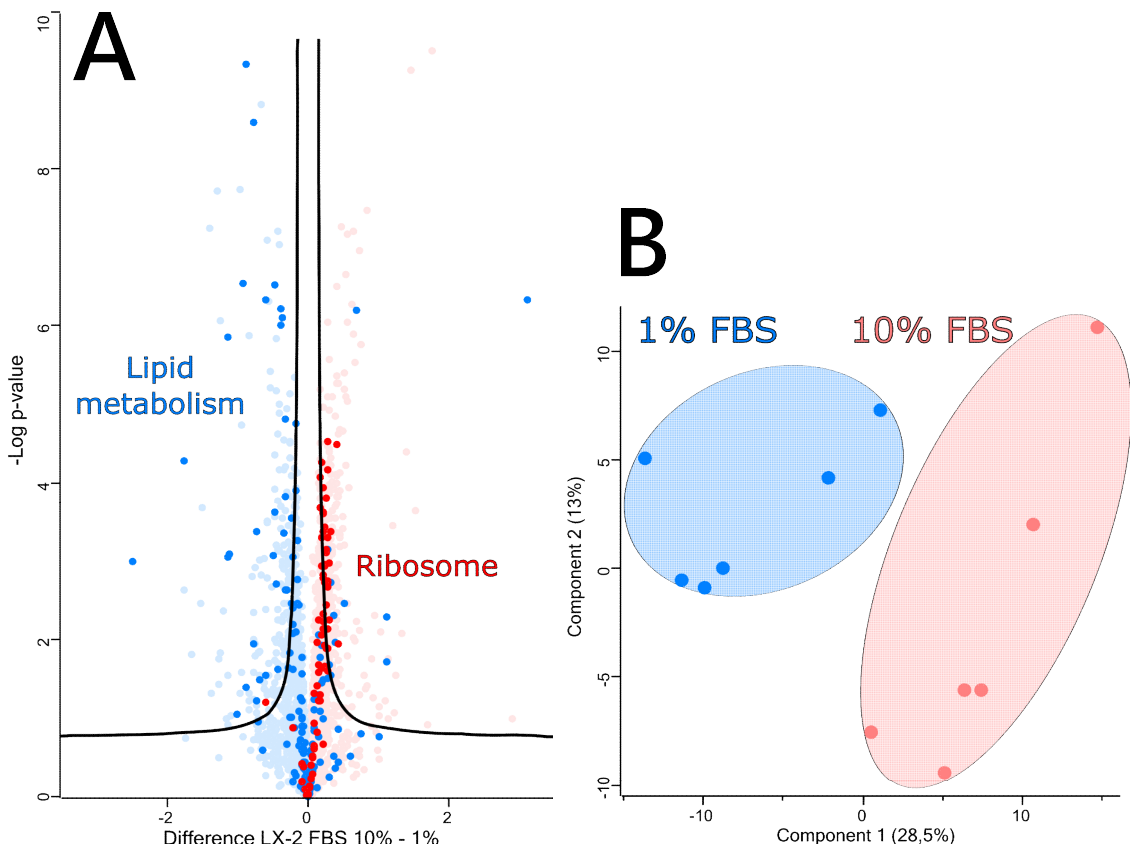

Figure 22: LFQ proteomics data shows statistically significant (q-value < 0.05) differentially regulated proteins between LX-2 10 % FBS vs. 1 % FBS control. n = 6 samples per group. **(A)** Volcano blot of LX-2 10 % FBS vs. 1 % FBS control, LFQ data. Statistical analysis: t-test (two-sided) with multi-testing (permutation-based) corrected, FDR = 0.05, S_0 = 0.1 plotted as -Log_{10} p-value. Difference in protein expression plotted as log_2 mean on x-axis. Pale red dots represent proteins with a difference of LX-2 10 % FBS vs. 1 % FBS control > 0, whereas pale blue dots show protein expression < 0. Bright red dots indicate proteins involved in multiple ribosomal biogenesis related pathways where 68 out of 75 identified proteins (29 out of 30 with q < 0.05) are upregulated in LX-2 10 % FBS vs. 1 % FBS control. Bright blue dots show proteins involved in multiple lipid metabolism related pathways where 99 out of 156 (35 out of 43 with q < 0.05) identified proteins are downregulated in LX-2 10 % FBS vs. 1 % FBS control. **(B)** Principal component analysis of LX-2 10 % FBS vs. 1 % FBS control without category enrichment shows a clear separation between the two groups.

To further investigate consequences of the downregulation of “lipid metabolism”, we took a closer look at other pathways involved in lipid metabolism. STRING analysis (see above) further identified the “fatty acid biosynthetic” pathway to be downregulated (Figure 23 A), while proteins involved in “citrate cycle TCA” were mostly upregulated (Figure 23 B) (Table 3).

Further analysis of proteins changed between LX-2 10 % FBS vs. 1 % FBS revealed changes in migratory behaviour (Figure 23 C), proliferation (Figure 23 D), extracellular matrix, and stress response (Figure 23 E). Proteins related to migration like fibronectin 1 (FN1) or angio-associated migratory cell protein (AAMP) were among the upregulated proteins in activated LX-2 cells, suggesting enhanced migration once activated. Many proteins related to proliferation, e.g., cyclin-dependent kinase 6 (CDK6) were upregulated as well. Additional proteins for extracellular matrix, like fibulin-2 (FBLN2), pleckstrin homology domain-containing family A member 2 (PLEKHA2) are upregulated likewise. Amino acid and nucleotide associated proteins, as well as stress response proteins (glutathione peroxidase 1 & 4 GPX1, GPX4) are upregulated in activated LX-2 cells. (Figure 23 E)

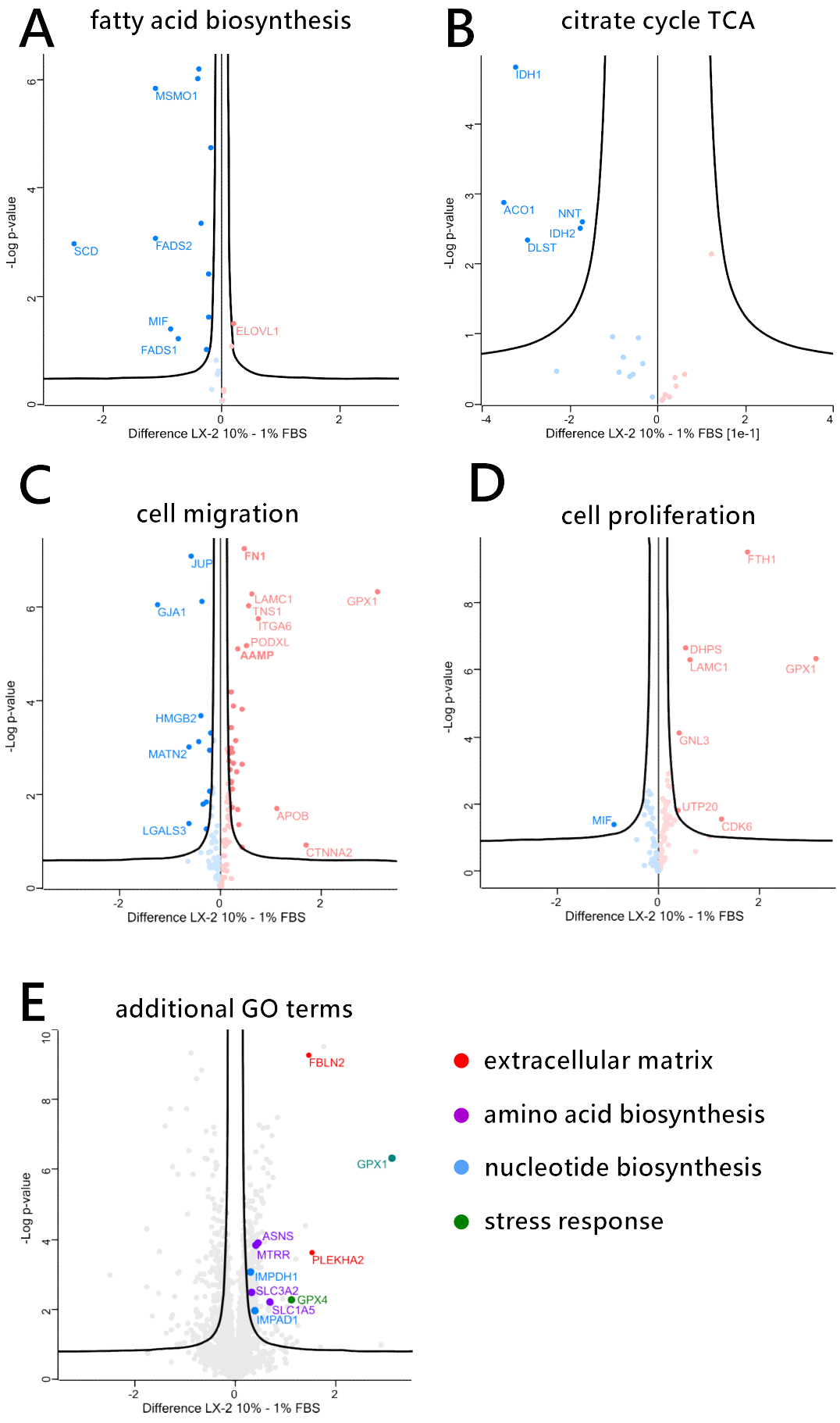
A
fatty acid biosynthesis
MSMO1
SCD
FADS2
MIF
FADS1
ELOVL1
-Log p-value
Difference LX-2 10% - 1% FBS
B
citrate cycle TCA
IDH1
ACO1
NNT
IDH2
DLST
-Log p-value
Difference LX-2 10% - 1% FBS [1e-1]
C
cell migration
JUP
FN1
GJA1
LAMC1
TNS1
ITGA6
GPX1
PODXL
AAMP
HMGB2
MATN2
APOB
LGALS3
CTNNA2
-Log p-value
Difference LX-2 10% - 1% FBS
D
cell proliferation
FTH1
DHPS
LAMC1
GPX1
GNL3
UTP20
MIF
CDK6
-Log p-value
Difference LX-2 10% - 1% FBS
E
additional GO terms
FBLN2
GPX1
ASNS
MTRR
PLEKHA2
IMPDH1
SLC3A2
GPX4
SLC1A5
IMPAD1
-Log p-value
Difference LX-2 10% - 1% FBS
extracellular matrix
amino acid biosynthesis
nucleotide biosynthesis
stress response

Figure 23: Volcano plots of enriched GO terms in LX-2 10 % FBS vs. 1 % FBS control LFQ data. n = 6 samples per group. Statistical analysis: t-test (two-sided) with multi-testing (permutation-based) corrected FDR = 0.05, S_0 = 0.1 plotted as -Log_{10} p-value with 250 randomizations. Difference in protein expression plotted as log_2 mean on x-axis. Pale dots show proteins with a q-value > 0.05, whereas bright dots show proteins with a q-value < 0.05 (red = upregulated, blue = downregulated in LX-2 10 % FBS vs. 1 % FBS controls). **(A)** GOBP "fatty acid biosynthesis" where 12 out of 13 identified proteins with a q-value < 0.05 are downregulated, 18 out of 26 proteins in total are downregulated in LX-2 10 % FBS vs. 1 % FBS control. **(B)** KEGG "citrate cycle TCA" where 5 out of 5 identified proteins with a q-value < 0.05 are downregulated, 15 out of 23 proteins in total are downregulated in LX-2 10 % FBS vs. 1 % FBS control. **(C)** GOBP "cell migration" where 32 out of 42 identified proteins with a q-value < 0.05 are upregulated, 75 out of 136 total identified proteins are upregulated in LX-2 10 % FBS vs. 1 % FBS control **(D)** GOBP "cell proliferation" where 7 out of 8 identified proteins with a q-value < 0.05 are upregulated, 66 out of 115 proteins in total are upregulated in LX-2 10 % FBS vs. 1 % FBS control. **(E)** Additional selected proteins of central pathways are highlighted in their respective colour. Volcano plot drawn with all identified proteins included.

Table 3: List of enriched GO terms LX-2 10 % FBS vs. 1 % FBS control. The GO terms "ribosome" and "lipid metabolism" were identified using the STRING database (99) multiple proteins (values/ranks) input using all identified proteins (n = 3163). In contrast to the volcano blot in Figure 22 A, this analysis only uses the KEGG term "ribosome" or the UniProt Keyword "lipid metabolism" without additional GO terms to avoid protein overlap.

TERM DESCRIPTION	CATEGORY	TERM ID	DIRECTION	GENES MAPPED/ PATHWAY SIZE	FALSE DISCOVERY RATE
RIBOSOME	KEGG	hsa03010	upregulated	88/130	4.54e-07
LIPID METABOLISM	UniProt Keywords	KW-0443	downregulated	92/482	2.87e-06
CITRATE CYCLE (TCA)	KEGG	hsa00020	downregulated	23/29	0.1176
FATTY ACID BIOSYNTHETIC PROCESS	GOBP	GO:0006633	Downregulated	26/118	0.0363
CELL MIGRATION	GOBP	GO:0016477	upregulated	62/136	0.0488
CELL PROLIFERATION	GOBP	GO:0008283	upregulated	48/115	0.157

Since we were able to identify changes to proteins in activated LX-2 cells related to proliferation, migration, and lipid metabolism, we further investigated these cellular

phenotypes. During activation in 10 % FBS, HSC transform into a proliferating, migratory phenotype. We therefore first assessed the proliferation of LX-2 cells treated with either 1 % or 10 % FBS. Higher FBS concentrations correlated with a significant increase (student's t-test, $p < 0.05$) in proliferation after 48 h (Figure 24 A). Next, we analysed LX-2 migratory behaviour under increased FBS concentrations. Similar to the upregulated proteins for cell migration (Figure 23 B), increased serum concentration also significantly increased (student's t-test, $p < 0.05$) the migratory potential of LX-2 cells after only 14 h (Figure 24 B). Despite showing increased proliferation, LX-2 do not show a difference in growth until 48 h (Figure 24 A), suggesting augmented migration without the effect of increased proliferation. Additionally, we tested transwell migration of LX-2 cells, where cells migrate through a porous (8 µm) membrane where they are fixed and stained after 24 h of incubation. Correspondingly, LX-2 cells migrated faster in higher FBS concentrations (Figure 24 C). Lastly, corresponding to a decreased expression of proteins involved in lipid metabolism (Figure 22 A), higher FBS concentrations significantly (student's t-test, two-sided, $p < 0.05$) decreased LX-2 LD volume after 48 h (Figure 24 D).

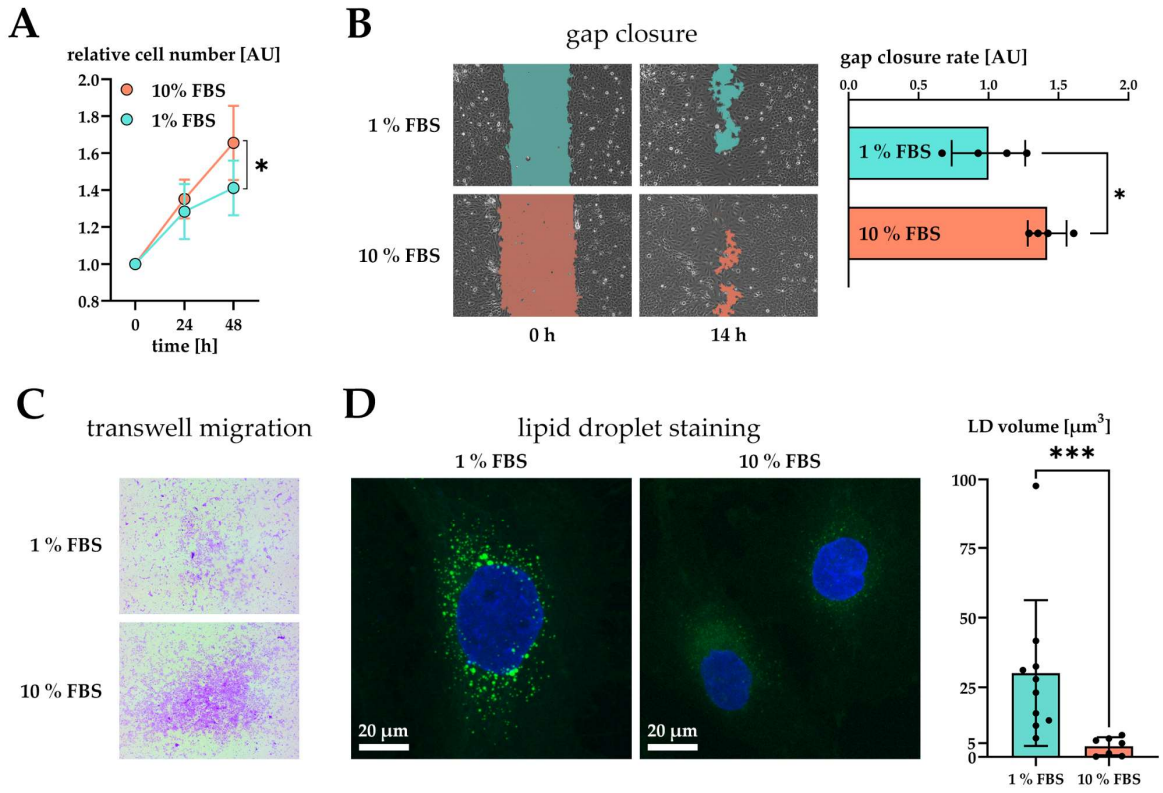

Figure 24: Phenotype analysis of LX-2 10 % FBS vs. 1 % FBS reveals differences in growth, migration, and lipid droplet volume. n = 4 samples per group. **(A)** LX-2 cells show increased growth (CCK-8 assay) in 10 % FBS, compared to 1 % FBS control after 48 h. **(B)** LX-2 cells display increased migration laterally (gap closure rate defined as the decrease in unoccupied area over time) and **(C)** through porous membranes (migrated cells indicated by purple staining) in 10 % FBS, compared to 1 % FBS. **(D)** Left: lipid droplets of LX-2 cells are stained with BODIPY (green), nuclei stained with DAPI (blue). LX-2 cells supplemented with 10 % FBS show decreased LD volume compared to LX-2 cells in 1 % FBS after 48 h of incubation. (* p-value < 0.05, *** p-value < 0.001). Adapted from Schinagl *et al* 2021 (1) under CC BY 4.0 license.

8.2 The PNPLA3 I148M mutation in hepatic stellate cells

As described in the previous chapter, lipid metabolism plays a central role in HSC activation and liver fibrosis. We therefore investigated a prominent mutation of PNPLA3[33], which is believed to be involved in the attenuation of triglyceride metabolism by sequestering CGI-58 from ATGL (89). Thus, we investigated how PNPLA3, both I148M and wt, changes HSC behaviour. To this end, we over-expressed I148M and wt PNPLA3 in LX-2 cells using lentiviral transfection (Figure 6 G, H). First, we identified sufficient OE relative to ancestral LX-2 cells using western blotting. Figure 25 B shows comparable OE of PNPLA3 I148M and wt in LX-2 cells with a 3-fold increase over ancestral LX-2 cells.

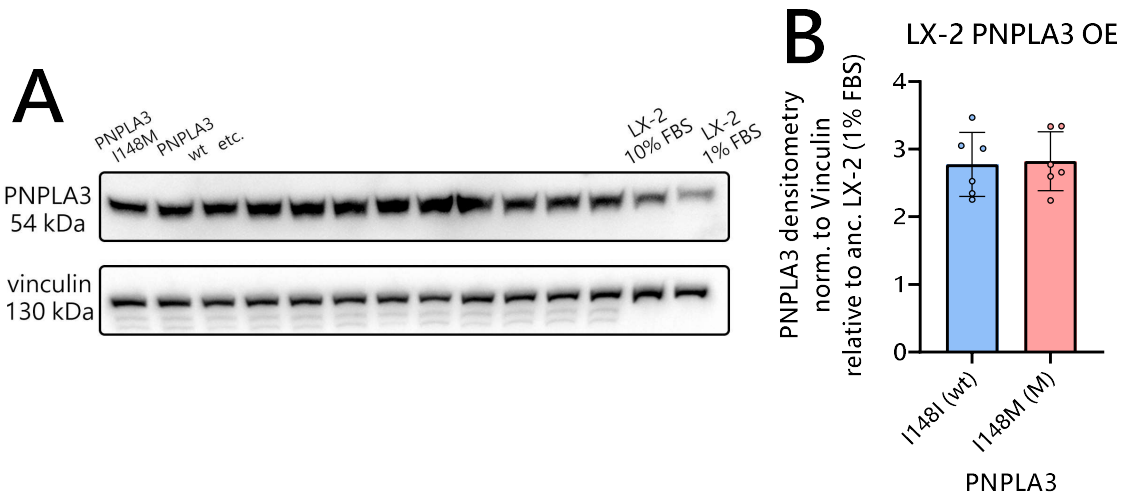

Figure 25: Western blot for PNPLA3 I148M or wt OE in LX-2 cells, compared to ancestral LX-2 cells. 6 samples per group, 1 sample for ancestral cells. **(A)** Demonstration of western blot PNPLA3 protein expression. **(B)** Graphical representation of Hep3B PNPLA3 expression (densitometry), normalized to Vinculin. LX-2 PNPLA3 I148M and wt cells show similar expression of PNPLA3 with a ~ 3-fold increase over ancestral LX-2 cells (1 % FBS).

[33] LX-2 cells innately carry the pathogenic PNPLA3 I148M (M) variant.

Next, we investigated proteomic changes in LX-2 PNPLA3 I148M and wt OE cells using label-free proteomics of LX-2 cells grown for 24 h (either PNPLA3 I148M or wt). After pre-processing our data (see Methods section 7.6), we normalized our data by calculating the mean transformed (log2) LFQ values for every column and subtracting the dedicated mean at every column to remove skewing in our dataset. Next, we filtered our dataset for at least 9 valid values out of 12 total (no grouping) and imputed missing values separately for each column with a width of 0.3 and a downshift of 1.8. Valid value filtering reduced our dataset from 5492 to 4256 identified proteins.

A two-sample student's T-test (two-sided) with $S_0 = 0.1$ and permutation-based FDR of 0.05 with 250 randomizations resulted in 1 significantly (q-value < 0.05) differentially expressed protein between LX-2 PNPLA3 I148M vs. wt control. A volcano plot of this analysis with equivalent parameters is shown in Figure 26 A. Without FDR correction, 598 proteins were significantly (p-value < 0.05) differentially expressed between LX-2 PNPLA3 I148M vs. wt control (see Table 5 in the appendix). Principal component analysis revealed a partial overlap between LX-2 PNPLA3 I148M vs. wt control (Figure 26 B).

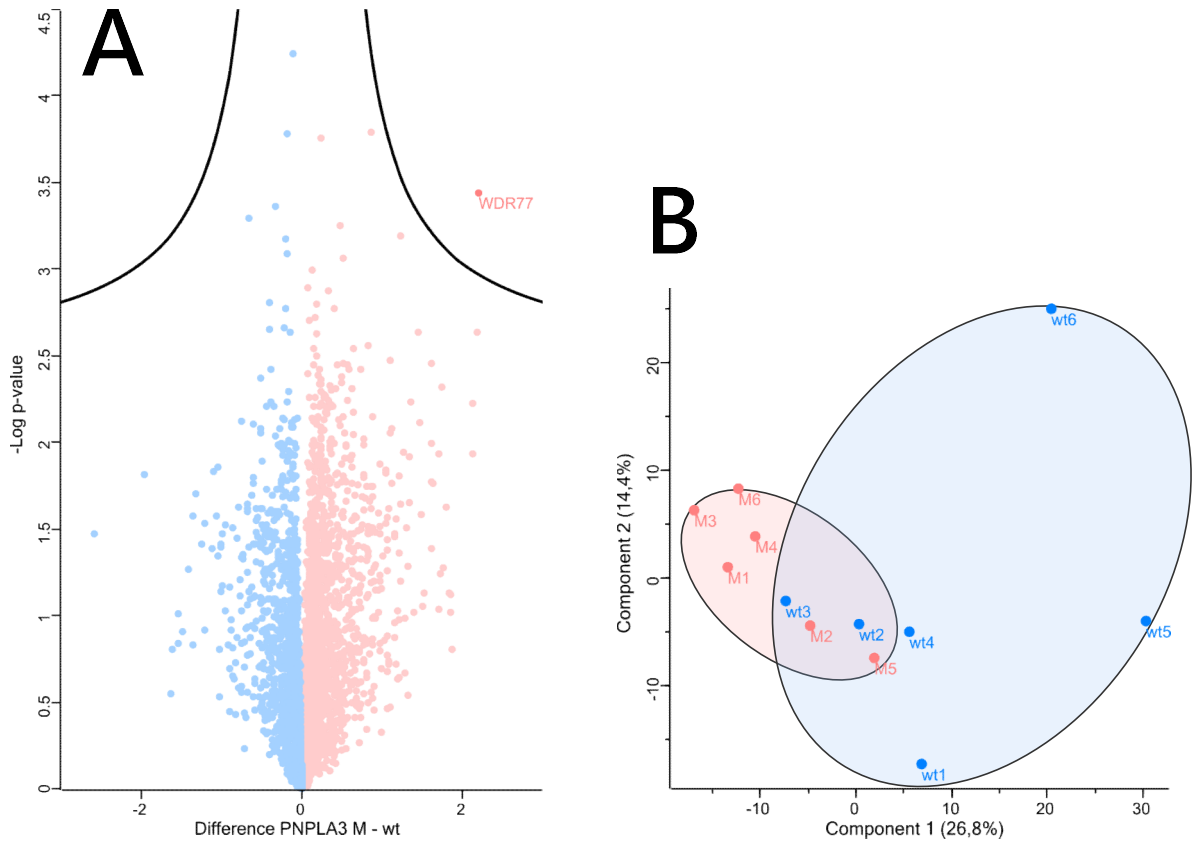

Figure 26: LFQ proteomics data shows one statistically significant (q-value < 0.05) differentially regulated protein between LX-2 PNPLA3 I148M (M) OE vs. PNPLA3 I148I (wt) OE control. n = 6 samples per group. (A) Volcano blot of LX-2 PNPLA3 I148M vs. wt control, LFQ data. Statistical analysis: t-test (two-sided) with multi-testing (permutation-based) corrected, FDR = 0.05, S_0 = 0.1, 250 randomizations, plotted as -Log_{10} p-value. Difference in protein expression plotted as log_2 mean on x-axis. Red dots represent proteins with a difference of LX-2 PNPLA3 I148M vs. wt control protein expression > 0, where-as blue dots show protein expression < 0. Only Methylosome protein 50 (WDR77) shows a statistically significant (q < 0.05) upregulation in LX-2 PNPLA3 I148M vs. wt control protein expression. **(B)** Principal component analysis of LX-2 PNPLA3 I148M vs. wt control without category enrichment shows overlap between the two groups.

The expression of methylosome protein 50 (WDR77) was increased in LX-2 PNPLA3 I148M vs. wt (q-value = 0.032, Figure 26 A). This protein is part of the methylosome complex, suggesting an increase in post-translational modifications in proteins. Further analysis of differentially expressed proteins between LX-2 PNPLA3 I148M vs. wt was done using the Fisher-exact test in Perseus with p-value significant (two-sided t-test, S_0 = 0.1, without multi-testing correction) proteins. Truncation of results was achieved with Benjamini-Hochberg FDR correction of < 0.2. Out of 598 proteins used for Fisher-exact analysis, we could identify enrichment in the Reactome pathway "p38 mitogen-activated protein kinases (p38MAPK) events", where 6 out of 6 proteins involved were be upregulated in LX-2 PNPLA3 I148M vs. wt control. Isolated analysis of these 6 proteins (two-sided t-test, S_0 = 0.1, permutation-based FDR = 0.05, Figure 27) revealed statistically significant (q < 0.05) upregulation of 5 out of 6 proteins involved in the pathway "p38MAPK events" (LX-2 PNPLA3 I148M vs. wt control). Strikingly, two well-studied oncogenes present in the "p38MAPK" pathway, KRAS and SRC are upregulated 32 % and 54 %, respectively, in LX-2 PNPLA3 I148M vs. wt.

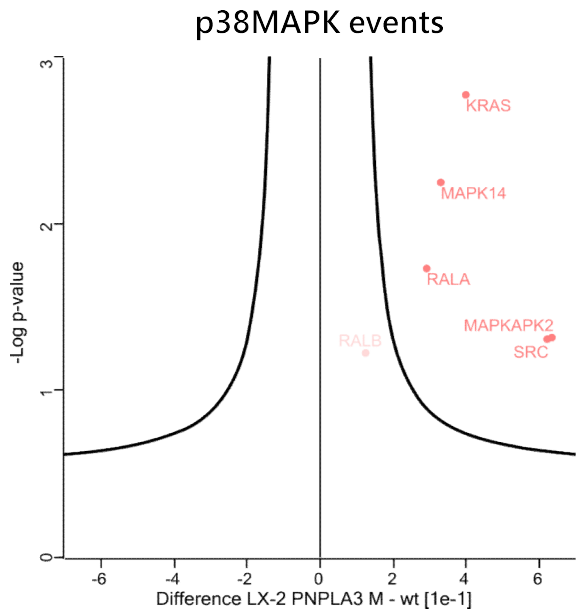

Figure 27: Volcano plots of the enriched GO term "p38MAPK events" in LX-2 PNPLA3 I148M (M) OE vs. PNPLA3 I148I (wt) OE control LFQ data. n = 6 samples per group. Statistical analysis: t-test (two-sided) with multi-testing (permutation-based) corrected FDR = 0.05, S0 = 0.1 plotted as -Log_{10} p-value with 250 randomizations. Difference in protein expression plotted as

log_2 mean on x-axis. Pale red dots show upregulated proteins with a q-value > 0.05 in LX-2 PNPLA3 I148M vs. wt control. Reactome "p38MAPK events" 5 out of 6 identified proteins with a q-value < 0.05 were upregulated, 6 out of 6 total identified proteins were upregulated in LX-2 PNPLA3 I148M vs. wt control. Reactome "p38MAPK events" pathway size = 6 proteins.

8.3 Hepatocyte- hepatic stellate cells co-culture

Lastly, we investigated the influence of CGI-58 in Hep3B hepatocytes in the context of hepatocyte – HSC interaction. To this end, we collected pre-conditioned media of either Hep3B CGI-58 KD or control cells after 24 h of incubation in 1 % FBS media. After filtering to remove cell debris, pre-conditioned media was mixed 1:1 with fresh 1 % FBS DMEM and applied to LX-2 cells for 24 h. Afterwards, LX-2 cells were harvested for WB. Although we could detect a small (non-significant) decrease in the expression of α-SMA in LX-2 cells treated with Hep3B CGI-58 KD pre-conditioned media, statistical analysis (two-sided t-test, $p < 0.05$) could not determine a significant change of α-SMA expression between LX-cells treated with either Hep3B CGI-58 KD or control pre-conditioned media.

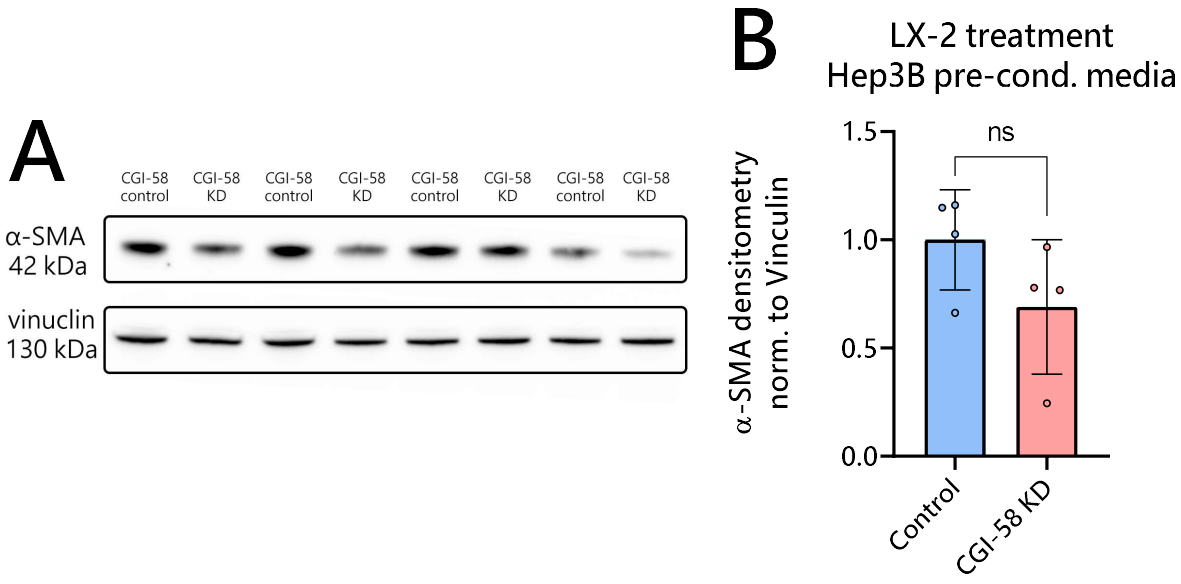

Figure 28: Western blot for LX-2 cells treated with pre-conditioned media of Hep3B cells with either CGI-58 KD or control. 4 samples per group. **(A)** Demonstration of western blot α-

SMA protein expression. **(B)** Graphical representation of LX-2 α-SMA expression (densitometry), normalized to Vinculin. LX-2 cells showed no significant difference (two-sided t-test, $p < 0.05$) between treatment with Hep3B CGI-58 KD or control pre-conditioned media for 24 h.

9 Discussion

The activation of HSC is a complex process, both from the perspective of the metabolism and gene expression. Activated HSC are a key player in liver fibrotic protein deposition and are therefore key in understanding progression of liver fibrosis. Although it is difficult to culture primary human HSC, both mouse- and human HSC cell lines have been established as a valuable resource in liver fibrosis research. LX-2 cells are a human HSC line enabling functional research by altering gene expression and rapidly testing activation conditions. Although the LX-2 cell line is immortalized using SV-40 (130), cell characteristics are somewhat comparable to primary human HSC (130). In this work, we studied the phenotype and protein expression of LX-2 cells upon activation. Strikingly, LX-2 cells undergo a massive change during transformation in metabolism and protein expression related to lipid metabolism, as well as increased proliferation, enhanced migration, and reduced LD volume.

9.1 Hepatic stellate cell activation is associated with an increase in ribosomal biosynthesis, combined with a decrease in lipid metabolism

In this thesis we describe the activation of LX-2 using FBS, which is a method of activation commonly used in HSC *in vitro* research. Although FBS often varies in composition between vendors and batches, FBS has consistently led to activation in LX-2 cells at higher concentrations (e.g., 10 % FBS vs. 1 % FBS). Our work shows that FBS treatment of LX-2 induces activation (Figure 21 A, C), while removal of FBS lowers activation in LX-2 cells (Figure 21 B). We measured these changes in LX-2 activation by observing both α-SMA and COL1A1 protein expression levels by western blotting. Both proteins are reliable markers for HSC activation (123–126).

Proteomic analysis of activated vs. quiescent LX-2 cells revealed enhanced biogenesis of ribosomal proteins (Figure 22 A, Table 3). We suggest this increase in ribosomal proteins is

linked to the rise in protein production[34] and the general re-structuring of cellular components to better fit the activated (myofibroblast) HSC phenotype. In line with our study, rat HSC were shown to increase their ribosomal biogenesis upon activation (131). This phenomenon is further corroborated by an increase in proteins related to amino-acid biosynthesis in activated LX-2 cells compared to control (Figure 23 E). Although not all ribosomal proteins are associated with increased activation[35] of HSC, most ribosomal proteins tend to be associated with an increase in HSC activation. Correspondingly, the increase in ribosomal biogenesis in activated HSC augmented proliferation (Figure 23 A) and proteins involved in proliferation (Figure 23 C) in LX-2 cells treated with 10 % FBS compared to 1 % FBS. Additionally, we could identify upregulated proteins in activated LX-2 cells which are involved in nucleotide biosynthesis (Figure 23 E) implying the need for additional DNA synthesis during enhanced proliferation. Taken together, this combined data suggests elevated protein demand and subsequently enhanced ribosomal protein expression is needed during increased proliferation.

Additionally, we identified a downregulation of many proteins associated with lipid metabolism (Figure 22 A, Table 3) in LX-2 cells grown in 10 % FBS compared to 1 % FBS control. Changes in lipid metabolism were also observed through vastly decreased LD volume during activation of LX-2 cells (Figure 24 D). Specifically fatty acid biosynthetic genes were downregulated in activated LX-2 cells (Figure 23 D) compared to quiescent cells, suggesting a lack of lipid biosynthesis might partially explain the loss of lipid droplets during activation. Other studies have shown that lipid catabolism during activation of HSC can mostly be attributed to lipophagy (133). The catabolism of lipids during activation might provide energy for the transformation of HSC into their active phenotype, supported by findings of lower activation when lipophagy is inhibited in HSC (134).

[34] Figure 21 C shows an increase in COL1A1 production, suggesting enhanced demand for the production of extracellular proteins. Figure 23 C shows additional extracellular matrix proteins upregulated in LX-2 10 % FBS vs. 1 % FBS.

[35] See Xu *et al* 2014 (132) where 40S ribosomal protein S5 (RPS5) OE was associated with a suppression in rat HSC activation. Our data shows upregulation of RPS5 in LX-2 10 % FBS treated cells, compared to 1 % FBS controls.

Interestingly, activated LX-2 cells also show a decrease in proteins involved in the TCA cycle (Figure 23 C). This suggests a shift of HSC to a more glycolytic phenotype during activation (135). Due to the high energy demands during transformation, HSC might preferentially metabolize glucose using aerobic glycolysis rather than mitochondrial respiration. This transition to a glycolytic phenotype might be aided by the provided high-glucose DMEM-media for LX-2 cells.

Activated LX-2 cells also exhibit increased migration and heightened expression of proteins related to migration compared to quiescent controls (Figure 24 B, C; Figure 23 D). This phenomenon is well documented in activated hepatic stellate cells, as they are migrating towards the site of injury in the liver (125).

9.2 PNPLA3 I148M expression in LX-2 cells leads to an increase in KRAS and SRC expression

PNPLA3 I148M is one of the most widespread mutations in liver disease, leading to lipid accumulation in hepatocytes and promoting liver cancer. HSC play an important role in liver cancer, as these cells are involved in liver fibrosis which has strong implications in liver cancer. Interestingly, we identified upregulation of the p38MAPK pathway in LX-2 PNPLA3 I148M vs. wt cells (Figure 27). p38MAPK is part of the RAS/MAPK pathway suggesting increased proliferation in LX-2 cells with PNPLA3 I148M. Yang *et al* 2018 (136) suggests that KRAS might play an important role in changes to the HSC microenvironment. Higher expression of α-SMA and fibrosis markers are detected in patients with the PNPLA3 I148M phenotype compared to wt PNPLA3 (137). Furthermore, primary human HSC carrying the PNPLA3 I148M mutation display higher expression of pro-inflammatory markers (138).

Expression of the mutant PNPLA3 might therefore directly positively influence HSC activation and aid liver disease progression.

9.3 Hepatocyte CGI-58 expression reveals differences in LX-2 growth during treatment with Hep3B pre-conditioned media

The proximity of hepatocytes and HSC in the liver requires a detailed study of their interaction. Co-culturing hepatocytes with lowered CGI-58 expression (CGI-58 KD) and LX-2 cells interestingly revealed a tendency to be decreased in LX-2 activation compared to controls. Although these are preliminary results, due to the noteworthy effects we observed in Hep3B CGI-58 KD cells (see chapter 5.1), lower CGI-58 levels in hepatocytes might influence Hep3B microenvironment and therefore the interaction between hepatocytes and HSC. This change in microenvironment might include the release of signalling molecules and/or a change in the availability of nutrients (although fresh media was mixed in to minimize this effect).

9.4 Conclusion

In conclusion, HSC undergo massive changes in their metabolism, proteome, and general phenotype during activation. Fascinatingly, this transformation from quiescent to an activated phenotype can be directly observed in increased growth, migratory potential, and LD loss. The shift towards a decreased fatty acid biosynthesis when LD are digested indicates a far-reaching re-structuring of HSC constitution and highlights the overarching theme of this thesis of the importance of lipid metabolism in liver cells.

10 Bibliography

1. Schinagl M, Tomin T, Gindlhuber J, Honeder S, Pfleger R, Schittmayer M, et al. Proteomic Changes of Activated Hepatic Stellate Cells. International Journal of Molecular Sciences. 2021 Jan;22(23):12782.

2. Gindlhuber J, Schinagl M, Liesinger L, Darnhofer B, Tomin T, Schittmayer M, et al. Hepatocyte Proteome Alterations Induced by Individual and Combinations of Common Free Fatty Acids. Int J Mol Sci. 2022 Mar 20;23(6):3356.

3. Honeder S, Tomin T, Nebel L, Gindlhuber J, Fritz-Wallace K, Schinagl M, et al. Adipose Triglyceride Lipase Loss Promotes a Metabolic Switch in A549 Non-Small Cell Lung Cancer Cell Spheroids. Mol Cell Proteomics. 2021;20:100095.

4. Tomin T, Bordag N, Zügner E, Al-Baghdadi A, Schinagl M, Birner-Gruenberger R, et al. Blood Plasma Quality Control by Plasma Glutathione Status. Antioxidants (Basel). 2021 May 27;10(6):864.

5. Ferlay J, Colombet M, Soerjomataram I, Parkin DM, Piñeros M, Znaor A, et al. Cancer statistics for the year 2020: An overview. International Journal of Cancer. 2021;149(4):778–89.

6. Ferlay J, Laversanne M, Ervik M, Lam F, Colombet M, Mery L, et al. Global Cancer Observatory: Cancer Tomorrow. [Internet]. Global Cancer Observatory: Cancer Tomorrow. [cited 2023 Jan 4]. Available from: https://gco.iarc.fr/tomorrow

7. Siegel RL, Miller KD, Fuchs HE, Jemal A. Cancer statistics, 2022. CA: A Cancer Journal for Clinicians. 2022;72(1):7–33.

8. Kew MC. Aflatoxins as a Cause of Hepatocellular Carcinoma. Journal of Gastrointestinal and Liver Diseases. 2013 Sep 1;22(3):305–10.

9. Finucane MM, Stevens GA, Cowan MJ, Danaei G, Lin JK, Paciorek CJ, et al. National, regional, and global trends in body-mass index since 1980: systematic analysis of health examination surveys and epidemiological studies with 960 country-years and 9·1 million participants. The Lancet. 2011 Feb 12;377(9765):557–67.

10. Abarca-Gómez L, Abdeen ZA, Hamid ZA, Abu-Rmeileh NM, Acosta-Cazares B, Acuin C, et al. Worldwide trends in body-mass index, underweight, overweight, and obesity from 1975 to 2016: a pooled analysis of 2416 population-based measurement studies in 128·9 million children, adolescents, and adults. The Lancet. 2017 Dec 16;390(10113):2627–42.

11. Michalopoulos GK, DeFrances MC. Liver Regeneration. Science. 1997 Apr 4;276(5309):60–6.

12. Roskams T. Relationships Among Stellate Cell Activation, Progenitor Cells, and Hepatic Regeneration. Clinics in Liver Disease. 2008 Nov 1;12(4):853–60.

13. Yin C, Evason KJ, Asahina K, Stainier DYR. Hepatic stellate cells in liver development, regeneration, and cancer. J Clin Invest. 2013 May 1;123(5):1902–10.

14. Singal AK. Similarities and differences between non-alcoholic fatty liver disease (NAFLD) & alcohol-associated liver disease (ALD). Transl Gastroenterol Hepatol. 2021 Jan 5;6:1.

15. Seitz HK, Mueller S. Alcoholic Liver Disease. In Springer; 2010. p. 1111–51.

16. Friedman SL, Neuschwander-Tetri BA, Rinella M, Sanyal AJ. Mechanisms of NAFLD development and therapeutic strategies. Nat Med. 2018 Jul;24(7):908–22.

17. Golabi P, Paik JM, Eberly K, de Avila L, Alqahtani SA, Younossi ZM. Causes of death in patients with Non-alcoholic Fatty Liver Disease (NAFLD), alcoholic liver disease and chronic viral Hepatitis B and C. Annals of Hepatology. 2022 Jan 1;27(1):100556.

18. Aniemeka C, Pillai AA. HCC Mortality Trends—In with ALD (and NAFLD) and Out with HCV. Dig Dis Sci. 2022 Aug 1;67(8):3483–4.

19. Huang DQ, El-Serag HB, Loomba R. Global epidemiology of NAFLD-related HCC: trends, predictions, risk factors and prevention. Nat Rev Gastroenterol Hepatol. 2021 Apr;18(4):223–38.

20. Testino G, Leone S, Borro P. Alcohol and hepatocellular carcinoma: A review and a point of view. World J Gastroenterol. 2014 Nov 21;20(43):15943–54.

21. Loomba R, Sanyal AJ. The global NAFLD epidemic. Nat Rev Gastroenterol Hepatol. 2013 Nov;10(11):686–90.

22. Graffy PM, Pickhardt PJ. Quantification of hepatic and visceral fat by CT and MR imaging: relevance to the obesity epidemic, metabolic syndrome and NAFLD. BJR. 2016 Jun;89(1062):20151024.

23. Asrani SK, Devarbhavi H, Eaton J, Kamath PS. Burden of liver diseases in the world. Journal of Hepatology. 2019 Jan 1;70(1):151–71.

24. Singh S, Osna NA, Kharbanda KK. Treatment options for alcoholic and non-alcoholic fatty liver disease: A review. World J Gastroenterol. 2017 Sep 28;23(36):6549–70.

25. Briasoulis A, Agarwal V, Messerli FH. Alcohol Consumption and the Risk of Hypertension in Men and Women: A Systematic Review and Meta-Analysis: Alcohol and Hypertension. The Journal of Clinical Hypertension. 2012 Nov;14(11):792–8.

26. Crabb DW, Bosron WF, Li TK. Ethanol metabolism. Pharmacology & Therapeutics. 1987 Jan 1;34(1):59–73.

27. Northfield TC, Ahmed H, Jazwari R, Zentler-Munro P. Bile Acids in Hepatobiliary Disease. Springer Science & Business Media; 2000. 366 p.

28. Baraona E, Lieber CS. Effects of ethanol on lipid metabolism. Journal of Lipid Research. 1979 Mar;20(3):289–315.

29. Ontko JA. Effects of ethanol on the metabolism of free fatty acids in isolated liver cells. Journal of Lipid Research. 1973 Jan;14(1):78–86.

30. You M, Fischer M, Deeg MA, Crabb DW. Ethanol Induces Fatty Acid Synthesis Pathways by Activation of Sterol Regulatory Element-binding Protein (SREBP). Journal of Biological Chemistry. 2002 Aug 9;277(32):29342–7.

31. Galli A, Pinaire J, Fischer M, Dorris R, Crabb DW. The Transcriptional and DNA Binding Activity of Peroxisome Proliferator-activated Receptor α Is Inhibited by Ethanol Metabolism: A Novel Mechanism for The Development of Ethanol-Induced Fatty Liver. Journal of Biological Chemistry. 2001 Jan 5;276(1):68–75.

32. Lieber CS. Alcoholic fatty liver: its pathogenesis and mechanism of progression to inflammation and fibrosis. Alcohol. 2004 Aug 1;34(1):9–19.

33. Morgan MY. The prognosis and outcome of alcoholic liver disease. Alcohol Alcohol Suppl. 1994 Jan 1;2:335–43.

34. Ortega FB, Lavie CJ, Blair SN. Obesity and Cardiovascular Disease. Circulation Research. 2016 May 27;118(11):1752–70.

35. Angulo P. Nonalcoholic Fatty Liver Disease. New England Journal of Medicine. 2002 Apr 18;346(16):1221–31.

36. Anstee QM, Day CP. 26 - Epidemiology, Natural History, and Evaluation of Nonalcoholic Fatty Liver Disease. In: Sanyal AJ, Boyer TD, Lindor KD, Terrault NA, editors. Zakim and Boyer's Hepatology. 7th ed. Philadelphia: Elsevier; 2018. p. 391-405.e3.

37. Engin AB, Engin A, editors. Obesity and Lipotoxicity. Cham: Springer International Publishing; 2017. (Advances in Experimental Medicine and Biology; vol. 960).

38. Farrell GC, Haczeyni F, Chitturi S. Pathogenesis of NASH: How Metabolic Complications of Overnutrition Favour Lipotoxicity and Pro-Inflammatory Fatty Liver Disease. In: Yu J, editor. Obesity, Fatty Liver and Liver Cancer. Singapore: Springer Singapore; 2018. p. 19–44. (Advances in Experimental Medicine and Biology; vol. 1061).

39. Wallace K, Burt AD, Wright MC. Liver fibrosis. Biochemical Journal. 2008 Mar 13;411(1):1–18.

40. Jung YK, Yim HJ. Reversal of liver cirrhosis: current evidence and expectations. Korean J Intern Med. 2017 Mar;32(2):213–28.

41. Dezső K, Paku S, Kóbori L, Thorgeirsson SS, Nagy P. What Makes Cirrhosis Irreversible?—Consideration on Structural Changes. Frontiers in Medicine. 2022 Apr 27;9:1–6.

42. Schuppan D, Afdhal NH. Liver cirrhosis. The Lancet. 2008 Mar 8;371(9615):838–51.

43. Colombo M, de Franchis R, Del Ninno E, Sangiovanni A, De Fazio C, Tommasini M, et al. Hepatocellular Carcinoma in Italian Patients with Cirrhosis. New England Journal of Medicine. 1991 Sep 5;325(10):675–80.

44. Friedman SL. Molecular Regulation of Hepatic Fibrosis, an Integrated Cellular Response to Tissue Injury*. Journal of Biological Chemistry. 2000 Jan 28;275(4):2247–50.

45. Eng FJ, Friedman SL. Fibrogenesis I. New insights into hepatic stellate cell activation: the simple becomes complex. American Journal of Physiology-Gastrointestinal and Liver Physiology. 2000 Jul;279(1):G7–11.

46. Ginès P, Cárdenas A, Arroyo V, Rodés J. Management of Cirrhosis and Ascites. New England Journal of Medicine. 2004 Apr 15;350(16):1646–54.

47. Plauth M, Schütz ET. Cachexia in liver cirrhosis. International Journal of Cardiology. 2002 Sep 1;85(1):83–7.

48. Bréchot C, Gozuacik D, Murakami Y, Paterlini-Bréchot P. Molecular bases for the development of hepatitis B virus (HBV)-related hepatocellular carcinoma (HCC). Seminars in Cancer Biology. 2000 Jun 1;10(3):211–31.

49. Kanwal F, Hoang T, Kramer JR, Asch SM, Goetz MB, Zeringue A, et al. Increasing Prevalence of HCC and Cirrhosis in Patients With Chronic Hepatitis C Virus Infection. Gastroenterology. 2011 Apr 1;140(4):1182-1188.e1.

50. Pavelka M, Roth J, editors. Smooth Endoplasmic Reticulum. In: Functional Ultrastructure: An Atlas of Tissue Biology and Pathology. 1st ed. Vienna: Springer; 2005. p. 38–9.

51. Kuntz E, Kuntz HD. Hepatology: textbook and atlas history, morphology, biochemistry, diagnostics, clinic, therapy. 3rd ed. Heidelberg: Springer Medizin Verlag; 2008.

52. Moriwaki H, Blaner WS, Piantedosi R, Goodman DS. Effects of dietary retinoid and triglyceride on the lipid composition of rat liver stellate cells and stellate cell lipid droplets. Journal of Lipid Research. 1988 Nov 1;29(11):1523–34.

53. Trivedi P, Wang S, Friedman SL. The Power of Plasticity—Metabolic Regulation of Hepatic Stellate Cells. Cell Metabolism. 2021 Feb 2;33(2):242–57.

54. Maher JJ. Interactions between Hepatic Stellate Cells and the Immune System. Semin Liver Dis. 2001;21(3):417–26.

55. Huang Y, Deng X, Liang J. Modulation of hepatic stellate cells and reversibility of hepatic fibrosis. Experimental Cell Research. 2017 Mar 15;352(2):420–6.

56. Iqbal J, Hussain MM. Intestinal lipid absorption. American Journal of Physiology-Endocrinology and Metabolism. 2009 Jun;296(6):E1183–94.

57. Zimmermann R, Strauss JG, Haemmerle G, Schoiswohl G, Birner-Gruenberger R, Riederer M, et al. Fat Mobilization in Adipose Tissue Is Promoted by Adipose Triglyceride Lipase. Science. 2004 Nov 19;306(5700):1383–6.

58. Karlsson M, Zhang C, Méar L, Zhong W, Digre A, Katona B, et al. A single–cell type transcriptomics map of human tissues. Science Advances. 2021 Jul 28;7(31):eabh2169.

59. Kraemer FB, Shen WJ. Hormone-sensitive lipase. Journal of Lipid Research. 2002 Oct 1;43(10):1585–94.

60. Fredrikson G, Tornqvist H, Belfrage P. Hormone-sensitive lipase and monoacylglycerol lipase are both required for complete degradation of adipocyte triacylglycerol. Biochimica et Biophysica Acta (BBA) - Lipids and Lipid Metabolism. 1986 Apr 15;876(2):288–93.

61. Honeder SE, Tomin T, Schinagl M, Pfleger R, Hoehlschen J, Darnhofer B, et al. Research Advances Through Activity-Based Lipid Hydrolase Profiling. Israel Journal of Chemistry. 2023;63(3–4):e202200078.

62. Lass A, Zimmermann R, Haemmerle G, Riederer M, Schoiswohl G, Schweiger M, et al. Adipose triglyceride lipase-mediated lipolysis of cellular fat stores is activated by CGI-58 and defective in Chanarin-Dorfman Syndrome. Cell Metabolism. 2006 May 1;3(5):309–19.

63. De A, Duseja A. Natural History of Simple Steatosis or Nonalcoholic Fatty Liver. Journal of Clinical and Experimental Hepatology. 2020 May 1;10(3):255–62.

64. Haemmerle G, Lass A, Zimmermann R, Gorkiewicz G, Meyer C, Rozman J, et al. Defective Lipolysis and Altered Energy Metabolism in Mice Lacking Adipose Triglyceride Lipase. Science. 2006 May 5;312(5774):734–7.

65. Radner FPW, Streith IE, Schoiswohl G, Schweiger M, Kumari M, Eichmann TO, et al. Growth Retardation, Impaired Triacylglycerol Catabolism, Hepatic Steatosis, and Lethal Skin Barrier Defect in Mice Lacking Comparative Gene Identification-58 (CGI-58)*. Journal of Biological Chemistry. 2010 Mar 5;285(10):7300–11.

66. Schreiber R, Xie H, Schweiger M. Of mice and men: The physiological role of adipose triglyceride lipase (ATGL). Biochimica et Biophysica Acta (BBA) - Molecular and Cell Biology of Lipids. 2019 Jun 1;1864(6):880–99.

67. Hoy AJ, Bruce CR, Turpin SM, Morris AJ, Febbraio MA, Watt MJ. Adipose Triglyceride Lipase-Null Mice Are Resistant to High-Fat Diet–Induced Insulin Resistance Despite Reduced Energy Expenditure and Ectopic Lipid Accumulation. Endocrinology. 2011 Jan 1;152(1):48–58.

68. Wu JW, Wang SP, Alvarez F, Casavant S, Gauthier N, Abed L, et al. Deficiency of liver adipose triglyceride lipase in mice causes progressive hepatic steatosis. Hepatology. 2011;54(1):122–32.

69. Schweiger M, Romauch M, Schreiber R, Grabner GF, Hütter S, Kotzbeck P, et al. Pharmacological inhibition of adipose triglyceride lipase corrects high-fat diet-induced insulin resistance and hepatosteatosis in mice. Nat Commun. 2017 Mar 22;8(1):14859.

70. Schreiber R, Hofer P, Taschler U, Voshol PJ, Rechberger GN, Kotzbeck P, et al. Hypophagia and metabolic adaptations in mice with defective ATGL-mediated lipolysis cause resistance to HFD-induced obesity. Proc Natl Acad Sci USA. 2015 Nov 10;112(45):13850–5.

71. Schweiger M, Lass A, Zimmermann R, Eichmann TO, Zechner R. Neutral lipid storage disease: genetic disorders caused by mutations in adipose triglyceride lipase/PNPLA2 or CGI-58/ABHD5. American Journal of Physiology-Endocrinology and Metabolism. 2009 Aug 1;297(2):E289–96.

72. Albert JS, Yerges-Armstrong LM, Horenstein RB, Pollin TI, Sreenivasan UT, Chai S, et al. Null Mutation in Hormone-Sensitive Lipase Gene and Risk of Type 2 Diabetes. N Engl J Med. 2014 Jun 12;370(24):2307–15.

73. Yin H, Li W, Mo L, Deng S, Lin W, Ma C, et al. Adipose triglyceride lipase promotes the proliferation of colorectal cancer cells via enhancing the lipolytic pathway. Journal of Cellular and Molecular Medicine. 2021;25(8):3963–75.

74. Zagani R, El-Assaad W, Gamache I, Teodoro JG. Inhibition of adipose triglyceride lipase (ATGL) by the putative tumor suppressor G0S2 or a small molecule inhibitor attenuates the growth of cancer cells. Oncotarget. 2015 Jul 31;6(29):28282–95.

75. Tomin T, Fritz K, Gindlhuber J, Waldherr L, Pucher B, Thallinger GG, et al. Deletion of Adipose Triglyceride Lipase Links Triacylglycerol Accumulation to a More-Aggressive Phenotype in A549 Lung Carcinoma Cells. J Proteome Res. 2018 Apr 6;17(4):1415–25.

76. Di Leo L, Vegliante R, Ciccarone F, Salvatori I, Scimeca M, Bonanno E, et al. Forcing ATGL expression in hepatocarcinoma cells imposes glycolytic rewiring through PPAR-α/p300-mediated acetylation of p53. Oncogene. 2019 Mar;38(11):1860–75.

77. Vegliante R, Di Leo L, Ciccarone F, Ciriolo MR. Hints on ATGL implications in cancer: beyond bioenergetic clues. Cell Death Dis. 2018 Feb 22;9(3):1–10.

78. Yang P, Wang Y, Tang W, Sun W, Ma Y, Lin S, et al. Western diet induces severe nonalcoholic steatohepatitis, ductular reaction, and hepatic fibrosis in liver CGI-58 knockout mice. Scientific Reports. 2020 Mar 13;10(1):4701.

79. Yu L, Li Y, Grisé A, Wang H. CGI-58: Versatile Regulator of Intracellular Lipid Droplet Homeostasis. Adv Exp Med Biol. 2020;1276:197–222.

80. Jarc E, Eichmann TO, Zimmermann R, Petan T. Lipidomic data on lipid droplet triglyceride remodelling associated with protection of breast cancer cells from lipotoxic stress. Data in Brief. 2018 Jun 1;18:234–40.

81. Vander Heiden MG, Cantley LC, Thompson CB. Understanding the Warburg Effect: The Metabolic Requirements of Cell Proliferation. Science. 2009 May 22;324(5930):1029–33.

82. Ou J, Miao H, Ma Y, Guo F, Deng J, Wei X, et al. Loss of Abhd5 Promotes Colorectal Tumor Development and Progression by Inducing Aerobic Glycolysis and Epithelial-Mesenchymal Transition. Cell Reports. 2014 Dec 11;9(5):1798–811.

83. Peng Y, Miao H, Wu S, Yang W, Zhang Y, Xie G, et al. ABHD5 interacts with BECN1 to regulate autophagy and tumorigenesis of colon cancer independent of PNPLA2. Autophagy. 2016 Aug 25;12(11):2167–82.

84. Chen G, Zhou G, Aras S, He Z, Lucas S, Podgorski I, et al. Loss of ABHD5 promotes the aggressiveness of prostate cancer cells. Sci Rep. 2017 Oct 12;7:13021.

85. Zhou Q, Wang F, Zhou K, Huang K, Zhu Q, Luo X, et al. Oncogenic role of ABHD5 in endometrial cancer. Cancer Manag Res. 2019 Mar 14;11:2139–50.

86. Cakmak E, Bagci G. Chanarin-Dorfman Syndrome: A comprehensive review. Liver International. 2021 May;41(5):905–14.

87. Basantani MK, Sitnick MT, Cai L, Brenner DS, Gardner NP, Li JZ, et al. Pnpla3/Adiponutrin deficiency in mice does not contribute to fatty liver disease or metabolic syndrome [S]. Journal of Lipid Research. 2011 Feb 1;52(2):318–29.

88. Romeo S, Kozlitina J, Xing C, Pertsemlidis A, Cox D, Pennacchio LA, et al. Genetic variation in PNPLA3 confers susceptibility to nonalcoholic fatty liver disease. Nat Genet. 2008 Dec;40(12):1461–5.

89. Romeo S, Savage DB. Lipase tug of war: PNPLA3 sequesters ABHD5 from ATGL. Nat Metab. 2019 May;1(5):505–6.

90. Trepo E, Guyot E, Ganne-Carrie N, Degre D, Gustot T, Franchimont D, et al. PNPLA3 (rs738409 C>G) is a common risk variant associated with hepatocellular carcinoma in alcoholic cirrhosis. Hepatology. 2012;55(4):1307–8.

91. Sookoian S, Castaño GO, Burgueño AL, Gianotti TF, Rosselli MS, Pirola CJ. A nonsynonymous gene variant in the adiponutrin gene is associated with nonalcoholic fatty liver disease severity. J Lipid Res. 2009 Oct;50(10):2111–6.

92. Valenti L, Rumi M, Galmozzi E, Aghemo A, Del Menico B, De Nicola S, et al. Patatin-Like phospholipase domain-containing 3 I148M polymorphism, steatosis, and liver damage in chronic hepatitis C. Hepatology. 2011;53(3):791–9.

93. Uhlén M, Fagerberg L, Hallström BM, Lindskog C, Oksvold P, Mardinoglu A, et al. Tissue-based map of the human proteome. Science. 2015 Jan 23;347(6220):1260419.

94. Trépo E, Romeo S, Zucman-Rossi J, Nahon P. PNPLA3 gene in liver diseases. Journal of Hepatology. 2016 Aug 1;65(2):399–412.

95. Meier F, Brunner AD, Koch S, Koch H, Lubeck M, Krause M, et al. Online Parallel Accumulation-Serial Fragmentation (PASEF) with a Novel Trapped Ion Mobility Mass Spectrometer. Mol Cell Proteomics. 2018 Dec;17(12):2534–45.

96. Cox J, Matic I, Hilger M, Nagaraj N, Selbach M, Olsen JV, et al. A practical guide to the MaxQuant computational platform for SILAC-based quantitative proteomics. Nat Protoc. 2009 May;4(5):698–705.

97. Tyanova S, Temu T, Sinitcyn P, Carlson A, Hein MY, Geiger T, et al. The Perseus computational platform for comprehensive analysis of (prote)omics data. Nat Methods. 2016 Sep;13(9):731–40.

98. Shannon P. Cytoscape: A Software Environment for Integrated Models of Biomolecular Interaction Networks. Genome Research. 2003 Nov 1;13(11):2498–504.

99. Szklarczyk D, Gable AL, Nastou KC, Lyon D, Kirsch R, Pyysalo S, et al. The STRING database in 2021: customizable protein-protein networks, and functional characterization of user-uploaded gene/measurement sets. Nucleic Acids Res. 2021 Jan 8;49(D1):D605–12.

100. Perez-Riverol Y, Csordas A, Bai J, Bernal-Llinares M, Hewapathirana S, Kundu DJ, et al. The PRIDE database and related tools and resources in 2019: improving support for quantification data. Nucleic Acids Research. 2019 Jan 8;47(D1):D442–50.

101. Schindelin J, Arganda-Carreras I, Frise E, Kaynig V, Longair M, Pietzsch T, et al. Fiji: an open-source platform for biological-image analysis. Nat Methods. 2012 Jul;9(7):676–82.

102. Goldman MJ, Craft B, Hastie M, Repečka K, McDade F, Kamath A, et al. Visualizing and interpreting cancer genomics data via the Xena platform. Nat Biotechnol. 2020 Jun;38(6):675–8.

103. Cai D, Latham VM Jr, Zhang X, Shapiro GI. Combined Depletion of Cell Cycle and Transcriptional Cyclin-Dependent Kinase Activities Induces Apoptosis in Cancer Cells. Cancer Research. 2006 Sep 18;66(18):9270–80.

104. González A, Jiménez A, Vázquez D, Davies JE, Schindler D. Studies on the mode of action of hygromycin B, an inhibitor of translocation in eukaryotes. Biochimica et Biophysica Acta (BBA) - Nucleic Acids and Protein Synthesis. 1978 Dec 21;521(2):459–69.

105. de Seny D, Bianchi E, Baiwir D, Cobraiville G, Collin C, Deliège M, et al. Proteins involved in the endoplasmic reticulum stress are modulated in synovitis of osteoarthritis, chronic pyrophosphate arthropathy and rheumatoid arthritis, and correlate with the histological inflammatory score. Sci Rep. 2020 Sep 4;10(1):14159.

106. Wendeler MW, Paccaud JP, Hauri HP. Role of Sec24 isoforms in selective export of membrane proteins from the endoplasmic reticulum. EMBO reports. 2007 Mar 1;8(3):258–64.

107. Ip WK, Lai PBS, Wong NLY, Sy SMH, Beheshti B, Squire JA, et al. Identification of PEG10 as a progression related biomarker for hepatocellular carcinoma. Cancer Letters. 2007 Jun 8;250(2):284–91.

108. Schneeberger PE, Nampoothiri S, Holling T, Yesodharan D, Alawi M, Knisely AS, et al. Biallelic variants in VPS50 cause a neurodevelopmental disorder with neonatal cholestasis. Brain. 2021 Oct 1;144(10):3036–49.

109. Cao B, Deng H, Cui H, Zhao R, Li H, Wei B, et al. Knockdown of PGM1 enhances anti-cancer effects of orlistat in gastric cancer under glucose deprivation. Cancer Cell Int. 2021 Dec;21(1):1–15.

110. Paolini E, Longo M, Meroni M, Tria G, Cespiati A, Lombardi R, et al. The I148M PNPLA3 variant mitigates niacin beneficial effects: How the genetic screening in non-alcoholic fatty liver disease patients gains value. Frontiers in Nutrition. 2023 Mar 2;10.

111. Vicens Q, Westhof E. Crystal Structure of Geneticin Bound to a Bacterial 16S Ribosomal RNA A Site Oligonucleotide. Journal of Molecular Biology. 2003 Feb 28;326(4):1175–88.

112. Zhou Y, Tao J, Calvisi DF, Chen X. Role of Lipogenesis Rewiring in Hepatocellular Carcinoma. Semin Liver Dis. 2022 Feb 1;42(1):77–86.

113. Harris KA, Harrison CD, Thacker CR, Ballard D, Musgrave-Brown E, Syndercombe-Court YD. Molecular analysis of the PGM1 phenotype. Forensic Science International: Genetics Supplement Series. 2008 Aug 1;1(1):559–60.

114. Jin GZ, Zhang Y, Cong WM, Wu X, Wang X, Wu S, et al. Phosphoglucomutase 1 inhibits hepatocellular carcinoma progression by regulating glucose trafficking. PLOS Biology. 2018 Oct 18;16(10):e2006483.

115. Walczak R, Tontonoz P. PPARadigms and PPARadoxes: expanding roles for PPARγ in the control of lipid metabolism. Journal of Lipid Research. 2002 Feb 1;43(2):177–86.

116. Yoon M. The role of PPARα in lipid metabolism and obesity: Focusing on the effects of estrogen on PPARα actions. Pharmacological Research. 2009 Sep 1;60(3):151–9.

117. Dubuquoy C, Robichon C, Lasnier F, Langlois C, Dugail I, Foufelle F, et al. Distinct regulation of adiponutrin/PNPLA3 gene expression by the transcription factors ChREBP and SREBP1c in mouse and human hepatocytes. Journal of Hepatology. 2011 Jul 1;55(1):145–53.

118. Smagris E, BasuRay S, Li J, Huang Y, Lai K man V, Gromada J, et al. Pnpla3I148M knockin mice accumulate PNPLA3 on lipid droplets and develop hepatic steatosis. Hepatology. 2015;61(1):108–18.

119. Senoo H. Structure and function of hepatic stellate cells. Med Electron Microsc. 2004 Mar 1;37(1):3–15.

120. Tsuchida T, Friedman SL. Mechanisms of hepatic stellate cell activation. Nat Rev Gastroenterol Hepatol. 2017 Jul;14(7):397–411.

121. Rockey DC. Hepatic Blood Flow Regulation by Stellate Cells in Normal and Injured Liver. Semin Liver Dis. 2001;21(03):337–50.

122. Wang BB, Cheng JY, Gao HH, Zhang Y, Chen ZN, Bian H. Hepatic Stellate Cells in Inflammation-Fibrosis-Carcinoma Axis. Anat Rec. 2010 Sep;293(9):1492–6.

123. Hinz B, Celetta G, Tomasek JJ, Gabbiani G, Chaponnier C. Alpha-Smooth Muscle Actin Expression Upregulates Fibroblast Contractile Activity. Matsudaira PT, editor. MBoC. 2001 Sep;12(9):2730–41.

124. Tanaka Y, Nouchi T, Yamane M, Irie T, Miyakawa H, Sato C, et al. Phenotypic modulation in lipocytes in experimental liver fibrosis. J Pathol. 1991 Jul;164(3):273–8.

125. Hautekeete ML, Geerts A. The hepatic stellate (Ito) cell: its role in human liver disease. Virchows Archiv. 1997 Mar;430(3):195–207.

126. Varela-Rey M, Montiel-Duarte C, Osés-Prieto JA, López-Zabalza MJ, Jaffrèzou JP, Rojkind M, et al. p38 MAPK mediates the regulation of α1(I) procollagen mRNA levels by TNF-α and TGF-β in a cell line of rat hepatic stellate cells. FEBS Letters. 2002 Sep 25;528(1):133–8.

127. Taimr P, Higuchi H, Kocova E, Rippe RA, Friedman S, Gores GJ. Activated stellate cells express the TRAIL receptor-2/death receptor-5 and undergo TRAIL-mediated apoptosis. Hepatology. 2003;37(1):87–95.

128. de Oliveira da Silva B, Alberici LC, Ramos LF, Silva CM, da Silveira MB, Dechant CRP, et al. Altered global microRNA expression in hepatic stellate cells LX-2 by angiotensin-(1–7) and miRNA-1914-5p identification as regulator of pro-fibrogenic elements and lipid metabolism. The International Journal of Biochemistry & Cell Biology. 2018 May 1;98:137–55.

129. Zhao XY, Zeng X, Li XM, Wang TL, Wang BE. Pirfenidone inhibits carbon tetrachloride- and albumin complex-induced liver fibrosis in rodents by preventing activation of hepatic stellate cells. Clinical and Experimental Pharmacology and Physiology. 2009 Oct;36(10):963–8.

130. Xu L. Human hepatic stellate cell lines, LX-1 and LX-2: new tools for analysis of hepatic fibrosis. Gut. 2005 Jan 1;54(1):142–51.

131. Ouyang Y, Guo J, Lin C, Lin J, Cao Y, Zhang Y, et al. Transcriptomic analysis of the effects of Toll-like receptor 4 and its ligands on the gene expression network of hepatic stellate cells. Fibrogenesis & Tissue Repair. 2016 Feb 18;9(1):2.

132. Xu WH, Hu HG, Tian Y, Wang SZ, Li J, Li JZ, et al. Bioactive compound reveals a novel function for ribosomal protein S5 in hepatic stellate cell activation and hepatic fibrosis. Hepatology. 2014;60(2):648–60.

133. Mastoridou EM, Goussia AC, Glantzounis GK, Kanavaros P, Charchanti AV. Autophagy and Exosomes: Cross-Regulated Pathways Playing Major Roles in Hepatic Stellate Cells Activation and Liver Fibrosis. Frontiers in Physiology. 2022 Feb 3;12.

134. Hernández–Gea V, Ghiassi–Nejad Z, Rozenfeld R, Gordon R, Fiel MI, Yue Z, et al. Autophagy Releases Lipid That Promotes Fibrogenesis by Activated Hepatic Stellate Cells in Mice and in Human Tissues. Gastroenterology. 2012 Apr;142(4):938–46.

135. Chen Y, Choi SS, Michelotti GA, Chan IS, Swiderska-Syn M, Karaca GF, et al. Hedgehog Controls Hepatic Stellate Cell Fate by Regulating Metabolism. Gastroenterology. 2012 Nov 1;143(5):1319-1329.e11.

136. Yang Q, Yan C, Gong Z. Interaction of hepatic stellate cells with neutrophils and macrophages in the liver following oncogenic kras activation in transgenic zebrafish. Sci Rep. 2018 May 31;8(1):8495.

137. Bruschi FV, Tardelli M, Herac M, Claudel T, Trauner M. Metabolic regulation of hepatic PNPLA3 expression and severity of liver fibrosis in patients with NASH. Liver International. 2020 Feb 11;40(5):1098–110.

138. Bruschi FV, Claudel T, Tardelli M, Caligiuri A, Stulnig TM, Marra F, et al. The PNPLA3 I148M variant modulates the fibrogenic phenotype of human hepatic stellate cells. Hepatology. 2017;65(6):1875–90.

11 Appendix

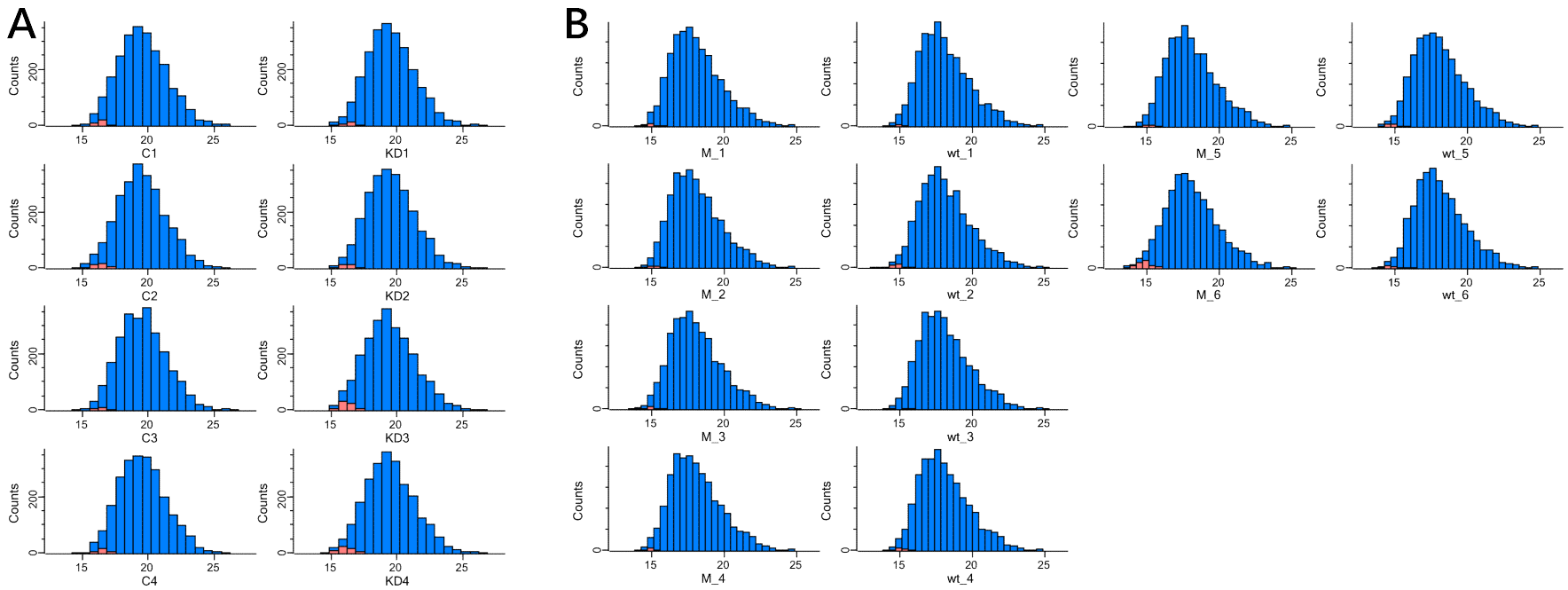

Figure 29: Imputed values of proteomics studies on Hep3B cells. Histogram graphical representation of imputed values created in Perseus. Missing values were imputed separately for each column with a width of 0.3 and a down-shift of 1.8. Blue columns represent measured values. Red columns represent imputed values. **(A)** Hep3B CGI-58 KD and control proteomics measurements. **(B)** Hep3B PNPLA3 I148M (M) and PNPLA3 wt proteomics measurements.

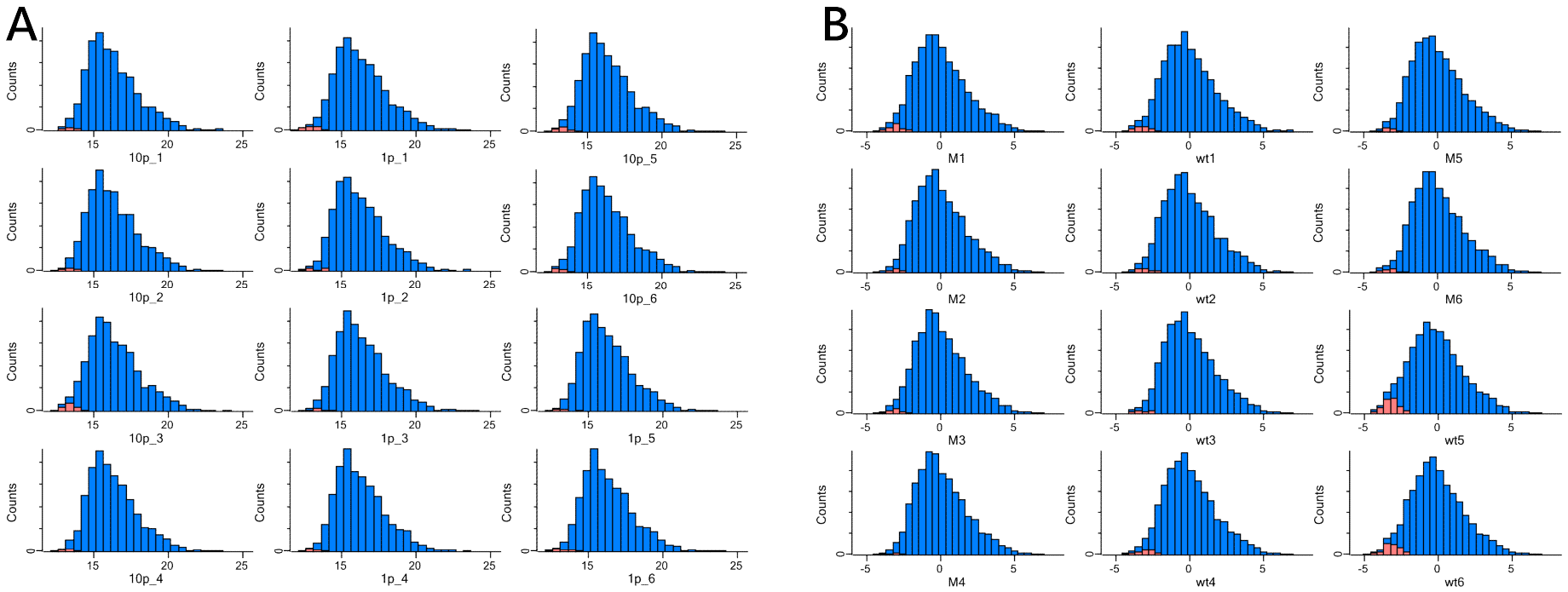

Figure 30: Imputed values of proteomics studies on LX-2 cells. Histogram graphical representation of imputed values created in Perseus. Missing values were imputed separately for each column with a width of 0.3 and a down-shift of 1.8. Blue columns represent measured values. Red columns represent imputed values. (A) LX-2 10 % FBS vs. 1 % FBS control proteomics measurements. (B) LX-2 PNPLA3 I148M (M) vs. PNPLA3 wt proteomics measurements.

Table 4: List of proteins with statistically significant (two-sample t-test, two sided, without multi-testing correction, S_0 = 0.01, p < 0.05) changes in expression Hep3B CGI-58 KD vs. control. FC = fold change.

GENE NAME	LOG2 FC HEP3B CGI-58 KD-C
ASNA1	-5,4612
S100A13	-3,8659
PIN4	-3,5102
B4GAT1	-3,4553
TFAM	-3,2621
UBE2M	-3,1349
ARF4	-3,0537
DENR	-2,9882
MRPL39	-2,8312
PWP2	-2,6895
SEC24A	-2,5473
BZW1	-2,5140
DDX20	-2,3363
ACADSB	-2,2215
GTPBP1	-2,2162
ACSS3	-2,2020
TP53RK	-2,1560
PBXIP1	-2,0949
LSR	-2,0416
NUP35	-2,0350
HUS1	-2,0096
PRPF38A	-1,9931
DNPH1	-1,9857
CARS2	-1,9833
SULT1A1	-1,9013
PATL1	-1,8713
NCAPG2	-1,8450
LARP4B	-1,8299
LIN28B	-1,8208
SEP15	-1,6931
RABGGTA	-1,6733
TMEM181	-1,6061
CAB39	-1,6002
TRMT1	-1,5886
CCDC132	-1,4883
LIG3	-1,4475
PEG10	-1,3199
SEL1L	-1,2909
RAB5A	-1,2340
TGOLN2	-1,1979
UBXN1	-1,1068
NT5E	-1,1040
WDR26	-1,0375
TST	-0,9874
SAMHD1	-0,9553
CALU	-0,9190
PSIP1	-0,9136
SF3B5	-0,9108
FAM169A	-0,8822
ARHGAP1	-0,8819
ANAPC7	-0,8750
MTTP	-0,8623
ARHGEF18	-0,8517
UBA3	-0,8476
MINA	-0,8434
POLDIP2	-0,7968
GPC6	-0,7893
RAD23A	-0,7745
RELN	-0,7671
SF3B4	-0,7417
BRIX1	-0,7169
IPO11	-0,7051
SBF1	-0,6946
HSPA1B;HSPA1A	-0,6932
CHID1	-0,6917
RCN1	-0,6802
PYCR1	-0,6551
BCKDHA	-0,6528
ZFYVE19	-0,6500
HMGN1	-0,6462
TIMMDC1	-0,6461
U2SURP	-0,6174
PEX5	-0,6034
DIS3	-0,6024
HIBADH	-0,6016
MESDC2	-0,5937
HMGN5	-0,5689
PGRMC2	-0,5653
UBA2	-0,5602
AP3B1	-0,5599
HN1	-0,5531
IST1	-0,5530
RPAP1	-0,5498
PNPO	-0,5424
TF	-0,5379
CEACAM1	-0,5359
SH3GL1	-0,5328
EPS15L1	-0,5318
SNRPD3	-0,5298
IKBKAP	-0,5284
PLCG1	-0,5248
FBL	-0,5247
NFKB1	-0,5241
BOD1L1	-0,5213
GANAB	-0,5200
DBNL	-0,5154
DEK	-0,5136
EP300	-0,5102
DNAJA2	-0,5076
PYGL	-0,5037
RBM8A	-0,5012
CECR5	-0,4958
PGM1	-0,4854
ASPH	-0,4848
LNPEP	-0,4777
BCLAF1	-0,4773
AGT	-0,4745
EHBP1	-0,4701
RPL6	-0,4687
RRBP1	-0,4673
POR	-0,4670
NUMA1	-0,4670
PPP1R10	-0,4608
FANCI	-0,4556
PPP1R7	-0,4552
CALR	-0,4521
ZNF687	-0,4504
ZC3H15	-0,4477
USP9X	-0,4469
SMARCC1	-0,4466
POLE4	-0,4449
CAP1	-0,4415
PMVK	-0,4398
NUDT21	-0,4392
AKAP12	-0,4367
LUC7L3	-0,4366
NNT	-0,4339
BCAS3	-0,4294
PDXDC1	-0,4280
RBM19	-0,4280
DDX1	-0,4212
CDV3	-0,4189
PRKCSH	-0,4140
TPP2	-0,4097
CANX	-0,4085
UHRF1BP1	-0,4053
FARSA	-0,4035
ITPR3	-0,4033
FAM120A	-0,4020
RTFDC1	-0,3995
NUDT5	-0,3989
U2AF2	-0,3988
TRIM24	-0,3909
FNBP1L	-0,3908
MTAP	-0,3895
GFM1	-0,3893
IMMT	-0,3892
NCBP1	-0,3883
DKC1	-0,3833
NUCKS1	-0,3816
EML4	-0,3755
PHIP	-0,3752
HSD17B11	-0,3719
MED12	-0,3701
MEPCE	-0,3660

NOA1	-0,3649	**EXOSC6**	-0,2907	**GOT1**	-0,2134
EIF4H	-0,3605	**HNRNPA3**	-0,2883	**HMGXB4**	-0,2092
HNRNPUL2	-0,3598	**NCAPG**	-0,2881	**ERO1L**	-0,2086
GPHN	-0,3579	**ZFP91**	-0,2878	**HUWE1**	-0,2063
NPM1	-0,3549	**CEP41**	-0,2876	**ADRM1**	-0,2052
PSME2	-0,3544	**ARHGAP35**	-0,2866	**SLK**	-0,2051
FXR1	-0,3542	**UFSP2**	-0,2853	**ANP32E**	-0,2049
AP2S1	-0,3534	**PRPF6**	-0,2822	**CSDE1**	-0,2044
HMGB1	-0,3521	**CPSF3**	-0,2797	**UGDH**	-0,2040
RELA	-0,3521	**PELP1**	-0,2792	**HNRNPA1;HNRNPA1L2**	-0,2035
MYO18A	-0,3464	**H2AFY2**	-0,2790	**ATP2B1**	-0,2017
SEC63	-0,3450	**CUL1**	-0,2766	**TOE1**	-0,2001
KIAA0101	-0,3441	**NIFK**	-0,2766	**MDC1**	-0,1996
SND1	-0,3409	**STOML2**	-0,2733	**MFAP1**	-0,1993
GTF2I	-0,3407	**RRP9**	-0,2697	**CSE1L**	-0,1989
TM9SF2	-0,3403	**CPSF1**	-0,2687	**IMPDH2**	-0,1975
UHRF1	-0,3387	**APOB**	-0,2678	**EIF3C;EIF3CL**	-0,1944
TUFM	-0,3383	**RETSAT**	-0,2675	**APEX1**	-0,1939
ALDH2	-0,3377	**WAC**	-0,2656	**PDHB**	-0,1895
SNRNP40	-0,3366	**CDK12**	-0,2651	**SMC1A**	-0,1893
UBAC2	-0,3366	**SMC3**	-0,2650	**CGN**	-0,1865
WDFY1	-0,3362	**CBR1**	-0,2643	**PAWR**	-0,1855
THOC2	-0,3315	**MED24**	-0,2635	**LRSAM1**	-0,1840
HMGB2	-0,3309	**GSR**	-0,2631	**EEF1G**	-0,1808
ACSL4	-0,3298	**CCDC94**	-0,2600	**RFC5**	-0,1808
BCAM	-0,3294	**PUS7**	-0,2588	**XRCC5**	-0,1794
CDK6	-0,3271	**SERPINB1**	-0,2581	**NOP58**	-0,1761
NUP155	-0,3258	**EPB41L2**	-0,2570	**RBM25**	-0,1759
HELLS	-0,3255	**RIC8A**	-0,2550	**SEC23A**	-0,1748
CHD4	-0,3251	**GFPT1**	-0,2512	**ACY1**	-0,1718
CLU	-0,3249	**EEF1B2**	-0,2478	**ZFR**	-0,1708
CHAF1A	-0,3229	**PLOD1**	-0,2472	**HNRNPA2B1**	-0,1696
IDH1	-0,3222	**FKBP15**	-0,2465	**MCCC2**	-0,1673
CAD	-0,3210	**EIF4G1**	-0,2464	**PCYOX1**	-0,1659
WDR61	-0,3207	**XPO7**	-0,2454	**GUF1**	-0,1648
HNRNPLL	-0,3150	**FAH**	-0,2453	**EFTUD2**	-0,1628
TCF20	-0,3142	**MGST3**	-0,2445	**IQGAP2**	-0,1613
MCM4	-0,3098	**SART3**	-0,2433	**ARHGDIA**	-0,1609
TMEM43	-0,3094	**MTDH**	-0,2373	**HNRNPM**	-0,1578
TXNDC5	-0,3031	**PTPRK;PTPRM**	-0,2371	**CORO7**	-0,1572
COX15	-0,3030	**PEX19**	-0,2367	**LTA4H**	-0,1545
MRPL37	-0,3027	**CCAR1**	-0,2308	**CCAR2**	-0,1519
KPNB1	-0,3022	**PDIA4**	-0,2298	**FAM134C**	-0,1513
OGFR	-0,3018	**TUBG1**	-0,2291	**XAB2**	-0,1469
APP	-0,3016	**ILF3**	-0,2286	**SPTBN1**	-0,1467
NUP88	-0,3005	**XRCC6**	-0,2281	**HSPB1**	-0,1463
HADHB	-0,2986	**AIP**	-0,2269	**SMC4**	-0,1458
FMR1	-0,2984	**CMTR1**	-0,2236	**IGF2BP1**	-0,1455
MCM6	-0,2974	**EIF4A3**	-0,2222	**PHF14**	-0,1411
MSH6	-0,2969	**GTF2F1**	-0,2220	**PSMD2**	-0,1384
TLN2	-0,2957	**HTT**	-0,2215	**EPPK1**	-0,1375
ABCF1	-0,2956	**TP53BP1**	-0,2203	**PC**	-0,1370
TNPO1	-0,2946	**PSMD11**	-0,2202	**NES**	-0,1347
RRP8	-0,2935	**RCN2**	-0,2200	**MCM2**	-0,1326
TXNL1	-0,2933	**PLAA**	-0,2195	**EIF5B**	-0,1295
LDHA	-0,2917	**GCFC2**	-0,2138	**AGPS**	-0,1288
PDS5B	-0,2908	**PMPCA**	-0,2135	**LRPPRC**	-0,1285

PFKL	-0,1256
EEF1D	-0,1250
DYNLT1	-0,1246
LETM1	-0,1235
LMNB1	-0,1128
HADHA	-0,1080
GCN1L1	-0,1059
EIF3I	-0,1052
PRPF8	-0,0994
CLTC	-0,0863
SPTAN1	-0,0814
SDC2	0,0523
LAMB1	0,0751
GDI2	0,0824
UBAP2L	0,0869
RPL4	0,1019
KIAA1211	0,1044
FLNA	0,1060
TPX2	0,1249
EGFR	0,1325
IDH2	0,1366
GLIPR2	0,1392
ACLY	0,1399
MACF1	0,1437
CKAP5	0,1491
IK	0,1536
HBS1L	0,1605
GTF2H1	0,1630
QPRT	0,1660
ANXA2;ANXA2P2	0,1661
DSP	0,1692
SRSF3	0,1735
TPM4	0,1755
MDH1	0,1783
TRA2B	0,1804
PDLIM7	0,1823
KIF5B	0,1843
CCT8	0,1884
AP2A1	0,1890
RSL1D1	0,1905
TFIP11	0,1935
PACSIN2	0,1970
LAMC1	0,2012
TNKS1BP1	0,2123
PDCD6IP	0,2187
IGF2BP3	0,2214
DDX5	0,2218
RTKN	0,2224
RFX1	0,2300
ATXN10	0,2313
PSMD4	0,2335
RRM1	0,2399
CLASP2	0,2404
APOA1BP	0,2410
RUVBL2	0,2442
KPNA2	0,2497
TACC3	0,2535
FGD4	0,2624
GLCCI1	0,2694
RBPMS	0,2803
TCEB1	0,2878
EPB41L5	0,2891
EPS8L2	0,2941
CLNS1A	0,2948
MYO1C	0,2972
SPATS2	0,2990
ACAT2	0,3017
MARS	0,3039
STBD1	0,3059
NDUFS1	0,3063
EXOC1	0,3075
FAM49B	0,3087
ARID3A	0,3143
CRIP2	0,3174
VIM	0,3198
AHR	0,3233
VCL	0,3233
PICALM	0,3240
ZNF281	0,3268
CPNE3	0,3294
EPCAM	0,3361
METAP2	0,3370
YAP1	0,3430
CSRP1	0,3447
TUBGCP2	0,3458
DPY30	0,3480
CCT3	0,3480
PPL	0,3506
GSTM3	0,3526
SPINT1	0,3568
SMTN	0,3618
COPZ1	0,3741
PALLD	0,3824
CKB	0,3885
GALNT1	0,3909
DNM1L	0,3910
SNAP23	0,4009
IBA57	0,4058
ANLN	0,4101
TIMM13	0,4287
AAK1	0,4318
HSD17B10	0,4343
SULT1C4	0,4368
TCEA1	0,4405
MAP4	0,4424
DYNLRB1	0,4546
ENAH	0,4628
KIF21A	0,4647
ADAM9	0,4851
BAG3	0,5057
JAG1	0,5236
SLAIN2	0,5441
CPNE8	0,5646
SCP2	0,5669
PKP2	0,5709
FSCN1	0,5721
GPC4	0,5991
DOHH	0,6050
NCKIPSD	0,6122
PRPF3	0,6175
DCUN1D5	0,6281
TBC1D22A	0,6687
ATG3	0,6865
ECI2	0,6990
FLNC	0,7077
CNN2	0,7278
FILIP1L	0,7356
RPL11	0,7660
ADPRHL2	0,8527
OCIAD1	0,9019
ASPSCR1	1,1298
ITGB4	1,1605
SPECC1L	1,2044
PGAM5	1,2593
TCF12	1,2695
YARS2	1,3199
TOM1L1	1,3362
CLIP1	1,3538
MSI1	1,5163
RBBP6	1,5250
SACM1L	1,5401
EXOSC4	1,7643
DCK	1,8091
RAP1A	1,9592
IPO8	2,1905
EPHB4;EPHB3	2,4290
ARPC5L	2,6051
VBP1	2,7937
XPOT	2,8904
ACP1	3,5633
TMF1	3,7310
RAB6A;RAB6B;RAB39A	4,9142

Table 5: List of proteins with statistically significant (two-sample t-test, two sided, without multi-testing correction, S_0 = 0.01, p < 0.05) changes in expression LX-2 PNPLA3 I148M vs wt. FC = fold change.

GENE NAMES	LOG2 FC LX-2 PNPLA3 I148M-
PGRMC2	-2,6229
NDUFA4	-2,3918
TUBA4A	-1,9852
RPF2	-1,9439
HEG1	-1,7639
CMAS	-1,6517
FBLN2	-1,5817
TIMM8A	-1,5714
HUS1	-1,4043
CD81	-1,3163
GHDC	-1,2673
TFPI2	-1,2525
JAGN1	-1,2253
CHST14	-1,2189
NPTN	-1,1939
FHL2	-1,1155
POLR2I	-1,0687
CDC20	-1,0166
C9ORF142	-0,9847
NDUFA11	-0,9576
NGLY1	-0,9575
CIAO1	-0,9497
OXA1L	-0,9104
HSPG2	-0,8255
C11ORF54	-0,8230
ACTB	-0,7983
RPS27A;UBA52;UBB;UB	-0,7545
POLA2	-0,7493
PGK2	-0,7312
DYNLL2	-0,6840
MDK	-0,6795
TIMP3	-0,6789
CDKAL1	-0,6657
NUBP1	-0,6595
RUNX1	-0,6350
CBR3	-0,6182
SNRPD2	-0,6136
DHCR7	-0,6038
ETFB	-0,6023
DDI2	-0,5966
CHCHD5	-0,5930
RPL18A	-0,5876
SEC24D	-0,5732
NUTF2	-0,5727
NFU1	-0,5637
C15ORF52	-0,5628
MRPS17	-0,5485
ATOX1	-0,5479
RPL12	-0,5325
ZMIZ2	-0,5320
ITGA6	-0,5213
RPS12	-0,5207
HSPBP1	-0,5189
GNB2	-0,5180
SEC13	-0,5139
RNH1	-0,5075
PSMD9	-0,5005
ISCU	-0,4979
SNRPD3	-0,4942
L3HYPDH	-0,4857
ZFAND5	-0,4763
LGALS1	-0,4553
PRPS1	-0,4455
TBCC	-0,4435
RPL30	-0,4406
NR2C2AP	-0,4358
CLIC1	-0,4322
PBK	-0,4224
CYR61	-0,4169
USP10	-0,4123
THBS1	-0,4079
DYNLL1	-0,4018
NOC2L	-0,4004
YIPF5	-0,3962
FECH	-0,3921
RABGAP1L	-0,3883
RSBN1L	-0,3867
IFITM1;IFITM2;IFITM3	-0,3849
GPC1	-0,3676
NECAP2	-0,3659
GLRX5	-0,3652
RBM42	-0,3627
RPLP1	-0,3484
NUP37	-0,3447
CXCL12	-0,3434
UBE2M	-0,3424
DSTN	-0,3406
CHORDC1	-0,3392
GNB1	-0,3387
EIF2B5	-0,3362
ANXA7	-0,3259
FAM3C	-0,3193
CCDC91	-0,3188
RPS11	-0,3186
NEK7	-0,3171
EXOSC4	-0,2977
PVRL2	-0,2957
GOT2	-0,2925
C2ORF47	-0,2892
RFTN1	-0,2774
PPP1CB	-0,2757
RRP7A	-0,2744
MTPN	-0,2665
NDUFV2	-0,2643
AHCYL1	-0,2625
PWP2	-0,2610
MEA1	-0,2607
MOB4	-0,2554
SORT1	-0,2452
VCL	-0,2450
TMEM120A	-0,2403
ATP6V1G1;ATP6V1G2	-0,2386
GNG12	-0,2355
GSTM4;GSTM1	-0,2345
MOB1A;MOB1B	-0,2337
RAB18	-0,2308
UBE2G1	-0,2251
CISD2	-0,2228
RND3	-0,2202
NGDN	-0,2166
SF3A2	-0,2125
EIF5A;EIF5AL1	-0,2089
RAP1A	-0,2087
HPRT1	-0,2073
ERH	-0,1992
MANF	-0,1982
SMAD3	-0,1956
MYADM	-0,1937
HAT1	-0,1885
CBX5	-0,1880
NUP98	-0,1867
PIK3R1	-0,1825
CAPZB	-0,1812
CLTB	-0,1810
ACOX1	-0,1787
JUN	-0,1772
UBL4A	-0,1762
AAMP	-0,1740
FIS1	-0,1711
NUDCD2	-0,1711
NIPA1	-0,1658
PDCD5	-0,1647
EIF2B3	-0,1632
ECHS1	-0,1592
NCKAP1	-0,1575
BRI3BP	-0,1553
PAICS	-0,1518
BAG3	-0,1511
FBLIM1	-0,1489
HSD17B7	-0,1480
PAIP1	-0,1476
CAMK2D	-0,1469
TCEA1	-0,1469
PNPT1	-0,1468
GTF3C1	-0,1464

HNRNPH2	-0,1462	**LMNB2**	0,0664	**LONP1**	0,1366
ASCC3	-0,1398	**HNRNPC**	0,0746	**AVEN**	0,1393
RDH11	-0,1383	**IQGAP1**	0,0767	**CLTC**	0,1394
HGS	-0,1376	**MCM3**	0,0774	**CDC42EP3**	0,1400
KIF23	-0,1369	**HNRNPK**	0,0775	**MED12**	0,1425
ARPC5	-0,1362	**DHX9**	0,0830	**BUB1**	0,1433
POLDIP2	-0,1328	**ESYT1**	0,0842	**CTPS1**	0,1435
APOA1BP	-0,1326	**PSMC1**	0,0852	**PGM3**	0,1439
NQO2	-0,1287	**PARK7**	0,0864	**ECE1**	0,1458
CCT4	-0,1265	**HSP90AA1**	0,0899	**ATXN2**	0,1467
SNRPF	-0,1264	**GBF1**	0,0912	**DIAPH1**	0,1467
NDUFS6	-0,1258	**SND1**	0,0934	**CUL4B**	0,1486
STT3B	-0,1239	**RNPS1**	0,0935	**DPP3**	0,1490
TRIOBP	-0,1237	**PPP1CA**	0,0935	**SKIV2L2**	0,1490
HM13	-0,1159	**PSMD13**	0,0948	**RPS7**	0,1496
RAC1	-0,1154	**SRSF4**	0,0948	**MYBBP1A**	0,1518
CSDE1	-0,1154	**IMPDH2**	0,0960	**DDX18**	0,1540
PSMD4	-0,1120	**EZR**	0,0974	**BPTF**	0,1542
EPN1	-0,1106	**KRT18**	0,0989	**TAMM41**	0,1548
ST13;ST13P4;ST13P5	-0,1091	**LARP7**	0,0994	**FAF2**	0,1551
XPO7	-0,1078	**SNRNP200**	0,1001	**EIF5B**	0,1567
RRM2	-0,1078	**BAG5**	0,1009	**GSTK1**	0,1575
TUBGCP2	-0,1032	**TBL2**	0,1013	**AHSA1**	0,1589
STMN1	-0,1030	**ACOT7**	0,1022	**PTPRF**	0,1607
SH3GL1	-0,1021	**HDLBP**	0,1044	**AQR**	0,1612
CEP170	-0,1021	**GBE1**	0,1048	**UQCRC1**	0,1616
EHD4	-0,1000	**CENPV**	0,1060	**ATL3**	0,1616
LSM5	-0,0970	**PEBP1**	0,1066	**LDHB**	0,1624
CLASP1	-0,0965	**SSB**	0,1069	**WIZ**	0,1640
IKBKAP	-0,0931	**PDLIM7**	0,1070	**NPM1**	0,1662
CLUH	-0,0930	**EFTUD2**	0,1100	**NOC3L**	0,1672
CD44	-0,0927	**P4HB**	0,1108	**ARPC2**	0,1696
ATXN2L	-0,0923	**USP5**	0,1129	**PARP1**	0,1702
STIP1	-0,0891	**RRP9**	0,1142	**DDX54**	0,1702
RARS	-0,0888	**RBM10**	0,1159	**PDIA6**	0,1703
ACTR3	-0,0882	**SARS**	0,1183	**ATP5B**	0,1710
NSUN2	-0,0877	**VARS**	0,1203	**CPSF1**	0,1721
CDK5RAP3	-0,0870	**ALYREF**	0,1206	**COG1**	0,1726
HSPA4	-0,0863	**AP3B1**	0,1208	**DDB1**	0,1728
TCEB1	-0,0850	**OLA1**	0,1215	**SUB1**	0,1763
SYNPO	-0,0829	**EXOC4**	0,1218	**PRPF8**	0,1764
RUVBL1	-0,0825	**RAB8A**	0,1230	**COMMD10**	0,1765
SNX4	-0,0785	**DNAJC8**	0,1249	**PTRH2**	0,1781
SEC24C	-0,0754	**ACLY**	0,1266	**POLR2C**	0,1789
SKA1	-0,0711	**NAT10**	0,1271	**AP2B1**	0,1799
PLEKHA5	-0,0695	**RRAS**	0,1272	**FIP1L1**	0,1806
HSPA9	-0,0693	**SRPR**	0,1274	**PSMA2**	0,1809
MYO1E	-0,0690	**RAB22A**	0,1286	**GTPBP1**	0,1814
TOR1AIP1	-0,0640	**HNRNPLL**	0,1297	**GSTM2**	0,1819
PRKDC	-0,0596	**BAZ1B**	0,1305	**ENDOD1**	0,1820
YWHAZ	-0,0559	**SEC31A**	0,1308	**SERPINB1**	0,1820
RSL1D1	-0,0499	**ERCC6L**	0,1310	**EXOC1**	0,1845
HNRNPH1	-0,0486	**PGAM1**	0,1313	**ATP6V1A**	0,1852
SUGP2	-0,0466	**MDH1**	0,1344	**API5**	0,1859
ILF3	0,0533	**FAM129B**	0,1347	**ANKRD40**	0,1859
DPYSL2	0,0536	**CCDC132**	0,1351	**SMCHD1**	0,1864
PNN	0,0554	**PPIL2**	0,1365	**HOMER3**	0,1876

NNT	0,1876
SRP54	0,1913
CPSF2	0,1926
ENO2	0,1930
GFPT1	0,1934
MICALL1	0,1947
SPC25	0,1959
CDH2	0,1971
RABGEF1	0,1990
PLCB3	0,1998
MRE11A	0,2022
COPS8	0,2075
CALU	0,2076
LSM4	0,2078
S100A16	0,2085
DAG1	0,2122
HNRNPA2B1	0,2126
RPN1	0,2128
WDR61	0,2131
STXBP2	0,2141
CS	0,2154
NIPSNAP3A	0,2165
OGDH	0,2165
NAMPT	0,2166
ARFIP1	0,2184
TIAL1	0,2215
GXYLT1	0,2222
GLRX3	0,2230
CCT5	0,2248
LDHA	0,2266
SWAP70	0,2296
GANAB	0,2299
TXNL1	0,2303
COPS5	0,2308
USP7	0,2334
C17ORF75	0,2340
YES1	0,2341
DDOST	0,2346
OAT	0,2348
GRSF1	0,2350
HNRNPA1;HNRNPA1L2	0,2355
ARHGEF28	0,2357
CARHSP1	0,2373
TAX1BP3	0,2377
XRCC5	0,2396
ADRBK1	0,2396
ABHD12	0,2422
PRPSAP2	0,2439
HNRNPA0	0,2449
PAIP2	0,2477
SAP30BP	0,2492
ARIH2	0,2499
FAF1	0,2542
HMGXB4	0,2543
NT5C	0,2573
HNRNPAB	0,2594
PSMB2	0,2617
PPP2R3A	0,2617
SNRNP40	0,2621
HNRNPA3	0,2625
THOC6	0,2652
EMG1	0,2666
LARP1	0,2672
ECHDC1	0,2681
FLOT2	0,2686
ARHGEF11	0,2716
PSMD8	0,2723
NAA25	0,2753
CSNK2A1;CSNK2A3	0,2753
UBQLN4	0,2754
FAM210A	0,2764
UBE2H	0,2774
ACOT8	0,2813
CWC27	0,2826
REXO2	0,2837
SMARCD2	0,2847
ARL3	0,2851
RPS15	0,2853
ALG2	0,2897
RALA	0,2922
PIP4K2C	0,2926
LMAN1	0,2962
PPP4R1	0,2962
DDX1	0,2983
GCDH	0,2998
SUN2	0,3018
MTHFD1L	0,3024
ORC3	0,3037
ISOC1	0,3048
KIF13A	0,3074
RCN1	0,3134
PRIM2	0,3141
RAB31	0,3177
ACTR1A	0,3189
SEL1L	0,3238
IFIT5	0,3240
ZNF148	0,3243
GIGYF1	0,3267
ITGB1	0,3275
ACADM	0,3292
ARHGAP1	0,3306
BTF3	0,3311
MAPK14	0,3325
FGFR1OP	0,3375
HIBADH	0,3382
ARL1	0,3387
GTF2E2	0,3428
ORC2	0,3519
SF1	0,3540
RPS15A	0,3563
ASNA1	0,3574
GMDS	0,3574
PSME2	0,3597
MCTS1	0,3609
SCPEP1	0,3625
TRIP10	0,3647
MGME1	0,3672
SMARCAD1	0,3673
TMX3	0,3712
MTR	0,3715
FADD	0,3743
MAP1S	0,3759
EHD2	0,3769
SNRPE	0,3814
RBM3	0,3836
TIGAR	0,3932
COASY	0,3949
NRBP1	0,3951
KRAS	0,3976
MYEOV2	0,4001
TUBG1;TUBG2	0,4100
SRSF10	0,4133
ABAT	0,4143
HARS2	0,4153
FAM91A1	0,4196
PXK	0,4198
VWA8	0,4203
COL5A1	0,4222
CARS2	0,4241
CCDC94	0,4289
SKP2	0,4292
BID	0,4302
NOM1	0,4353
BRIX1	0,4355
STRIP1	0,4364
PFAS	0,4374
SCCPDH	0,4376
TEX10	0,4448
RPA3	0,4455
CENPP	0,4507
YKT6	0,4523
GSKIP	0,4524
SAP18	0,4634
YEATS4	0,4635
LDLRAP1	0,4676
MSH3	0,4729
USP48	0,4766
WDR26	0,4775
ZC3H7B	0,4794
HSD17B11	0,4846
CPA4	0,4848
PEF1	0,4921
NMD3	0,4941
TTI1	0,4955
CCNH	0,4962
NOC4L	0,4968
GCLC	0,4986
VWA9	0,5048
HINT1	0,5063
MEST	0,5072
RBM22	0,5075

MGST3	0,5096
GSTT2B;GSTT2	0,5103
RPL38	0,5112
BCCIP	0,5265
PMPCA	0,5316
PUS1	0,5347
DDX24	0,5437
WBP2	0,5452
EHD3	0,5489
MORF4L1	0,5574
RAB4B	0,5673
SCLY	0,5738
SIPA1L3	0,5783
GBA	0,5820
DNAJC17	0,5930
PHC2	0,5938
RPP40	0,5972
ARF5	0,6084
RAVER1	0,6103
SRC	0,6245
GOLPH3	0,6254
ARF1;ARF3	0,6264
AKT2	0,6301
ABHD11	0,6320
TMX2	0,6320
POLR2E	0,6333
ATP6V1F	0,6351
MAPKAPK2	0,6353
PDGFRB	0,6403
PBXIP1	0,6404
DHCR24	0,6425
PPIH	0,6438
RBM15	0,6481
STK39	0,6671
MKLN1	0,6682
CNOT2	0,6798
CRCP	0,6851
MOGS	0,6906
SUPT7L	0,6959
MED21	0,7001
TRIM56	0,7025
FBXO44	0,7065
HMGCL	0,7295
POLE	0,7307
HDAC6	0,7342
INTS3	0,7401
RILPL2	0,7420
DNAJC11	0,7531
CACNA2D1	0,7549
C9ORF114	0,7634
HMG20A	0,7649
HOOK2	0,7747
MB21D2	0,7864
NDUFB5	0,7889
TMX4	0,8027
LSM14A	0,8091
CCDC82	0,8097
ACOT1;ACOT2	0,8282
FLAD1	0,8284
STYX	0,8300
MDP1	0,8508
AASS	0,8525
MRPL28	0,8637
HSP90AB2P	0,8643
PHACTR2	0,8676
CTNNAL1	0,8692
SLC4A2	0,8782
DOLPP1	0,8851
ELOVL2	0,8868
S100A6	0,8882
VPS18	0,8884
CCNK	0,8891
SEC11A	0,9014
CNRIP1	0,9180
RBM5	0,9291
LRSAM1	0,9603
TMED7	0,9757
PIP4K2A	0,9923
ARHGEF40	1,0010
SDHAF2	1,0151
PYCARD	1,0160
STAT6	1,0170
FLI1	1,0238
ANAPC4	1,0333
TOR1AIP2	1,0439
CYP20A1	1,0500
C16ORF62	1,0535
ISOC2	1,0544
RBM7	1,0563
TIMM17A	1,0637
ARAF	1,0680
TRIM26	1,0745
PRKACB	1,1008
TMOD2	1,1211
MRPL23	1,1348
FAM213B	1,1439
TMEM14C	1,1639
NAGA	1,1929
LLPH	1,2099
MRPL10	1,2158
MRPL21	1,2211
FNTB	1,2456
PARP2	1,2770
RAD9A	1,3036
BPHL	1,3164
MKRN2	1,3245
LMF2	1,3641
TXNL4A	1,3808
CENPK	1,3979
SAC3D1	1,4021
EMC3	1,4032
MGAT1	1,4131
CFAP36	1,4322
CENPU	1,4793
NDNL2	1,5772
PIGT	1,5893
RRAGC;RRAGD	1,5971
ZNF207	1,6131
MPC2	1,7211
MRPL50	1,7383
GLUL	1,7955
CDK7	2,0075
LEO1	2,0783
CDC42SE2	2,0973
PSEN1;PSEN2	2,1246
WDR77	2,1983
HIGD1A	2,2523
LSM7	2,2805
ROMO1	2,3214
LPHN2;LPHN1	2,3510
ZSWIM8	3,3383
RYR2	4,9649

Table 6: List of all enriched GO terms (STRING analysis) "biological processes" Hep3B CGI-58 KD vs control using only proteins with a p-value of < 0.05 (two-sidedT t-test without FDR correction, S_0 = 0.1) for analysis. FDR cut-off value 0.1.

#TERM ID	TERM DESCRIPTION GO BIOLOGICAL PROCESSES HEP3B CGI-58 KD-C	OBSERVED GENE COUNT	BACKGROUND GENE COUNT	STRENGTH	FALSE DISCOVERY RATE
GO:0034641	Cellular nitrogen compound metabolic process	196	3282	0.39	8.39e-31
GO:0006139	Nucleobase-containing compound metabolic process	167	2659	0.41	2.21e-27
GO:0046483	Heterocycle metabolic process	173	2840	0.4	2.50e-27
GO:0044237	Cellular metabolic process	309	7513	0.23	6.97e-27
GO:0006807	Nitrogen compound metabolic process	291	6852	0.24	1.67e-26
GO:0006725	Cellular aromatic compound metabolic process	172	2882	0.39	2.05e-26
GO:0044238	Primary metabolic process	303	7332	0.23	2.05e-26
GO:1901360	Organic cyclic compound metabolic process	179	3118	0.37	5.86e-26
GO:0071704	Organic substance metabolic process	311	7755	0.22	2.07e-25
GO:0090304	Nucleic acid metabolic process	142	2178	0.43	2.56e-24
GO:0008152	Metabolic process	321	8298	0.2	4.89e-24
GO:0009987	Cellular process	452	15024	0.09	9.54e-23
GO:0043170	Macromolecule metabolic process	262	6137	0.24	1.24e-22
GO:0010467	Gene expression	133	2056	0.42	3.13e-22
GO:0016071	mRNA metabolic process	66	678	0.6	1.53e-17
GO:0071840	Cellular component organization or biogenesis	235	5633	0.23	1.53e-17
GO:0016070	RNA metabolic process	105	1584	0.43	2.06e-17
GO:0016043	Cellular component organization	225	5447	0.23	7.16e-16
GO:0051641	Cellular localization	150	2967	0.32	9.80e-16
GO:0006396	RNA processing	71	854	0.53	1.19e-15
GO:0051649	Establishment of localization in cell	128	2375	0.34	6.76e-15
GO:0044260	Cellular macromolecule metabolic process	207	4976	0.23	2.57e-14
GO:0006397	mRNA processing	49	468	0.63	9.08e-14
GO:0008380	RNA splicing	44	396	0.66	4.74e-13
GO:0044085	Cellular component biogenesis	130	2583	0.31	5.54e-13
GO:0000398	mRNA splicing, via spliceosome	38	294	0.72	5.56e-13
GO:0006996	Organelle organization	157	3450	0.27	8.58e-13
GO:0043933	Protein-containing complex subunit organization	89	1539	0.37	3.66e-11
GO:0033036	Macromolecule localization	121	2473	0.3	4.46e-11
GO:0065003	Protein-containing complex assembly	79	1293	0.4	7.77e-11
GO:0010608	Posttranscriptional regulation of gene expression	49	574	0.54	8.92e-11
GO:0022607	Cellular component assembly	116	2359	0.3	1.15e-10
GO:0045184	Establishment of protein localization	88	1564	0.36	1.92e-10
GO:0008104	Protein localization	107	2139	0.31	4.39e-10
GO:0015031	Protein transport	84	1486	0.36	5.44e-10
GO:0044271	Cellular nitrogen compound biosynthetic process	85	1522	0.36	7.01e-10
GO:0034613	Cellular protein localization	88	1610	0.35	7.83e-10
GO:1901576	Organic substance biosynthetic process	124	2734	0.27	2.42e-09
GO:0022613	Ribonucleoprotein complex biogenesis	39	423	0.58	2.59e-09
GO:0009058	Biosynthetic process	125	2788	0.26	3.90e-09
GO:0046907	Intracellular transport	82	1520	0.34	8.13e-09
GO:0034622	Cellular protein-containing complex assembly	55	816	0.44	1.23e-08
GO:0071705	Nitrogen compound transport	92	1823	0.32	1.23e-08
GO:0006886	Intracellular protein transport	62	999	0.4	1.56e-08
GO:0006403	RNA localization	26	210	0.7	2.39e-08

GO:0071826	Ribonucleoprotein complex subunit organization	25	193	0.72	2.39e-08
GO:1903311	Regulation of mRNA metabolic process	33	338	0.6	2.39e-08
GO:0051179	Localization	203	5591	0.17	2.67e-08
GO:0009059	Macromolecule biosynthetic process	84	1643	0.32	4.94e-08
GO:0044249	Cellular biosynthetic process	115	2611	0.26	8.00e-08
GO:0051169	Nuclear transport	28	266	0.63	1.26e-07
GO:0016032	Viral process	51	776	0.43	1.27e-07
GO:0034645	Cellular macromolecule biosynthetic process	81	1592	0.32	1.29e-07
GO:0034248	Regulation of cellular amide metabolic process	37	456	0.52	1.84e-07
GO:0022618	Ribonucleoprotein complex assembly	23	186	0.7	2.57e-07
GO:0006417	Regulation of translation	34	398	0.54	2.61e-07
GO:1901575	Organic substance catabolic process	85	1750	0.3	3.58e-07
GO:0006913	Nucleocytoplasmic transport	27	263	0.62	3.75e-07
GO:0051234	Establishment of localization	167	4479	0.18	5.19e-07
GO:0043299	Leukocyte degranulation	38	506	0.49	7.24e-07
GO:0043312	Neutrophil degranulation	37	484	0.5	7.41e-07
GO:0006259	DNA metabolic process	48	750	0.42	8.04e-07
GO:0002274	Myeloid leukocyte activation	41	585	0.46	1.04e-06
GO:0002444	Myeloid leukocyte mediated immunity	38	516	0.48	1.10e-06
GO:0006810	Transport	162	4353	0.18	1.10e-06
GO:0044403	Symbiotic process	52	865	0.39	1.19e-06
GO:0050658	RNA transport	22	189	0.68	1.30e-06
GO:0002275	Myeloid cell activation involved in immune response	38	522	0.47	1.34e-06
GO:0018130	Heterocycle biosynthetic process	59	1061	0.36	1.48e-06
GO:0048522	Positive regulation of cellular process	195	5579	0.16	1.48e-06
GO:0000278	Mitotic cell cycle	45	695	0.42	1.49e-06
GO:0009056	Catabolic process	92	2042	0.27	1.80e-06
GO:0007010	Cytoskeleton organization	61	1126	0.35	1.88e-06
GO:0009057	Macromolecule catabolic process	58	1058	0.35	2.98e-06
GO:0002443	Leukocyte mediated immunity	42	641	0.43	3.33e-06
GO:0006281	DNA repair	37	522	0.46	3.61e-06
GO:0006412	Translation	30	366	0.53	4.12e-06
GO:0045055	Regulated exocytosis	44	697	0.41	4.12e-06
GO:1901362	Organic cyclic compound biosynthetic process	63	1211	0.33	4.15e-06
GO:0002263	Cell activation involved in immune response	41	630	0.43	5.56e-06
GO:0033554	Cellular response to stress	80	1725	0.28	5.57e-06
GO:0071702	Organic substance transport	94	2173	0.25	7.11e-06
GO:0051128	Regulation of cellular component organization	101	2402	0.24	7.66e-06
GO:0016192	Vesicle-mediated transport	82	1805	0.27	8.34e-06
GO:0019438	Aromatic compound biosynthetic process	57	1070	0.34	8.97e-06
GO:1901564	Organonitrogen compound metabolic process	182	5244	0.15	9.87e-06
GO:0034654	Nucleobase-containing compound biosynthetic process	54	995	0.35	1.13e-05
GO:0044248	Cellular catabolic process	80	1758	0.27	1.13e-05
GO:0002252	Immune effector process	53	969	0.35	1.16e-05
GO:0002366	Leukocyte activation involved in immune response	40	626	0.42	1.16e-05
GO:0006518	Peptide metabolic process	35	503	0.45	1.16e-05
GO:0051028	mRNA transport	18	148	0.7	1.21e-05
GO:0009894	Regulation of catabolic process	55	1038	0.34	1.68e-05
GO:0031123	RNA 3-end processing	17	135	0.71	1.69e-05
GO:0031329	Regulation of cellular catabolic process	49	875	0.36	1.79e-05
GO:0043487	Regulation of RNA stability	20	192	0.63	2.28e-05
GO:0048518	Positive regulation of biological process	203	6112	0.13	2.58e-05
GO:0072594	Establishment of protein localization to organelle	31	433	0.47	3.28e-05
GO:0006887	Exocytosis	45	789	0.37	3.50e-05
GO:0048024	Regulation of mRNA splicing, via spliceosome	15	110	0.75	3.50e-05
GO:0051130	Positive regulation of cellular component organization	60	1209	0.31	3.50e-05
GO:0051168	Nuclear export	18	162	0.66	3.72e-05

GO:0033365	Protein localization to organelle	43	743	0.37	4.41e-05
GO:1903047	Mitotic cell cycle process	38	616	0.4	4.95e-05
GO:0006611	Protein export from nucleus	17	150	0.67	5.97e-05
GO:0043484	Regulation of RNA splicing	17	152	0.66	7.01e-05
GO:0032940	Secretion by cell	51	979	0.33	7.08e-05
GO:0006974	Cellular response to DNA damage stimulus	44	793	0.36	9.00e-05
GO:0006457	Protein folding	20	213	0.58	9.15e-05
GO:0065007	Biological regulation	348	12171	0.07	9.15e-05
GO:0007049	Cell cycle	62	1313	0.29	9.82e-05
GO:0043604	Amide biosynthetic process	33	512	0.42	0.00011
GO:0050794	Regulation of cellular process	319	10932	0.08	0.00011
GO:0019222	Regulation of metabolic process	221	6948	0.11	0.00012
GO:0140352	Export from cell	52	1028	0.32	0.00012
GO:0034660	ncRNA metabolic process	31	467	0.43	0.00013
GO:0044270	Cellular nitrogen compound catabolic process	29	422	0.45	0.00015
GO:0043488	Regulation of mRNA stability	18	183	0.6	0.00016
GO:0001775	Cell activation	53	1075	0.3	0.00019
GO:0061013	Regulation of mRNA catabolic process	19	205	0.58	0.00019
GO:0006405	RNA export from nucleus	15	131	0.67	0.00021
GO:0050684	Regulation of mRNA processing	16	149	0.64	0.00021
GO:0050789	Regulation of biological process	330	11475	0.07	0.00022
GO:0065008	Regulation of biological quality	142	4042	0.16	0.00024
GO:1905214	Regulation of RNA binding	6	12	1.31	0.00024
GO:0060255	Regulation of macromolecule metabolic process	205	6407	0.12	0.00028
GO:0051170	Import into nucleus	14	118	0.69	0.00031
GO:0045321	Leukocyte activation	47	929	0.32	0.00036
GO:0034655	Nucleobase-containing compound catabolic process	26	373	0.46	0.00037
GO:0000381	Regulation of alternative mRNA splicing, via spliceo-	11	73	0.79	0.00044
GO:0044087	Regulation of cellular component biogenesis	48	971	0.31	0.00050
GO:0043603	Cellular amide metabolic process	41	773	0.34	0.00052
GO:0031323	Regulation of cellular metabolic process	199	6239	0.12	0.00054
GO:0071426	Ribonucleoprotein complex export from nucleus	14	125	0.66	0.00054
GO:0046903	Secretion	52	1097	0.29	0.00060
GO:0030029	Actin filament-based process	34	592	0.37	0.00067
GO:0044267	Cellular protein metabolic process	130	3696	0.16	0.00067
GO:0080090	Regulation of primary metabolic process	193	6032	0.12	0.00067
GO:1902850	Microtubule cytoskeleton organization involved in mito-	13	112	0.68	0.00078
GO:0032392	DNA geometric change	13	114	0.67	0.00092
GO:0055114	Oxidation-reduction process	46	939	0.3	0.00092
GO:1901361	Organic cyclic compound catabolic process	29	472	0.4	0.00094
GO:0046700	Heterocycle catabolic process	27	422	0.42	0.00095
GO:0031503	Protein-containing complex localization	20	257	0.5	0.00098
GO:0010638	Positive regulation of organelle organization	35	633	0.35	0.0010
GO:0031325	Positive regulation of cellular metabolic process	121	3413	0.16	0.0010
GO:0033043	Regulation of organelle organization	58	1306	0.26	0.0010
GO:0010604	Positive regulation of macromolecule metabolic process	126	3600	0.16	0.0011
GO:0051276	Chromosome organization	50	1066	0.28	0.0011
GO:0009893	Positive regulation of metabolic process	134	3893	0.15	0.0012
GO:1901566	Organonitrogen compound biosynthetic process	59	1346	0.25	0.0012
GO:0034470	ncRNA processing	25	381	0.43	0.0013
GO:0051171	Regulation of nitrogen compound metabolic process	186	5836	0.12	0.0013
GO:0044419	Interspecies interaction between organisms	76	1899	0.21	0.0014
GO:0006950	Response to stress	122	3485	0.16	0.0016
GO:0019439	Aromatic compound catabolic process	27	437	0.4	0.0016
GO:0030036	Actin cytoskeleton organization	30	516	0.38	0.0016
GO:0006401	RNA catabolic process	19	247	0.5	0.0017
GO:0042254	Ribosome biogenesis	21	292	0.47	0.0017

GO:0019752	Carboxylic acid metabolic process	42	853	0.3	0.0018
GO:0051246	Regulation of protein metabolic process	103	2828	0.17	0.0018
GO:0017038	Protein import	14	144	0.6	0.0019
GO:0032268	Regulation of cellular protein metabolic process	99	2693	0.18	0.0019
GO:0043436	Oxoacid metabolic process	45	944	0.29	0.0019
GO:0044265	Cellular macromolecule catabolic process	44	917	0.29	0.0020
GO:0006406	mRNA export from nucleus	12	109	0.65	0.0023
GO:0019538	Protein metabolic process	142	4251	0.14	0.0025
GO:0071103	DNA conformation change	22	328	0.44	0.0027
GO:0097435	Supramolecular fiber organization	28	480	0.38	0.0027
GO:0006402	mRNA catabolic process	17	214	0.51	0.0029
GO:0000956	Nuclear-transcribed mRNA catabolic process	16	194	0.53	0.0032
GO:0000244	Spliceosomal tri-snRNP complex assembly	5	13	1.2	0.0034
GO:0009889	Regulation of biosynthetic process	140	4210	0.13	0.0035
GO:0006606	Protein import into nucleus	11	97	0.67	0.0037
GO:0051173	Positive regulation of nitrogen compound metabolic	113	3239	0.15	0.0037
GO:0010468	Regulation of gene expression	156	4813	0.12	0.0038
GO:0022402	Cell cycle process	45	976	0.28	0.0038
GO:0051301	Cell division	28	493	0.37	0.0040
GO:0007052	Mitotic spindle organization	10	81	0.7	0.0041
GO:0010557	Positive regulation of macromolecule biosynthetic pro-	74	1906	0.2	0.0042
GO:0048519	Negative regulation of biological process	171	5389	0.11	0.0042
GO:2000736	Regulation of stem cell differentiation	12	119	0.62	0.0047
GO:0031124	mRNA 3-end processing	10	83	0.69	0.0048
GO:0034250	Positive regulation of cellular amide metabolic process	14	162	0.55	0.0056
GO:0045935	Positive regulation of nucleobase-containing compound	74	1927	0.2	0.0058
GO:0050896	Response to stimulus	238	8046	0.08	0.0061
GO:0000387	Spliceosomal snRNP assembly	7	39	0.87	0.0063
GO:0010556	Regulation of macromolecule biosynthetic process	132	3976	0.13	0.0063
GO:1901565	Organonitrogen compound catabolic process	47	1070	0.25	0.0073
GO:0071214	Cellular response to abiotic stimulus	20	313	0.42	0.0099
GO:0072583	Clathrin-dependent endocytosis	6	29	0.93	0.0099

Table 7: List of all enriched GO terms (STRING analysis) "cellular components" Hep3B CGI-58 KD vs control using only proteins with a p-value of < 0.05 (two-sided t-test without FDR correction, S_0 = 0.1) for analysis. FDR cut-off value 0.1.

#TERM ID	TERM DESCRIPTION GO CELLULAR COMPONENT HEP3B CGI-58 KD-C	OBSERVED GENE COUNT	BACKGROUND GENE COUNT	STRENGTH	FALSE DISCOVERY RATE
GO:0005622	Intracellular	466	14276	0.13	6.67e-44
GO:0070013	Intracellular organelle lumen	289	5857	0.31	2.98e-39
GO:0043226	Organelle	449	13515	0.13	5.91e-38
GO:0043227	Membrane-bounded organelle	431	12427	0.15	1.85e-37
GO:0043229	Intracellular organelle	429	12528	0.15	6.01e-35
GO:0005737	Cytoplasm	403	11428	0.16	2.28e-31
GO:0043231	Intracellular membrane-bounded organelle	385	10761	0.17	6.73e-29
GO:0005829	Cytosol	247	5193	0.29	2.07e-28
GO:0032991	Protein-containing complex	237	5073	0.28	1.58e-25
GO:0005654	Nucleoplasm	199	3973	0.31	1.97e-23
GO:0031981	Nuclear lumen	219	4733	0.28	3.54e-22
GO:0005634	Nucleus	291	7390	0.21	6.35e-22

GO:0070062	Extracellular exosome	127	2099	0.39	1.79e-19
GO:0043232	Intracellular non-membrane-bounded organelle	213	4880	0.25	2.95e-18
GO:1990904	Ribonucleoprotein complex	63	677	0.58	1.03e-16
GO:0110165	Cellular anatomical entity	474	17788	0.04	5.08e-13
GO:0031982	Vesicle	163	3879	0.24	3.19e-11
GO:0005681	Spliceosomal complex	26	192	0.74	1.18e-09
GO:0005615	Extracellular space	137	3195	0.24	1.45e-09
GO:0005684	U2-type spliceosomal complex	19	94	0.92	1.51e-09
GO:0031983	Vesicle lumen	32	330	0.6	1.39e-08
GO:0005730	Nucleolus	56	924	0.39	7.94e-08
GO:1904813	ficolin-1-rich granule lumen	19	125	0.79	9.80e-08
GO:0034774	Secretory granule lumen	30	324	0.58	1.22e-07
GO:0005856	Cytoskeleton	100	2221	0.27	1.26e-07
GO:0030055	Cell-substrate junction	33	413	0.51	5.20e-07
GO:0016604	Nuclear body	48	789	0.4	9.44e-07
GO:0005925	Focal adhesion	32	405	0.51	1.05e-06
GO:0070161	Anchoring junction	49	820	0.39	1.07e-06
GO:1902494	Catalytic complex	67	1328	0.31	1.42e-06
GO:0005844	Polysome	13	68	0.89	2.63e-06
GO:0031252	Cell leading edge	32	425	0.49	2.68e-06
GO:0005576	Extracellular region	152	4166	0.17	3.67e-06
GO:0099080	Supramolecular complex	63	1261	0.31	4.87e-06
GO:0071013	Catalytic step 2 spliceosome	14	87	0.82	4.97e-06
GO:0005759	Mitochondrial matrix	32	479	0.44	2.98e-05
GO:0001726	Ruffle	18	179	0.61	4.82e-05
GO:0071005	U2-type precatalytic spliceosome	10	50	0.91	5.30e-05
GO:0016607	Nuclear speck	28	399	0.46	5.68e-05
GO:0015629	Actin cytoskeleton	31	477	0.42	6.84e-05
GO:0099512	Supramolecular fiber	48	939	0.32	8.23e-05
GO:0005635	Nuclear envelope	30	472	0.42	0.00014
GO:0030141	Secretory granule	43	845	0.32	0.00030
GO:0099513	Polymeric cytoskeletal fiber	38	705	0.34	0.00030
GO:0005694	Chromosome	71	1712	0.23	0.00038
GO:0005739	Mitochondrion	67	1611	0.23	0.00062
GO:0030054	Cell junction	81	2075	0.2	0.00069
GO:0120114	Sm-like protein family complex	10	73	0.75	0.00083
GO:0015030	Cajal body	9	59	0.8	0.00096
GO:0005788	Endoplasmic reticulum lumen	21	308	0.45	0.0013
GO:0030863	Cortical cytoskeleton	11	96	0.67	0.0014
GO:0034399	Nuclear periphery	13	133	0.6	0.0014
GO:0015630	Microtubule cytoskeleton	53	1219	0.25	0.0015
GO:0099503	Secretory vesicle	46	1010	0.27	0.0017
GO:0012505	Endomembrane system	148	4542	0.13	0.0020
GO:0048471	Perinuclear region of cytoplasm	36	727	0.31	0.0022
GO:0005905	Clathrin-coated pit	9	69	0.73	0.0025
GO:0016363	Nuclear matrix	11	108	0.62	0.0033
GO:0097525	Spliceosomal snRNP complex	8	56	0.77	0.0034
GO:0010494	Cytoplasmic stress granule	9	73	0.7	0.0036
GO:0005938	Cell cortex	19	292	0.43	0.0045
GO:0098687	Chromosomal region	20	318	0.41	0.0046
GO:0016020	Membrane	261	9072	0.07	0.0052
GO:0000502	Proteasome complex	8	62	0.72	0.0059
GO:0005777	Peroxisome	12	138	0.55	0.0059
GO:0070381	Endosome to plasma membrane transport vesi-	3	3	1.61	0.0059
GO:0000793	Condensed chromosome	15	216	0.45	0.0098
GO:0030864	Cortical actin cytoskeleton	8	68	0.68	0.0098
GO:0031410	Cytoplasmic vesicle	84	2386	0.16	0.0099

Table 8: List of all enriched GO terms (STRING analysis) "KEGG pathways" Hep3B CGI-58 KD vs control using only proteins with a p-value of < 0.05 (two-sided t-test without FDR correction, S0 = 0.1) for analysis. FDR cut-off value 0.1.

#TERM ID	TERM DESCRIPTION KEGG PATHWAYS HEP3B CGI-58 KD-C	OBSERVED GENE COUNT	BACKGROUND GENE COUNT	STRENGTH	FALSE DISCOVERY RATE
HSA0304	Spliceosome	24	132	0.87	1.28e-10
HSA0301	RNA transport	18	160	0.66	4.69e-05
HSA0414	Protein processing in endoplasmic reticulum	18	165	0.65	4.73e-05
HSA0028	Valine, leucine and isoleucine degradation	9	46	0.9	0.00047
HSA0002	Citrate cycle (TCA cycle)	6	29	0.93	0.0102
HSA0007	Fatty acid degradation	7	42	0.83	0.0102